Lawrence Berkeley Laboratory
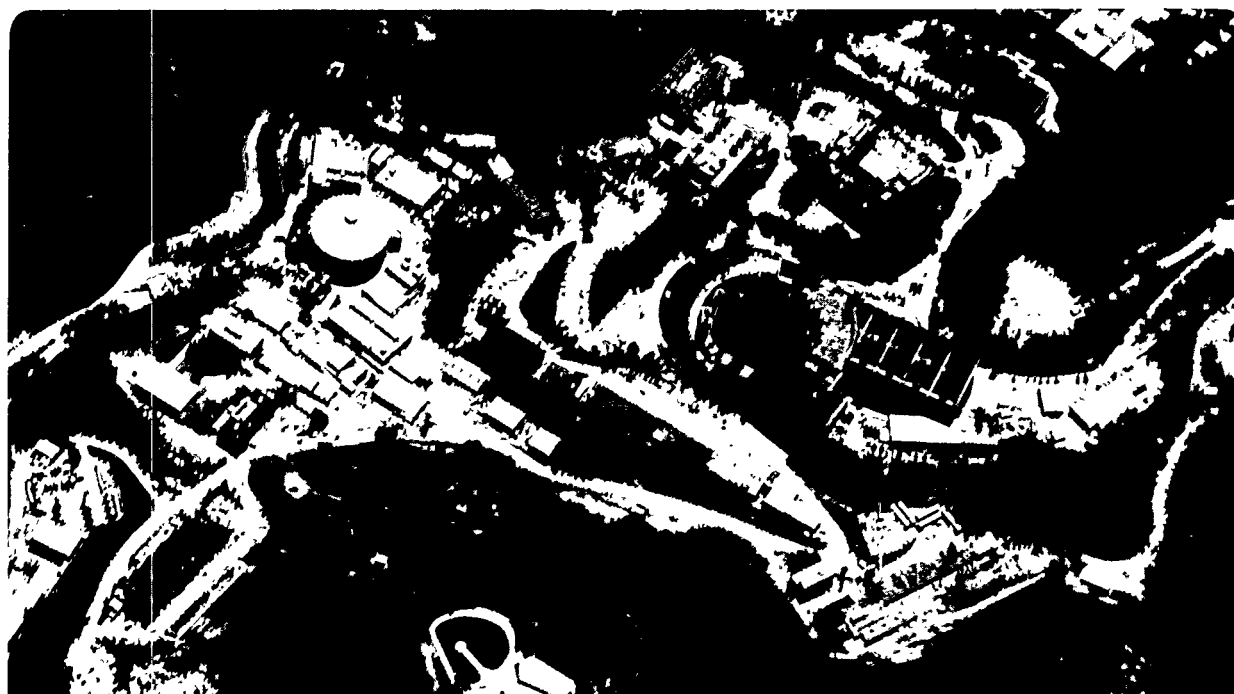
UNIVERSITY OF CALIFORNIA

Physics Division

High Spatial Resolution Radiation
Detectors Based on Hydrogenated
Amorphous Silicon and Scintillator

T. Jing
(Ph.D. Thesis)

May 1995

DISCLAIMER

DISCLAIMER

Portions of this document may be illegible in electronic image products. Images are produced from the best available original document.

High Spatial Resolution Radiation Detectors Based on Hydrogenated Amorphous Silicon and Scintillator

Tao Jing
Ph.D. Thesis

Department of Engineering—Nuclear Engineering
University of California, Berkeley

and

Physics Division
Lawrence Berkeley Laboratory
University of California
Berkeley, CA 94720

May 1995

High Spatial Resolution Radiation Detectors Based on
Hydrogenated Amorphous Silicon and Scintillator

by

Tao Jing

B.E. (Northeast University) 1984
M.S. (China Medical University) 1987

A thesis submitted in partial satisfaction of the

requirements for the degree of

Doctor of Philosophy

in

Engineering-Nuclear Engineering

in the

GRADUATE DIVISION

of the

UNIVERSITY of CALIFORNIA at BERKELEY

Committee in charge:

Professor Selig N. Kaplan, Chair
Professor Victor Perez-Mendez
Professor Chenming Hu

1995

High Spatial Resolution Radiation Detectors Based on

Hydrogenated Amorphous Silicon and Scintillator

Copyright © 1995

by

Tao Jing

Abstract

High Spatial Resolution Radiation Detectors Based on Hydrogenated Amorphous Silicon and Scintillator

by

Tao Jing
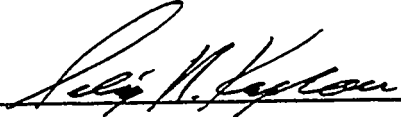
Doctor of Philosophy in Nuclear Engineering

University of California at Berkeley

Professor Selig N. Kaplan, Chair

Hydrogenated amorphous silicon (a-Si:H) as a large-area thin film semiconductor with ease of doping and low-cost fabrication capability has given a new impetus to the field of imaging sensors; its high radiation resistance also makes it a good material for radiation detectors. In addition, large-area microelectronics based on a-Si:H or polysilicon can be made with full integration of peripheral circuits, including readout switches and shift registers on the same substrate. Thin a-Si:H p-i-n photodiodes coupled to suitable scintillators are shown to be suitable for detecting charged particles, electrons, and X-rays. The response speed of CsI/a-Si:H diode combinations to individual particulate radiation is limited by the scintillation light decay since the charge collection time of the diode is very short (<10ns). The reverse current of the detector is analyzed in term of contact injection, thermal generation, field enhanced emission (Poole-Frenkel effect), and edge leakage. A good collection efficiency for a diode is obtained by optimizing the p layer of the diode thickness and composition. The CsI(Tl) scintillator coupled to an a-Si:H photodiode detector shows a capability for detecting minimum ionizing particles with S/N ~20. In such

1

an arrangement a p-i-n diode is operated in a photovoltaic mode (reverse bias). In addition, a p-i-n diode can also work as a photoconductor under forward bias and produces a gain yield of 3-8 for shaping times of 1 μs. The mechanism of the formation of structured CsI scintillator layers is analyzed. Initial nucleation in the deposited layer is sensitive to the type of substrate medium, with imperfections generally catalyzing nucleation. Therefore, the microgeometry of a patterned substrate has a significant effect on the structure of the CsI growth. CsI films with internal columnar structure developed using techniques described have produced greater X-ray detection sensitivity and higher spatial resolution than presently available commercial scintillator screens.

Committee in charge: Selig N. Kaplan,   Chair
                       Victor Perez-Mendez
                       Chenming Hu

To my family

Table of Contents

Chapter 5. Radiation Detection

Chapter 6. Conclusion

Acknowledgments

I would like to express my greatly appreciation to Professors Victor Perez-Mendez and Selig N. Kaplan for their great ideas, valuable suggestions, encouragement and guidance to conduct my research in the Lawrence Berkeley Laboratory. I also would like to thank Dr. Chenming Hu, a Professor of EECS, for his kindness, helpful discussions and guidance to complete thesis, as well as for his wonderful lectures on solid state devices which are helpful for my research and very useful for my future carrier. My appreciation is extended to Professor Jasmina Vujic for her useful discussions and valuable lecture. I would like to thank my group members, Drs. Gyuseong Cho, John Drewery, Ichiro Fujieda, Wan-Shick Hong, Hyoung-Koo Lee, Ali Mireshghi, and Daniel Wildermuth for experimental assistance and discussions during my research. I specially thank to Claude Goodman, a very kindly scientist from Air Techniques, Inc., New York for his many useful discussion and experimental assistance to the study related with CsI scintillators. I also would like to express gratitude to Dr. Gene Weckler of EG&G, Reticon for providing me photosensor array and readout electronics, which is essential to characterize the spatial properties of CsI layers.

Finally, I would like to thank my parents who continue their support in my life, my wife, Hong Xu , who always supports me in every aspect since we were in love twelve years ago, as well as my two lovely sons, Muqing Jing (Jing Jing), a very brilliant boy, Kirk Jing, a handsome little gentleman.

Chapter 1. Introduction

The introduction of hydrogenated amorphous silicon (a-Si:H) as large area thin-film semiconductors with low cost, ease of doping, and low temperature fabrication capability has not only given a new impetus to the field of optoelectronic devices- solar cells, flat panel displays, image sensors and others, but also forms the basis for large area microelectronics[1-3]. The development of large area amorphous silicon radiation detectors coincides with the demands arising from rapidly growing field of various imaging applications such as digital medical radiography or high energy particle tracking which require good position resolution[4-6]. This thesis describes the development of radiation detectors based on a-Si:H/CsI combination and emphases the realization of the high spatial resolution of the imager by developing columnar structure CsI scintillator layers. In this chapter, some basic properties of a-Si:H, its preparation, and the principles of these detectors are described.

1.1 Hydrogenated Amorphous Silicon (a-Si:H)

1.1.1 The Disordered structure

The essential feature of the amorphous semiconductor, in contrast to its crystalline counterpart, is its disordered structure, i.e. the absence of long range periodicity in the positions of the constituent atoms.

In spite of this disorder, amorphous silicon has an absorption gap and high temperature activation energy for conductivity similar to those for crystalline silicon. This happens because, irrespective of the way a semiconductor solid is built in the long range (ordered or disordered), the way each atom is bonded to its neighbors is the same, being governed by quantum chemistry laws. The partially disordered semiconductor conserves locally, to a very great extent, the short-range order of the crystalline solid, but not the long-range order. The structure of a-Si:H is represented by a continuous random network

as shown in Fig.1.1. While in a crystal distorted bonds also represent defects, in the amorphous materials they are the rule and defects are represented by broken or unsaturated bonds which are formed to release internal tension[7]. These intrinsic defects produce defect states between the valence type and conducted type states (Fig.1.2b). The most prominent intrinsic defect is the unsaturated bond, called the dangling bond, which is a paramagnetic center contributing an uncompensated spin to the electron spin resonance (ESR) signal [8,9]. Depending on the particular amorphous material considered, the defects may have different contributions to the electronic energy structure such as dangling bonds and voids which act as trapping and recombination centers for electrons and holes.

O Silicon

● Hydrogen
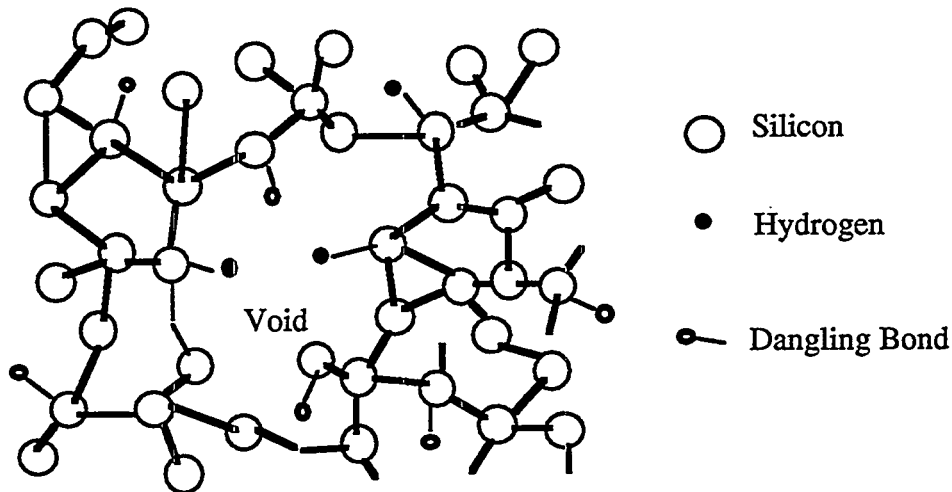
o— Dangling Bond

Fig.1.1 A schematic random network structure of a-Si:H showing dangling
bonds, voids, and the long range disorder structure.

It has been shown by Hall (1952)[10] and by Weaire and Thorpe (1971)[11] that this short-range order is responsible for the presence of a gap between the valence band and conduction band states in the energy state density distribution of a solid, either crystalline or amorphous.

1.1.2 Density of states and electronic transport

In an ideal impurity and defect-free crystal, the gap is completely free of states, its

limits being singularity points of the energy state density distribution (valence and conduction band limits—see Fig.1.2(b)). It is generally accepted [12] that fluctuations of bond length, bond angles and dihedral angles are responsible for replacing singularity edges of the bands with a wide tailing of the bands into the gap (Fig.1.2(b)).
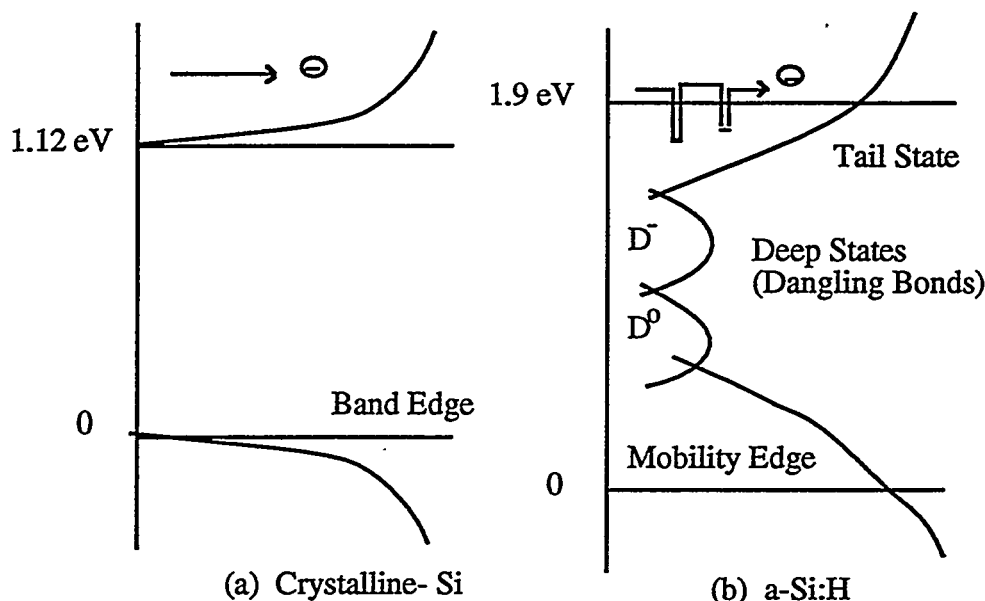
Fig.1.2 Schematic band diagrams of (a) crystalline and (b) amorphous silicon.

As we have seen, the pattern of the density of states (DOS) distribution is broadly the same for crystalline and amorphous semiconductors, but the nature of the states may be significantly different. In the crystal the band states are all extended but in the a-Si:H, part or even all, of them may be localized, depending on the degree of disorder [13] (see Fig. 1.2(b)). In the band tail states, the density of states is so low that the electron wave function do not overlap between states. Thus electrons or holes in the tail states can not move as freely as in the conduction or valence band. In contrast to crystalline silicon, the observed average mobility, often called the drift mobility of amorphous silicon around room temperature, increases as the temperature is raised because of excitation of trapped electrons in the tails states to higher conduction states. The observed drift mobilities are typically ~ 1 cm^2/Vsec and ~ 0.004 cm^2/Vsec for electrons and holes respectively at room temperature. Because of the asymmetrical density of states, with more states in the lower

3

half of the gap, the average drift mobility of holes is much lower than that of electrons. Also, hole transport is dispersive and is governed by a hopping mechanism even at room temperature. At very low temperatures, transport of both carriers is dominated by a hopping mechanism rather than drift. Hopping is a conduction mechanism in which carriers jump from a localized tail state to a neighboring tail state under the influence of the electric field. Table 1.1 is a comparison of fundamental properties of crystalline silicon and a-Si:H.

Table 1.1 Material properties of crystalline silicon and hydrogenated amorphous silicon

Properties	Crystalline Si	a-Si:H
Structure	Diamond	random network
Interatomic distance (Å)	2.35	2.35 ± 0.07
First bond angle (°)	109.47	109 ± 10
Density (g/cm^3)	2.3	~ 2.25
Dielectric constant	12.0	~ 11.8
Resistivity (Ωcm)	$< 10^5$	$> 10^9$
Electron mobility (cm^2/Vsec)	1350	1 ~ 2
Hole mobility (cm^2/Vsec)	480	0.004 ~ 0.007
Band gap energy (eV)	1.12 (indirect)	1.7 ~ 1.9 (direct)

The addition of Hydrogen to the amorphous silicon has the effect of passivating many of the dangling bonds by attaching to them. For a-Si:H, many more hydrogen atoms are incorporated than are necessary to compensate for the dangling bonds. By forming Si-H bonds, instead of very strained Si-Si bonds, internal stresses are reduced and the carrier mobility is improved. This flexibility is found to be responsible for specific mechanisms for the formation of metastable dangling bonds, associated with non-equilibrium carrier recombination [14].

4

1.1.3 Growth methods

Amorphous silicon has been prepared using numerous deposition techniques such as: glow discharge(GD) or Plasma Enhanced Chemical Vapor Deposition (PECVD); CVD; reactive sputtering; reactive evaporation. Among these methods, a-Si films prepared from SiH4 gas using PECVD method possesses the lowest density of dangling bond states. These films containing approximately 10 atomic percent hydrogen[15] are appropriately referred to as a-Si:H. PECVD is presently the most important deposition technique and is widely used in industry.

Fig.1.3 shows a schematic diagram of the LBL PECVD system. In the PECVD method, silane gas, sometimes diluted with hydrogen, is fed into a vacuum chamber through a control valve and decomposed in a glow discharge by capacitively or inductively coupled rf power into SiH_n^- (n = 1~3) and H^+ and forms a weakly ionized plasma[16]. SiH_n^- ions, precursors, diffuse onto a substrate and form a Si-Si network by chemical reactions assisted by the heat. Heat is transferred from the filament underneath the substrate by controlling its temperature. During the deposition process hydrogen gas is evolved from the surface and is removed by the vacuum pump together with the excess gas. The incorporation of hydrogen to satisfy Si dangling bonds, which are an inevitable consequence of the non-periodic structure, is responsible for the satisfactory electrical transport and optical properties. p and n type a-Si:H layers can be achieved by adding dopant gases such as diborane (B_2H_6) or phospine (PH_3) to silane gas.

The opto-electronic properties of the PECVD a-Si:H films depend upon many deposition parameters such as the: pressure of the gas; flow rate; substrate temperature; power dissipation in the plasma; excitation frequency. Optimization of the deposition condition needs lengthy trial-error experiments. Table 1.2 shows an example of the deposition conditions for LBL PECVD system that are generally employed to produce high quality electronic material.

Sample Transfer
Device

Load Lock
Chamber

Roughing Pump

Process
Vacuum
Chamber

Gate
Valve

RF Generator

Turbo
Pump

Substrate

Isolation
Valve

Throttle
Valve

Turbine

Backing
Pumps

Flow Controller

Purge
Valve

Excess Flow Valve

Pneumatic
Cylinder Valve

Gas
Cylinder

Chemical
Scrubber

Gas
Cabinet

To Exhaust
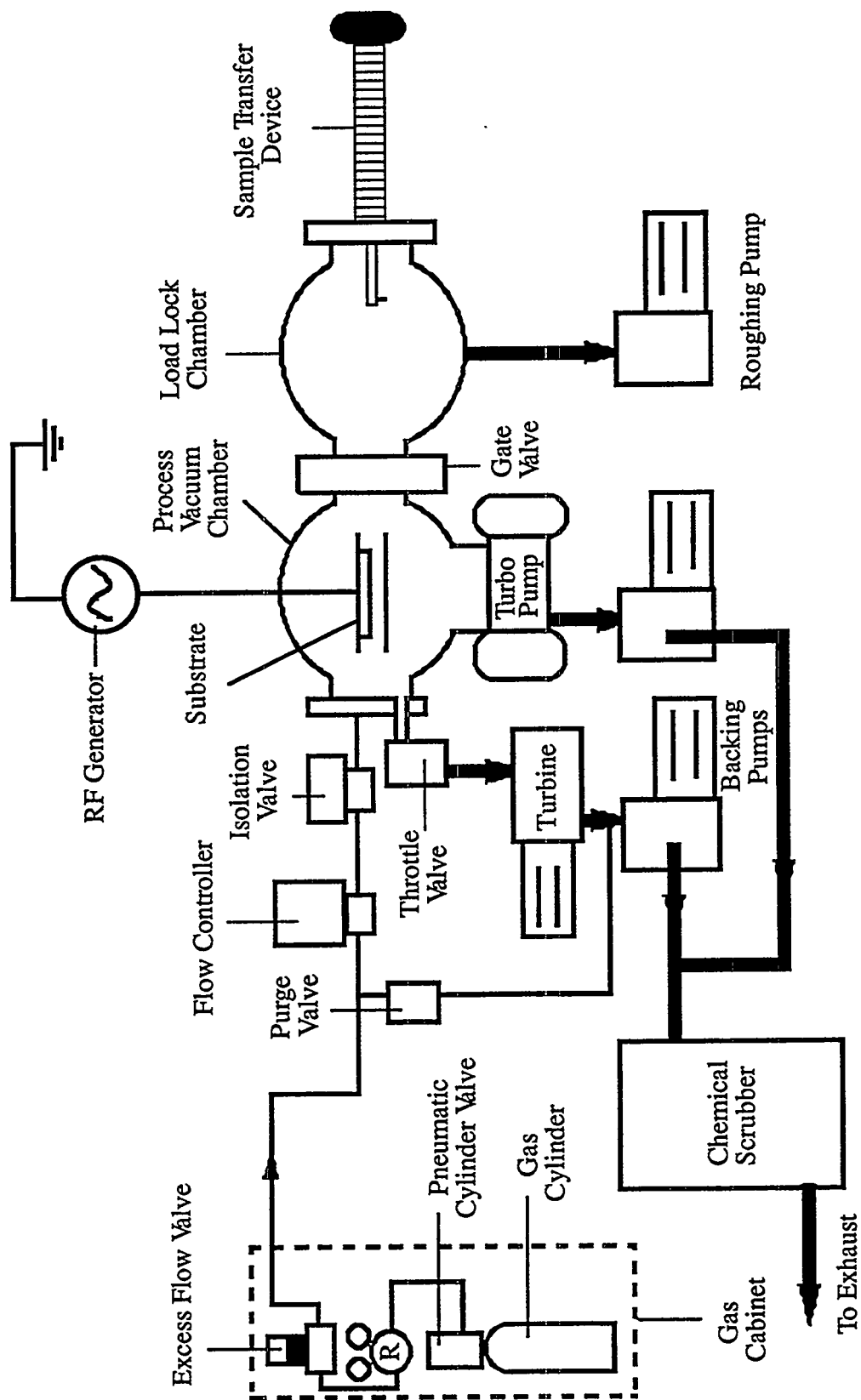
Fig. 1.3 A Schematic diagram of LBL PECVD system

6

Table. 1.2 Deposition parameters of LBL PECVD system

Layer type	n-layer	i-layer	p-layer
Gases & flow rate	SiH_4 : 40 sccm PH_3 : 8 sccm	SiH_4 : 40 sccm	SiH_4 : 40 sccm B_2H_6 : 15 sccm CH_4 : 90 sccm
Heater temperature	320 °C	320 °C	250 °C
RF power	5 Watt/cm^2	7 Watt/cm^2	5 Watt/cm^2
Pressure	300 mTorr	300 mTorr	300 mTorr
Growth rate	27 nm/min	38 nm/min	27 nm/min

1.2 A-Si:H radiation detector

1.2.1 Background

Crystalline semiconductors such as silicon and germanium have had a long record of functioning as detectors of ultraviolet and visible light, charged particles, X-rays, and γ rays. a-Si:H has been investigated also as an alternative for these applications. Many efforts have been made to show its capabilities as radiation detectors. As an X-ray detector, it has shown a good linearity between the output signal and the input X-ray intensity[17]. When coupled to a suitable high Z phosphor, a larger signal can be obtained[18]. Two dimensional a-Si:H photodiode arrays coupled to light emitting intensifying screens have been used for X-ray and γ ray imaging detection. Our group has also developed a-Si:H detectors in applications for charged particle, neutron, and X-ray detection[19-23].

1.2.2 Detection principles

A-Si:H radiation detector structure is a reverse biased p-i-n diode which is similar to that of solar cells. A detector consists of a metallic layer and a thin heavily doped p^+ layer (~ 10-30 nm), followed by an intrinsic i layer which forms the bulk of the diode, then a thin heavily doped n^+ layer (~ 30 nm) and finally a thin metallic layer. Chromium or palladium are the usual metals that are used for the electrical contact. The p and n layers are blocking layers to minimize the reverse current. The bulk i layer acts as the main region where the incident radiation interacts and generates the secondary electron-hole pairs. The i-layer must be thick enough to produce enough electron-hole pairs to give a detectable signal.
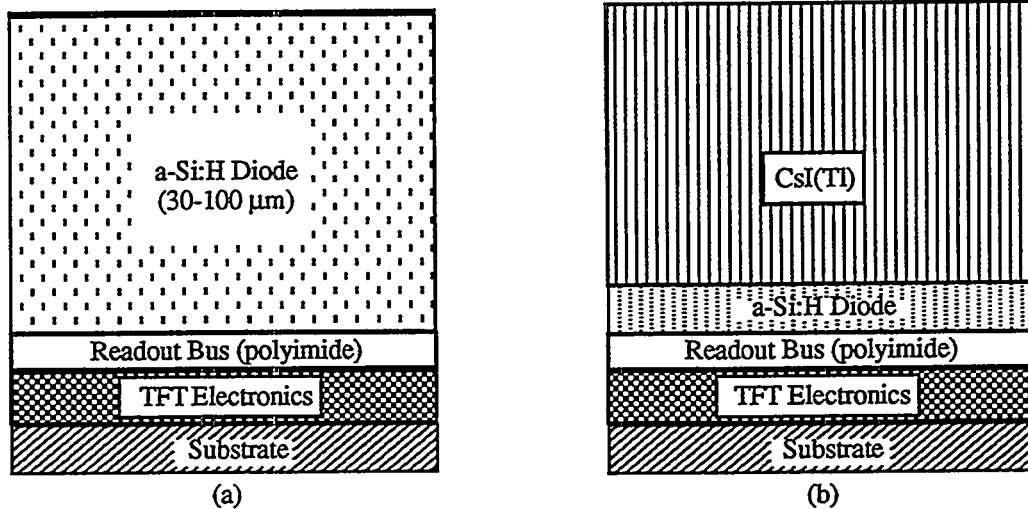
Fig.1.4 Detector configurations (a) thick p-i-n diode and (b) thin p-i-n photodiode coupled to scintillator layer

The incident radiation can be detected as a fluence in some cases. Alternatively, other applications require the detection of individual high energy photons (x-rays, γ-rays) or individual charged particles. Two basic detector configurations are shown schematically in Fig.1.4. Fig.1.4(a) shows such a detector in which the i layer is made 30-100 μm thick in order for incident charged particles to be able to deposit enough energy to produce a large enough signal. Fig.1.4(b) shows an alternative configuration in which a thin 1-2 μm

8

thick a-Si:H p$^+$-i-n$^+$ diode acts as a detector of visible light and is coupled to a thick (>100 μm) converter layer of CsI or other scintillator which converts the energy deposited by charged particles, X-rays into visible light in the visible (300-700 nm). The signal in both cases is $V_s = Q/C_d$, where Q is the collected charge and C_d the electrical capacity of the detector element. For single particle detection, where Q is often in the range of only a few thousand e-h pairs, the detector capacitance should be kept to a minimum in order to achieve a large signal to noise radio.

1.3 CsI(Tl) Scintillator

For this case we assume that the signal is produced predominantly by the interaction of the radiation with a scintillator and that the scintillation light is then detected by the a-Si:H through a transparent indium tin oxide contact. Choice of a scintillator dependents on specific requirements for each detector application, namely, the type of radiation, speed requirement and spatial resolution. Among various scintillating materials, CsI(Tl) appears the most promising for the following reasons :

(a) Large-area deposition : It is readily deposited by vacuum evaporation at low deposition substrate temperature [24] in the range of 50 ~ 200 °C. This allows for the possibility of direct evaporation onto an a-Si:H photo diode layer without degrading the a-Si:H which starts to degrade at 250 °C. The CsI layer adheres well to glass or a-Si:H. However in order to deposit it with good bonding on ITO coated a-Si:H it was found necessary to deposit an intermediate layer of ~ 1μm thick polyimide which is transparent to the scintillation light.[25] The details of the evaporation conditions for the CsI will be discussed in chapter 4.

(b) Good spatial resolution : Depending on the deposition conditions, it forms columnar structures [26,27] which limit the light diffusion sideways and allows high spatial resolution. 100 μm of spatial resolution has been demonstrated from 1 mm thick CsI(Tl) by

17 KeV X-ray which was a factor of 2 higher than that of the same thickness Gd_2O_2S, a commonly used scintillator[28].

(c) Light properties : After interacting with the incident radiation, CsI(Tl) emits a spectrum of light with decay time of 1 μsec. The emitted light is in the visible and matches well the absorption response of a-Si:H as shown in Fig.1.5 which compares the light spectrum with other CsI materials.[29] The light yield is 60,000 visible photons per 1 MeV energy deposit under optimal conditions[30, 31], which is among the highest light output of any known scintillator.
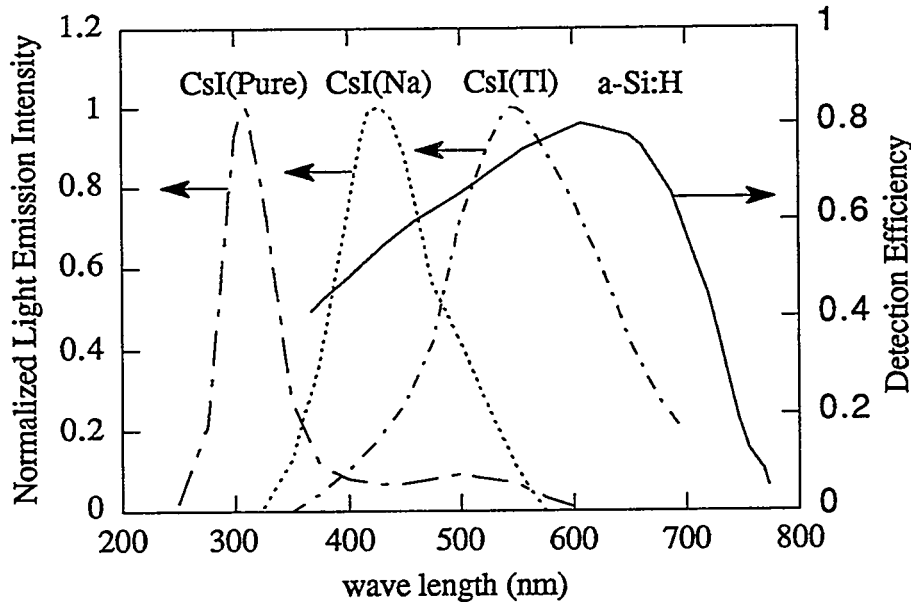
Fig.1.5 Scintillation light spectra of CsI(Tl) and CsI(Na) and detection efficiency of a-Si:H photodiodes.

The main disadvantage of CsI(Tl) scintillators is that their resistance to radiation damage by energetic particles (fast neutrons or high energy protons) and by gamma rays is not as high as that of a-Si:H. Perez-Mendez et al.[32] have shown that a-Si:H is extremely radiation resistant and is not damaged by fast neutron fluxes upto 10^{14} n/cm^2. However, because the CsI(Tl) is deposited in thin layers, the degradation due to radiation which is

largely due to attenuation of the light transmission is less than that of thick crystals. For example, for a ~ 100 μm thick deposition the signal from gamma rays emitted by Co^{60} dropped by half after an irradiation dose of 10^6 rad of the same gamma rays[28]. By comparison with a 1 mm crystalline CsI(Tl) detector, the signal dropped to half at 10^4 rad.[33]

CsI(Na) is more radiation resistant than CsI(Tl) [34] and it has a short lived ~ 20 nsec component but it is hygroscopic and emits less light (38,000 photon/MeV)[24]. Other scintillators, such as cadmium tungstate, gadolinium oxysulfide, gadolinium silicate etc., which can be deposited in large areas may also prove applicable to the indirect detection method.

Thus for those reasons above, the combination of CsI(Tl) layer with a-Si:H diode pixel arrays is a good choice for large area, low cost, sensitive 2-D radiation detectors.

References:

[1]   K. Kempter, "Large-Area Electronics Based on Amorphous Silicon," Adv. Sol. Stat. Phys. (Festkorpreprobleme). Vol.27, 1987, pp.279-305.

[2]   K. Rosan, "Hydrogenated Amorphous-Silicon Image Sensors," IEEE Trans. Electron Devices, Vol.36, No. 12, p.2923-2927 (1989).

[3]   W. E. Howard, "Flat Panel Display Technologies," Japan Display 89, October 1989, p. 8-11.

[4]   S. N. Kaplan, J. Morel, V. Perez-Mendez and R. A. Street, "Detection of Charged Particles in Amorphous Silicon Layers," IEEE Trans. Nuc. Sci., NS-33, p.351-354 (1987)

[5]   I. Fujieda, R. A. Street, R. L. Weisfield, S. Nelson, P. Nylen, V. Perez-Mendez, and G. Cho, "High Sensitivity Readout of 2D a-Si Image Sensors," Jan. J. Appl. Phys. Vol.32, No.1A, p.198-204 (1993).

[6]   L. E. Antonuk, J. H. Siewerdsen, J. Yorkston, W. Huang, "Radiation Response of Amorphous Silicon Imaging arrays at Diagnostic Energies," IEEE Trans. Nuc. Sci., NS-41, p.1500-1505 (1994)

[7]   J. C. Philips, Phys. Rev. Lett. "Structure of Amorphous $(Ge,Si)_{1-x}Y_x$ Alloys," Vol.42, p.1151 (1979).

[8]   M. H. Brodsky and R. S. Tile, "Electron Spin Resonance in Amorphous Silicon, Germanium, and Silicon Carbide," Phys. Rev. Lett. Vol.23, p.581 (1969).

[9]   P. C. Tayler, "Magnetic Resonance Measurements in a-Si:H," *Semiconductors and Semimetals*, Academic Press, Vol. 21, Part C, p. 99 (1984).

[10]   G. G. Hall, Phil. Mag. Vol.43, p.338 (1952).

[11]   D. Weaire and M. F. Thorpe, "Electronic Properties of an Amorphous Solid. I. A Simple Tight-Binding Theory," Phys. Rev. B. Vol.4, p.2508 (1971).

[12]   H. Overhof and P. Thomas, Electronic Transport in Hydrogenated Amorphous Semiconductors, Springer Tracts in Modern Phys. Vol.114, Berlin, Springer (1989).

[13]   P. W. Anderson, Phys. Rev., Vol. 109, p.1492 (1958).

[14]   D. L. Staebler and C. R. Wronski, "Reversible Conductivity Change in Discharge-produced Amorphous Silicon," Appl. Phys. Lett. Vol. 31 p.292 (1977).

[15]   M. H. Brodsky, M. A. Frisch, J. F. Ziegler and W. A. Lanford, "Quantitative Analysis of Hydrogen in Glow Discharge Amorphous Silicon," Appl. Phys. Lett., 30, 561 (1977).

[16] A. Madan and M. P. Shaw, *The Physics and Applications of Amorphous Semiconductors*, Academic Press, Inc., San Diego, p.18 (1988).

[17] G. P. Wei, H. Okamoto, and Y. Hamakawa, "Amorphous-Silicon Photovoltaic X-ray Sensors," Jpn. J. Appl. Phys. Vol.24 p.1105 (1985).

[18] W. Guang, H. Okamoto and Y. Hamakawa, "Amorphous-Silicon Photovoltaic X-Ray Sensor," Jpn. J. Appl. Phys., Vol. 24, 1105 (1985).

[19] S. N. Kaplan, J. Morel, V. Perez-Mendez and R. A. Street, "Detection of Charge Particles in Amorphous Silicon Layers," IEEE Trans. Nuc. Sci., NS-33, 351 (1986).

[20] V. Perez-Mendez, S. N. Kaplan, G. Cho, I. Fujieda, S. Qureshi, W. Ward and R. A. Street, "Hydrogenated Amorphous Silicon Pixel Detectors for Minimum Ionizing Particles," Nuc. Inst. and Meth., A273, p.127-134 (1988).

[21] W. S. Hong, J. S. Drewery, T. Jing, H. K. Lee, S. N. Kaplan, A. Mireshghi, and V. Perez-Mendez,"Thick (~50μm) Amorphous Silicon P-I-N Diodes for Direct Detection of Minimum Ionizing Particles," to be published in Nuc. Inst. and Meth.

[22] A. Mireshghi, G. Cho, J. Drewery, S. N. Kaplan, V. Perez-Mendez and D. Wildermuth, "Amorphous Silicon Position Sensitive Neutron Detector," IEEE Trans. Nuc. Sci., NS-39, pp. 635-640 (1992).

[23] T. Jing, C.A. Goodman, G. Cho, J. Drewery, W.S. Hong, H. Lee, Y. Kitsuno, S.N. Kaplan, A. Mireshghi, V. Perez-Mendez, and D. Wildermuth, "Amorphous Silicon Pixel Layers with Cesium Iodide Converters for Medical Radiography," IEEE Trans Nuc. Sci., NS-41 p. 903-909 (1994).

[24] C. W. Bates, "Scintillation Process in Thin Films of CsI(Na) and CsI(Tl) due to Low Energy X-rays, Electrons and Protons," Adv. Electronics and Electron. Phys., 28A, 451 (1968).

[25] Pyralin polyimide coating P1-2555, Dupont Electronics, Wilmington, Delaware.

[26] A. L. N. Stevels and A. D. M. Schrama de Pauw, "Vapor-Deposited CsI:Na Layers, I. Morphologic and Crystallographic Properties, II. Screens for Application in X-ray Imaging Devices," Philips Res. Repts., 29, 340 (1974).

[27] T. Jing, G. Cho, J. Drewery, S. N. Kaplan, A. Mireshghi, V. Perez-Mendez and D. Wildermuth, "Enhanced Columnar Structure in CsI Layer by Substrate Patterning," IEEE Trans. Nuc. Sci., NS-39, p.1195-1192 (1992).

[28] I. Fujieda, G. Cho, J. Drewery, T. Gee, T. Jing, S. N. Kaplan, V. Perez-Mendez, D. Wildermuth and R.A. Street, "X-ray and Charged Particle Detection with CsI(Tl) Layer Coupled to a-Si:H Photodiode Layers," IEEE Trans. Nuc. Sci., NS-38, 255 (1991)

[29] H. Ito, S. Matsubara, T. Takahashi, T. Shimada and H. Takeuchi, "Integrated Radiation Detectors with a-Si Photodiodes on Ceramic Scintillators," Jap. J. Appl. Phys., Vol., 28, L1476 (1989)

[30] I. Holl, E. Lorenz and G. Mageras, "A Measurement of Light Yield of Some Common Inorganic Scintillators," IEEE. Trans. Nuc. Sci., NS-35, 105 (1989)

[31] J. D. Valentine, D. K. Wehe, G. F. Knoll, and C. E. Moss," Temperature Dependence of CsI(Tl) Absolute Scintillation Yield," IEEE Trans. Nucl. Sci. vol. 40, No. 4, 1993, pp. 1267-1274.

[32] V. Perez-Mendez, S. N. Kaplan, G. Cho, I. Fujieda, S. Qureshi, W. Ward and R. A. Street, "Hydrogenated Amorphous Silicon Pixel Detectors for Minimum Ionizing Particles," Nucl. Instr. and Meth., A273, 127 (1988)

[33] M. Kobayashi and S. Sakuragi, "Radiation Damage of CsI(Tl) Crystal above 10^3 rad," Nucl. Instr. and Meth., A254, 275 (1987)

[34] C. L. Woody, P. W. Levy, J. A. Kierstead, T. Skwarnicki, Z. Sobolewski, M. Goldberg, N. Horwitz, P. Souder, D. F. Anderson, "Readout Techniques and Radiation Damage of Undoped CsI," IEEE Trans. Nuc. Sci., NS-37, 497 (1990).

Chapter 2. Amorphous Silicon detector and Electronics

2.1 Photodetector

There are several types of photodetectors, classified according to the type of interface between electrodes and intrinsic layer: photoconductor, homojunction, heterojunction, Schottky barrier devices. Their schematic structures are shown in Fig.2.1.
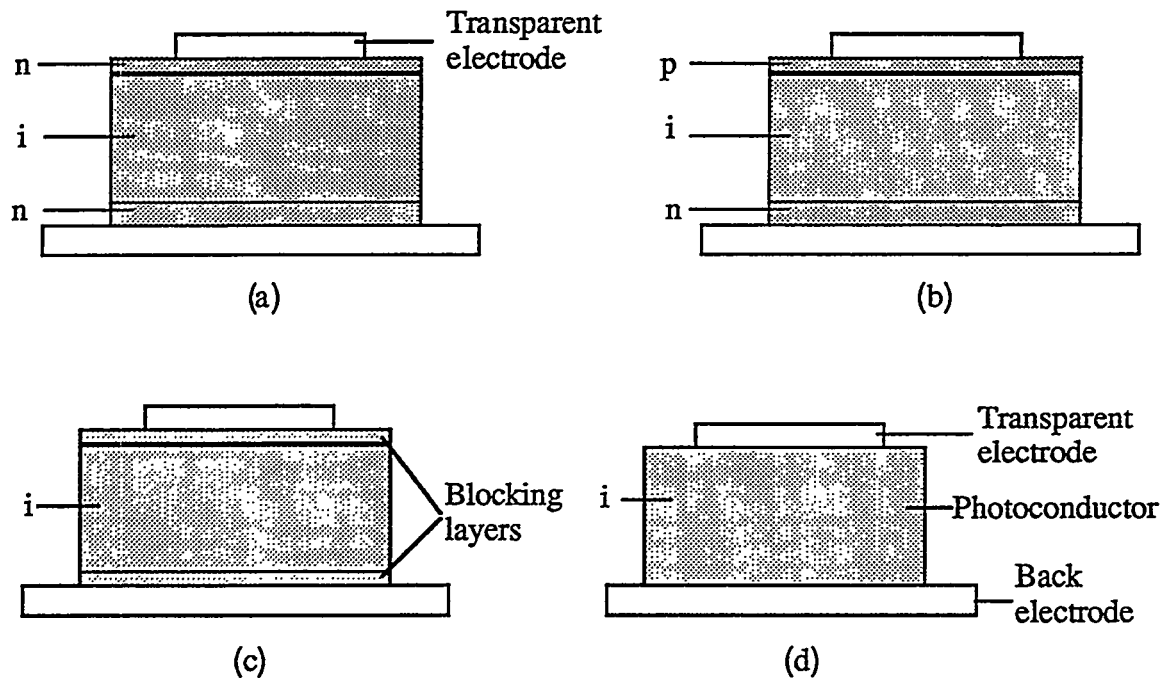
Fig.2.1 Types of thin film photodetectors. (a) Photoconductor; (b) Homojunction; (c) Heterojunction; (d) Schottky-barrier.

The photoresponse speed of photodiodes is due mainly to the transit of carriers. As the diode is depleted, only a small amount of trapped charge contributes to the decay time. Photodiodes are therefore used in most high-speed image sensors. For a photoconductor, however, the speed is much slower due to its current multiplication nature[1].

15

The polarity of a-Si:H photodiodes is almost always chosen to make the transparent electrode negative, thus ensuring that the carrier transport is dominated by electrons[2], because of their greater $\mu\tau$ product and mobility. Combinations of different junction types for the top and the bottom electrode are also used in thin-film image sensors.

These devices differ mainly in their fabrication complexity and dark current. The lowest dark-current densities of $\sim 10^{-9}$ A/cm^2 are usually achieved by homojunction devices such as p-i-n or p-i diodes or by heterojunction devices with SiN$_x$ or with p-a-SiC:H blocking layers, for example. To evaluate the degree of blocking, this value must be compared with the current density, given by the ohmic resistivity $\rho = 1\times10^9$ Ω cm of the a-Si:H bulk material. A 1 μm layer transmits a current of 1×10^{-7} A/cm^2 with 5V applied as opposed to the pure ohmic of 5×10^{-5} A/cm^2. From an economic point of view the Schottky barrier principle is attractive because of its simple structure.

2.1.1 Charge collection efficiency

The p-i-n diode is operated under reverse bias. In the i layer region, the dangling bonds are readily ionized under the action of the electric field across the diode, and will leave a density of positive charge which is about 30% of the density of the total dangling bonds as measured by electron spin resonance[3]. Thus the i layer exhibits a slightly n-type property and depletion of the i layer starts from the p-i junction and extends towards the i-n junction as the bias increases. The potential of the depletion layer V(x) is given by Poisson's equation

$$\frac{d^2V(x)}{dx^2} = -\frac{\rho(x)}{\varepsilon_0\varepsilon_{Si}},\qquad(2.1)$$

where ε_0 and ε_{Si} are the dielectric constant of vacuum and the relative dielectric constant of a-Si:H respectively. The space charge, $\rho(x)$, arises from the ionization of band gap states which are raised above the equilibrium Fermi energy by the band bending.

16

$$\rho(V, x) = \int_{E_F(0)}^{E_F(V(x))} qN(E)dE \approx qN_d^*, \tag{2.2}$$

The space charge density can be regarded as constant and is equal to the ionized dangling bond density qN_d^*. With this assumption, the depletion width and the electric field are easily derived as [4, 11] as:

$$W = \sqrt{\frac{2(V_b + V_0)}{\alpha}} = \left[\frac{2\varepsilon_0\varepsilon_{Si}(V_b + V_0)}{qN_d^*}\right]^{\frac{1}{2}}, \tag{2.3}$$

where V_0 is the built-in potential and V_b is the applied bias. α is $qN_d^*/\varepsilon_0\varepsilon_{Si}$.

The electric field is

$$E(x) = \alpha\,(x\text{-}w) \qquad 0 < x < w \qquad \text{Partial depletion} \tag{2.4}$$

$$E(x) = \alpha\,(x\text{-}0.5d - 0.5dw^2/d) = V/d + 0.5\alpha d - \alpha x \qquad \text{Fully depletion} \tag{2.5}$$

The relative importance of drift and diffusion is different in a-Si:H compared to crystalline silicon counterparts. Virtually all charge collection occurs within the depletion region, unlike the equivalent crystalline PN-junction device, in which there is efficient collection by diffusion from the field-free region.

(a) Charge collection simulation for CsI(Tl) light.

The wavelength of the scintillation light from most scintillators is in the range of 300-650nm. CsI(Tl) gives scintillation light which peaks at 560nm. This wavelength light will be strongly absorbed within a short distance ($< 0.3\ \mu m$) in the a-Si:H.

If the p-i-n diode is biased at a voltage V, the electrons and holes generated in the optical interaction will drift toward the positive and negative electrodes, including a current given by the Ramo theorem:[5]

$$i(t) = \frac{q}{d}\,[v_e(t)n_e(t) + v_h(t)n_h(t)], \tag{2.6}$$

17

Where q is the electron charge, d the thickness of the diode, v_e and v_h the velocities of electrons and holes and $n(t)$ their corresponding concentrations at instant t. To a first approximation, the carrier velocity follows a linear relationship with the electric field:

$$v_e(t) = \mu_e E(x), \quad v_h(t) = \mu_h E(x), \tag{2.7}$$

μ is the carrier mobility. $E(x)$, being the electric field distribution will be substituted by the average electric filed E. This is a reasonable assumption for a thin device.

The mean carrier concentration decreases due to deep trapping or recombination during the transit and its decrease is characterized by a lifetime τ, following an exponential decay law:

$$n_e(t) = n_0 e^{-t/\tau_e}, \quad n_h(t) = n_0 e^{-t/\tau_h}, \tag{2.8}$$

In this way, the current in eq.(2.6) becomes,

$$i(t) = \frac{qn_0 E}{d} [\mu_e e^{-t/\tau_e} + \mu_h e^{-t/\tau_h}], \tag{2.9}$$

and the total charge induced on the electrode during some measurement time T_m after charge injection is simply the integral of eq.(2.9) for electrons and holes, namely,

$$Q_e = \int_0^{T^*} i(t)\, dt = \frac{qn_0 E}{d} [\mu_e \tau_e (1 - e^{-T^* /\tau_e}) + \mu_h \tau_h (1 - e^{-T^* /\tau_h})] \tag{2.10}$$

T^* is either the measurement time T_m or the transit times of the electrons or holes through the depletion layer, whichever is shorter.

Because small carrier diffusion lengths are an inherent property of amorphous semiconductors, an important feature is the built-in drift field E_0, which provides a means of carrier transport across the device. When the external bias is applied to the device, the internal field will be modified. It is difficult to predict the precise distribution of the electric field inside the device because of its nonhomogenerous structure; however in order to make a correlation of results possible we shall assume that the resulting average field is given by

$$E = E_0 + V_d/d, \tag{2.11}$$

18

V_d is the applied bias voltage. Obviously, eq.(2.11) is an oversimplification, justifiable only by the fact it leads to resonably consistent results.

When strongly absorbed radiation, 560nm light in this case, is incident on the p-side of a diode, a signal is essentially induced by the electrons only. Because the transit distances for hole are short so that the transit time for hole T^*_h is nearly zero, the second term of the eq.(2.10) can be neglected. Hence, the charge collection efficiency is

$$\eta = \frac{Q_e + Q_h}{Q_{gen}} = \frac{Q_e}{qn_0} = \frac{\mu_e \tau_e E}{d} (1 - e^{-T^*_e / \tau_e}), \tag{2.12}$$

Because the transit time T_r for electrons is shorter than the measurement time Tm, the T^*_e should be

$$T^*_e = T_r = d/v = d/\mu_e E, \tag{2.13}$$

Combining eq.(2.11),(2.12) and (2.13),

$$\eta = \frac{\mu_e \tau_e (E_0 + V_d/d)}{d} [1 - e^{-d/\mu_e \tau_e (E_0 + V_d/d)}], \tag{2.14}$$

The efficiency calculated by eq.(2.14) is plotted as solid line in Fig.2.2 (a).
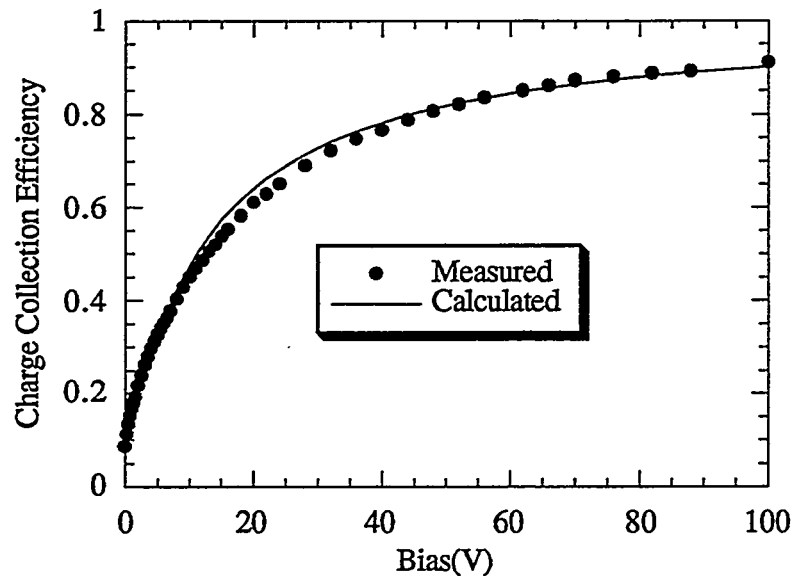
Fig.2.2 (a) Charge collection efficiency for various voltage bias for a 10 µm thick diode.

The signal size dependence of the shaping time was measured by exposing a short light pulse (200 ns) with wavelength 560 nm from the p side of the diode to simulate the scintillation light from CsI(Tl). The operating bias was set at - 100 volts on a 10 μm thick p-i-n diode. For this wave length light, only one type of carrier involves the signal formation as noted above, therefore, the signal measured by the external circuit is virtually all due to the collection of the electrons. For a p-i-n diode with 10 μm thick i layer the transit time of the electrons at a bias of 100V is less than 15ns. Fig.2.2 (b) shows the charge collection efficiency as a function of RC-CR shaping time.
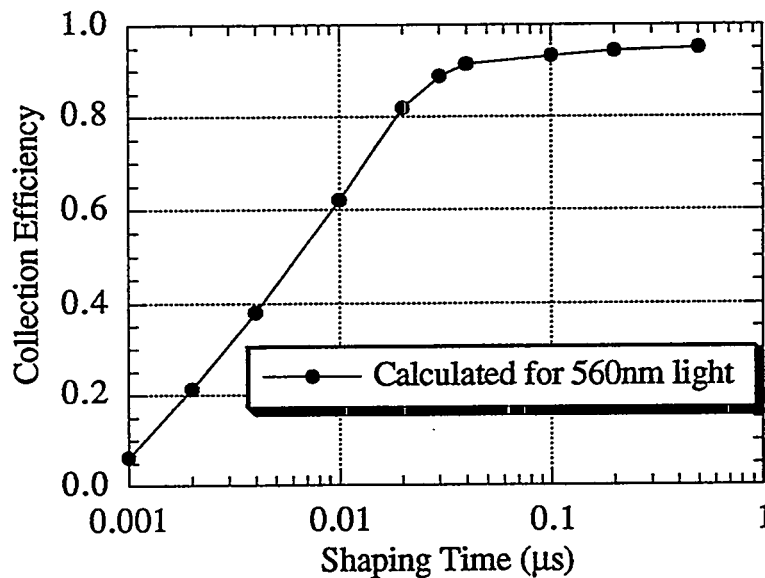
Fig.2.2 (b) Collection efficiency for different shaping times for 560nm light
on a 10 μm diode.

If the scintillation light is incident from the n side of the diode, the signal induced will be virtually all due to the collection of the hole charges with a longer collection time. The efficiency is lower than for electron charges, because an external signal occurs only when the whole thickness of the diode is depleted so that the hole can move toward the p side electrode. Thus when a p-i-n diode is operated at the voltaic mode (reverse bias), the

light is always incident on the p side of the diode. The charge collection comparison from p side and from n side is shown in Fig.2.2(a) and Fig.2.3.
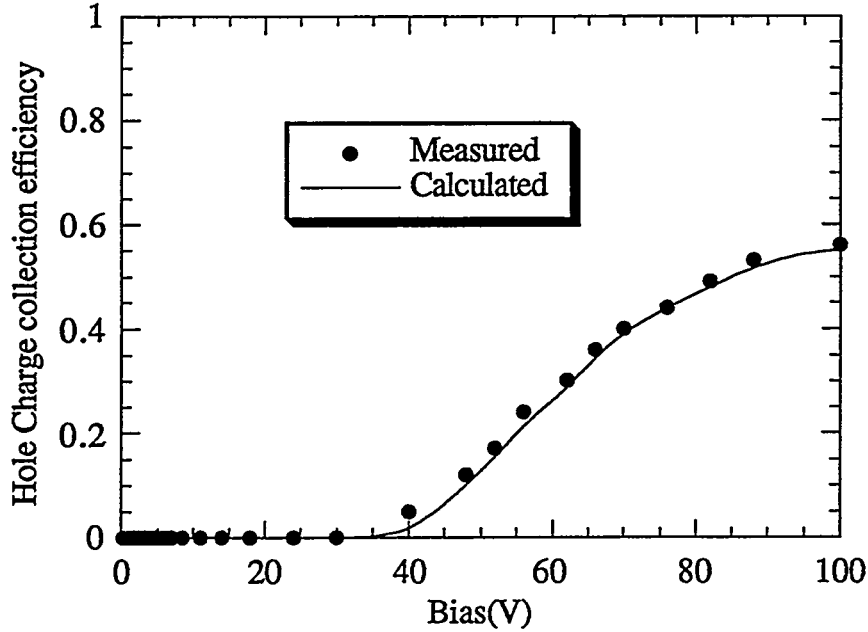
Fig. 2.3 Collection efficiency of holes in the cases of surface generation for a 10 μm thick sample. Dots are measured data from 560 nm light and lines are calculation results.

2.1.2 Optimizing the p-i-n diode

A typical spectral dependence of the charge collection, $Q(hv)$, of a 1 μm p-i-n device is shown in Fig.1.5. The collection efficiency reaches its peak value of 80% at wavelength between 500-600nm, indicating that there is little loss due to recombination. The reduction at the long wavelength is due to the decreasing absorption coefficient of a-Si:H, so that a smaller fraction of photons is absorbed in the device. The decreased collection efficiency at short wavelength has several origins. One cause is the absorption of light in the p or n layer, whichever is directly exposed to the incident light. The resulting carriers give virtually no contribution to the charge collection because of the relatively low

21

minority carrier lifetime in the doped layer, since most of the light absorbed in the doped layer is lost to recombination. For boron-doped a-Si:H, absorption coefficient is much larger than that for intrinsic or undoped layer(see Fig.2.4), thus the p layer absorption loss is often significant. The thickness of the p layer must be optimized; thin enough to minimize the light absorption and thick enough to prevent tunneling across the p-i junction and breakdown. The optical absorption coefficient α is[6]

$$(\alpha h\nu)^{\frac{1}{2}} = 6.9(eV\mu m)^{\frac{1}{2}}(h\nu - E_g), \qquad (2.15)$$
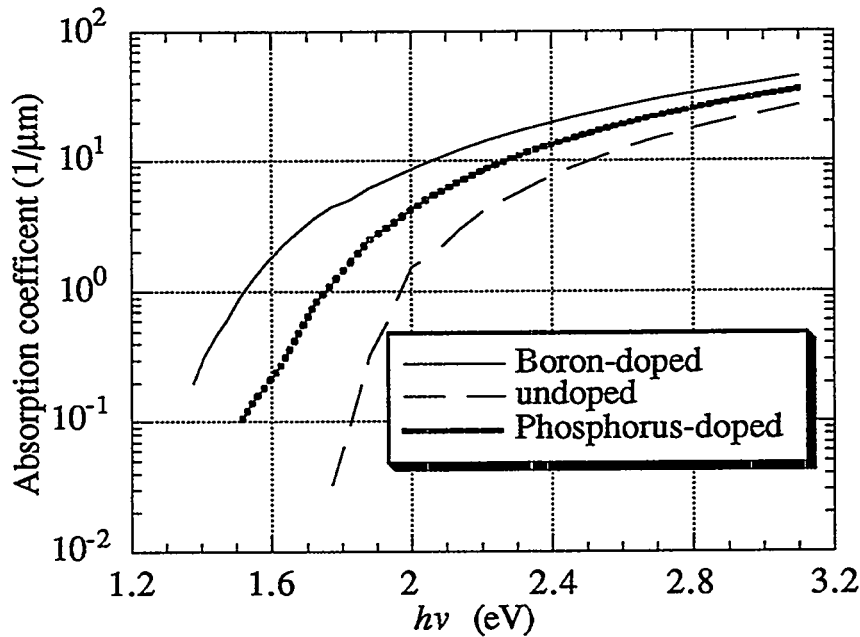
Fig. 2.4 Absorption coefficients for p-doped, n-doped, and intrinsic a-Si:H.

The loss due to the p layer was calculated for different thicknesses as shown in Fig.2.5. In the visible light region, such a loss can be significant. The p layer should be designed as thin as possible. However, for long wavelength detection or for minimum ionizing charged particle detection, p-layer absorption is negligible.
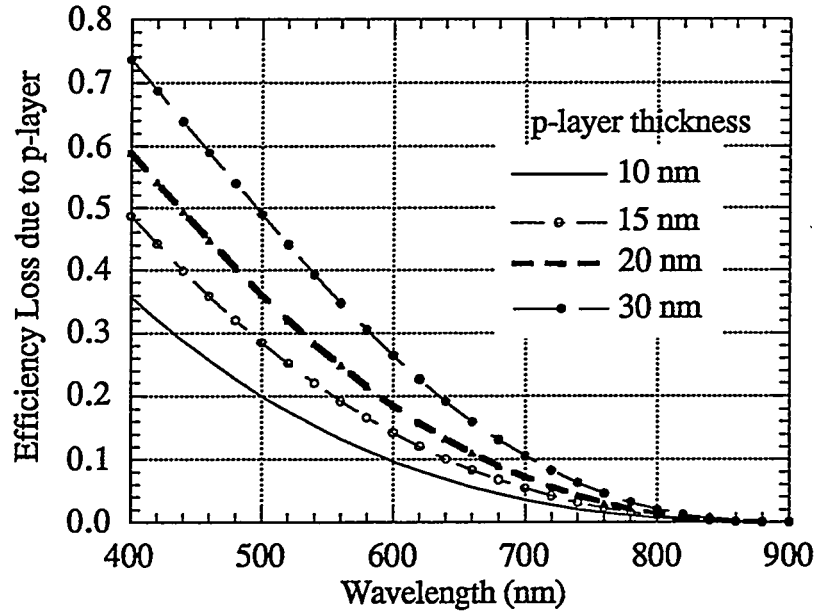
Fig. 2.5 Charge collection loss due to the absorption in the p-doped layer.

Two approaches can be used to modify the properties of the p-doped layer in order to minimize absorption loss. In one case, the absorption coefficient of the doped layers has been decreased to 50% of conventional doped a-Si:H by inducing the formation a microcrystalline phase. Microcrystalline Si:H films are formed by diluting the SiH_4 in H_2 and increasing the discharge power[7]. A second approach involves increasing the optical gap by alloying the boron-doped a-Si:H layer with carbon forming a-SiC:H (amorphous silicon carbide) which increases the optical gap from ~ 1.4 eV to 2.0 eV.

2.1.3 Back diffusion effect

The diffusion of carriers in the undoped layer against the internal field also reduces the collection efficiency. A thermalized carrier can, on average, diffuse over a potential of kT. Backward diffusion can therefore occur over a distance, x_D, of approximately

23

$$x_D = \frac{kT}{qE},$$ (2.16)

where E is the electric field. The estimated value of x_D is in the range of 35nm -90 nm[8,9]. The effect of back diffusion is most significant at high photon energy when the absorption length is less than 100 nm and the charge collection is reduced significantly at wavelength below 600nm. The back diffusion is further enhanced by hot carrier effects. At high photon energies, electron-hole pairs are created with a large excess energy which can rapidly diffuse 50-100 Å during thermalization to the band edges. This distance is independent of the applied field because the drift distance within a time of 10^{-12} second is negligible.
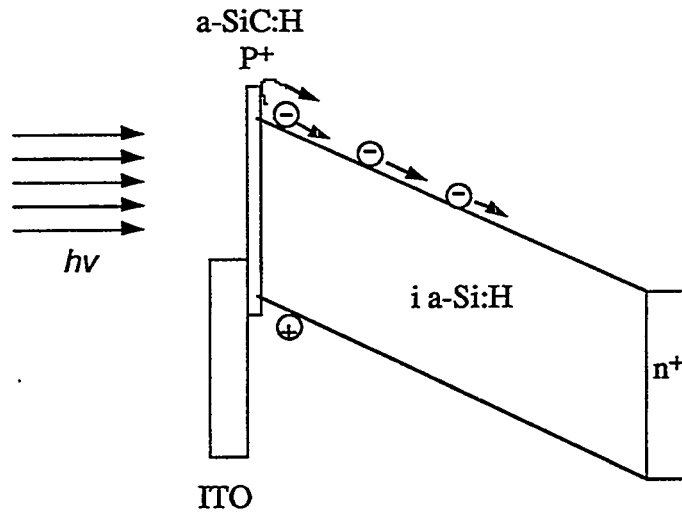
Fig.2.6 Band diagram of a-SiC:H p$^+$-i-n$^+$ device

To reduce back diffusion, p-type a-SiC:H is used for higher collection efficiency. Because the band gap of a-SiC:H (from 1.9 to 2.3 eV depending on the content of the carbon) is higher than a-Si:H, a barrier is formed to prevent the diffusion of the electrons as shown in Fig.2.6.

2.2. Reverse current

When a-Si:H p-i-n structures are used for solar cells, photo sensors, and charged particle detectors, the undoped layer is an efficient collector of electron-hole pairs generated by photon or charged particles because it has a low defect density. The doped layers provide the built-in field of the solar cell and blocking contacts for the detectors which are operated under reverse bias. The performance of both types of devices depends on the quality of the undoped layer and of the junctions to the doped layers. The dark current is a sensitive measure of the electronic performance of the material. Contributions to the dark current can be anticipated from contact injection, bulk thermal generation, and edge leakage.

2.2.1 Contact injection current

The injection current is determined primarily by electron injection through the p-i interface. Hole injection from the n layer to the i layer is negligible due to the low electric field at the i-n interface and due to the low hole mobility. The p layer functions as a barrier to prevent electron injection to the i layer. The different transport mechanisms across the barrier are illustrated in Fig.2.7. Thermionic emission refers to the excitation of the carriers over the top of the barrier where the conduction band edge intersects the interface. Tunneling through the barrier reduces the apparent barrier height and is significant when the internal field is large, which occurs when the applied voltage is high or the depletion layer is narrow. Tunneling into the localized states at band edge also causes a reduction in the height in the barrier height. Finally there can be field emission from the Fermi energy at high reverse bias, possibly via gap states.[10]

25
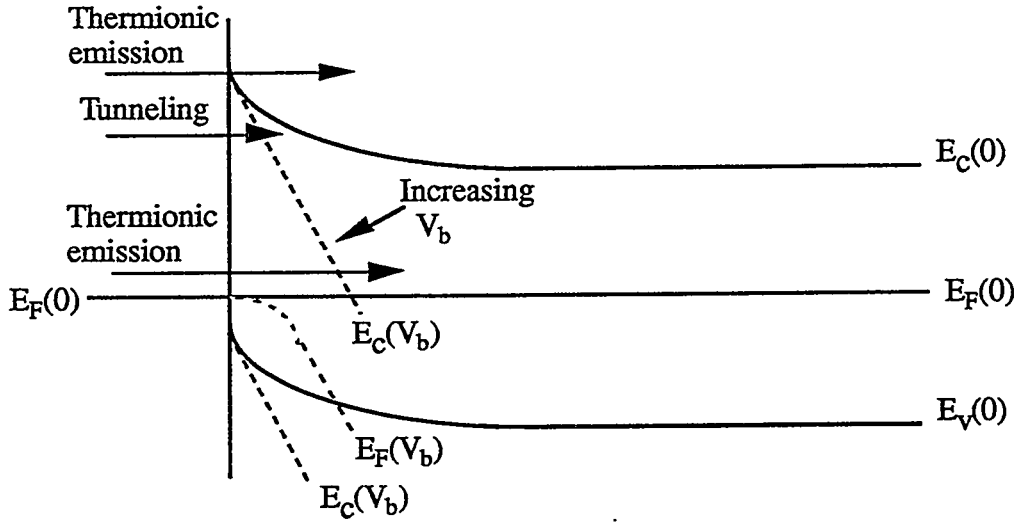
Fig.2.7 The three main mechanisms of electronic transport across the barrier. The dashed
lines represent the change in potential profile when a reverse bias V_b is applied.

We can treat the p-i interface as an effective Schottky contact to the i layer in terms
of electron injection. At zero applied voltage, the equilibrium current fluxes in each
direction are equal. The thermionic current density from the electrode over the barrier is

$$J_0 = A^* T^2 \exp(-e\Phi_b/kT) \tag{2.17}$$

where A^* is Richardson's constant (120 $Acm^{-2}K^{-2}$ for free electrons in vacuum)[11]. Φ_b is
the barrier height. The application of a bias V_b changes the current by a factor $\exp(eV_b/kT)$,
because the Fermi energy is raised or lower by eV_a with respect to the metal Fermi energy.
Thus,

$$J(V_b) = J_0 [\exp(eV_b/kT)-1] \tag{2.18}$$

In forward bias the current increases exponentially with V_b (when $V_b >> kT$) and
reverse bias the current saturates at J_0. From various Schottky barriers, J_0 can be
extrapolated from forward J-V data. J_0 is $10^{-12}-10^{-11}$ A cm^{-2}. Such a small value of J_0 can
not explain the reverse bias current in p-i-n devices. The larger current occur because the
junction is not ideal and tunneling across the barrier reduces the effective barrier height.

There may also be defective regions of the barrier where the leakage is particularly large. The current due to tunneling across the barrier is approximately,

$$J_{tunn} = J_0 \exp(E_m R_a/kT) \qquad (2.19)$$

where R_a is an effective tunneling length and E_m is the field at the contact. R_a is about 100 Å for a good junction[12]. The origin of R_a is unclear and its magnitude depends quite strongly on the deposition conditions.

2.2.2 Bulk thermal current

The thermal generation current represents the lowest dark current possible in a fully depleted sensor and can only be reduced by lowering the defect density or raising the band gap. Thick diodes have a correspondingly higher thermal generation current because J_{th} is proportional to the thickness. J_{th} arises from the excitation of electrons from the valence band to the empty gap states, and from the filled states to the conduction band. The contribution to the generation current from a single trap level is given by the Shockley-Read-Hall formalism[13]. Fig.2.8 shows a schematic diagram of the density of states distribution, $N(E)$, of a-Si:H showing the broad band of defect states near the middle of the gap.

For a continuous distribution of traps, the generation current is dominated by the emission from those traps with kT of an energy E_{FD}, for which the excitation rates for electrons and holes are equal. The thermal generation current, assuming full depletion and complete collection of excited electrons and holes, is given by Street[14].

$$I_{th} = eN(E_{FD})kT\omega_0\exp[-(E_c - E_{FD})/kT]Ad, \qquad (2.20)$$

where $\sim 10^{13}s^{-1}$ is the excitation rate prefactor, A is the area, and d the thickness. E_{FD} is a quasi-Fermi energy defining the occupancy of the localized states near midgap, and is determined by the thermal generation process. The condition for equal electron and hole

27
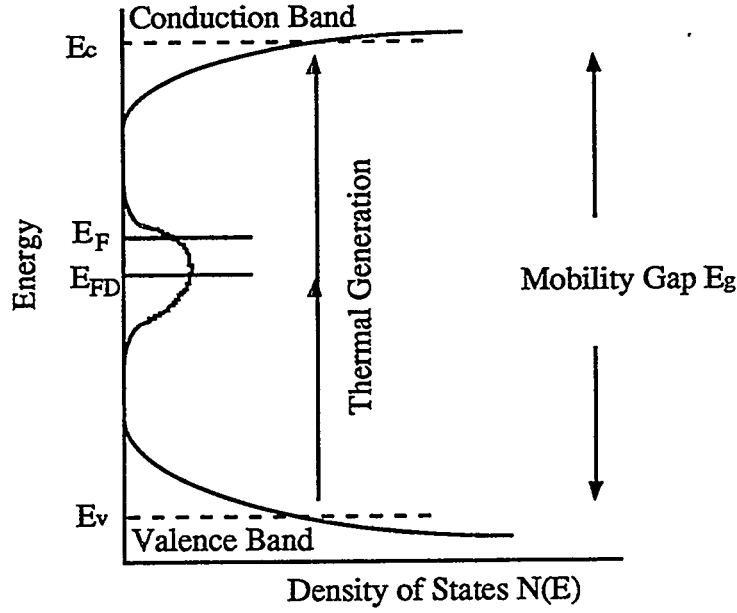
Fig.2.8 Density of states diagram showing the origin of the thermal generation current through gap states.

generation occurs very close to the middle of the gap. The rate prefactor is different for electrons and holes due to their different capture cross sections σ_e and σ_h, which shifts the quasi-Fermi energy to

$$E_c - E_{FD} = 0.5\, E_M + 0.5\, kT\, \ln(\sigma_e/\sigma_h), \qquad (2.21)$$

where E_M is the mobility gap energy. Since σ_e/σ_h is of order 0.1, the shift is negative and about 30meV. The value of $E_c - E_{FD}$ is therefore expected to be 0.9-0.95.[14]

For a good material, the ionized dangling bond density $N(E_{FD})\Delta E$ of depleted p-i-n diodes is about $7\times10^{14}/cm^3$[15]. $\Delta E = E_F - E_{FD} = 0.1$ eV. Combining these values, the predicted thermal generation current will be

$$I_{th} = 1.5 \times 10^{-7} Ad \ A/cm^3, \qquad (2.22)$$

For a film thickness of $1\mu m$, the current density is

$$J_{th} = 1.5 \times 10^{-11} \ A/cm^2,$$

This result only applies to a good quality thin a-Si:H photodiode as a good approximation at low bias. However, with high reverse bias, the strong non-uniform electric field in the

28

depleted region enhances the emission of electrons and holes significantly. The main source of field enhanced emission is the Poole-Frenkel effect[16], also called the internal Schottky effect. Such effect is the field-enhancement of thermal emission from localized states to the conduction states due to barrier lowering as shown in Fig.2.9
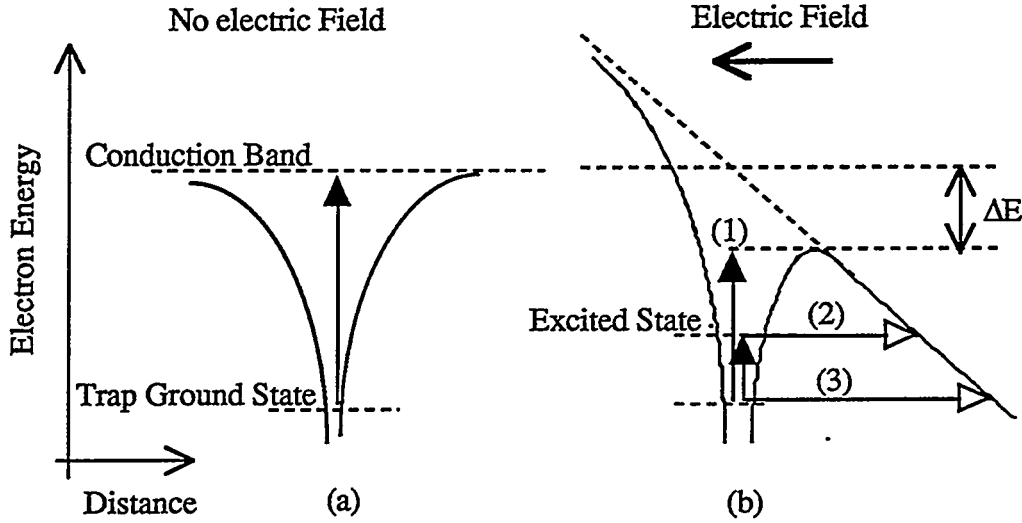
Fig. 2.9 Mechanisms of electron generation from recombination centers (a) Simple thermal generation, (b) Three effects of strong electric field; (1) Poole-Frenkel barrier lowering, (2) phonon assisted tunneling and (3) direct tunneling.

Arrow ↑ represents a thermal emission process and → represents a field emission process.

Such bulk current was formulated as

$$J_{PF} = \frac{J_{th}2kT\sqrt{E_m}}{d\beta_{PF}} \exp(\beta_{PF}\sqrt{E_m}/kT),$$ (2.23)

where β_{pf} is the Poole-Frenkel constant defined as

$$\beta_{PF} = \left(\frac{q^3}{\pi\varepsilon_0\varepsilon_{Si}}\right)^{\frac{1}{2}} \approx 0.002 \left(eV\sqrt{\mu m/V}\right),$$ (2.24)

α is the slope of the electric field or space charge density in the deep depletion region given by

$$\alpha = \frac{qN_d^*}{\varepsilon_0\varepsilon_{Si}},$$ (2.25)

29

where ε_0 is the permittivity in vacuum and ε_{Si} is the relative dielectric constant of a-Si:H. E_m is the peak electric field at the p-i junction,

$$E_m = V_b/d + 0.5\alpha d, \tag{2.26}$$
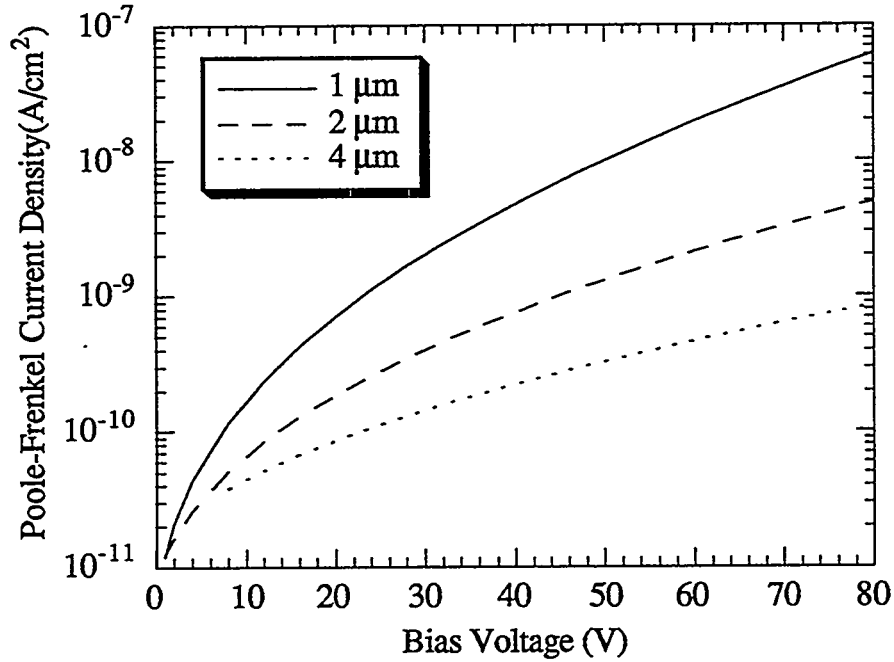
Fig.2.10 Calculated poole-Frenkel current from a Coulomb potential well with 0.9 eV barrier height at room temperature.

The calculation results based on above equations are shown in Fig.2.10. It is easy to see that the Poole-Frenkel emission in the depletion region dominates the bulk current even at a low bias. To reduce this P-F effect, as shown in eq.(2.23), the peak electric field E_m should be reduced. One way to accomplish this is to use a buried lightly doped p layer inside the intrinsic region of a-Si:H[17,18]. The E_m could be reduced by a factor of two by depositing a p layer in the middle of the diode.

2.2.3 Edge leakage current

The dominance of the bulk generation current at low bias implies that contribution to the reverse current from other sources is significantly lower. However, some devices of the same structure have a larger reverse current, for example, at higher bias, or small pixel size. Except for the contact injection, current leakage around the electrode may also contribute to the total reverse current.
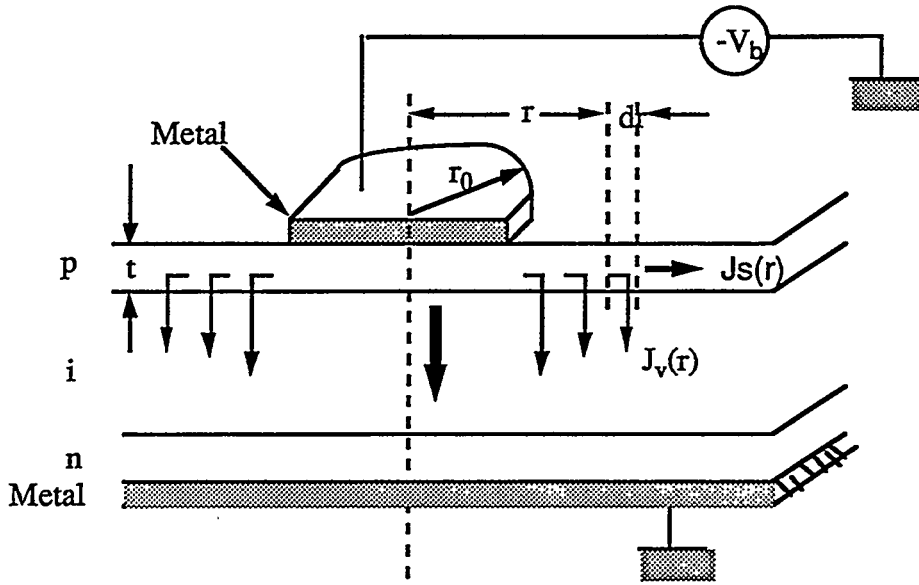
Fig. 2.11 A p-i-n diode showing the currents flowing through the diode.

Consider the dimensional schematic of the currents flowing in a p-i-n diode illustrated in Fig.2.11. Let $J_s(r)$ be the surface current for $r > r_0$ (r_0 is the electrode diameter) in the top doped layer at a distance r away from the center of the electrode, J_v the reverse current density flowing vertically through a cylindrical shell of thickness dr. Applying Ohm's law to the top layer we get

$$dV(r) = -J_s(r) \, (dr/\sigma), \tag{2.27}$$

where $V(r)$ is the potential at a distance r in the top doped layer, σ the top layer conductivity. Differentiating eq.(2.27) yields

$$\frac{d^2V}{dr^2} = -\frac{1}{\sigma}\frac{dJ_s(r)}{dr}, \qquad (2.28)$$

Note that the surface current decreases along r due to the vertical current flowing J_v. Thus,

$$2\pi rtJ_s(r) = 2\pi rtJ_s(r + \Delta r) + 2\pi r\Delta rJ_v(r), \text{ or}$$

$$t\Delta J_s = -\Delta rJ_v(r), \qquad (2.29)$$

Therefore equation (2.28) becomes

$$\frac{d^2V}{dr^2} = \frac{J_v(r)}{t\sigma}, \qquad (2.30)$$

a linear behavior of J_v-V is normally observed

$$J_v = kV(r), \qquad (2.31)$$

where k is a constant determined by measurement, $\sim 0.5\text{x}10\text{-}11\ \Omega^{-1}\text{cm}^{-2}$, equation (2.30) then becomes

$$\frac{d^2V}{dr^2} = -\frac{kV(r)}{t\sigma}, \qquad (2.32)$$

Thus the solution for equation (2.32) is

$$V(r) = V_b\exp(-\sqrt{\frac{k}{t\sigma}}(r\text{-}r_0)), \qquad (2.33)$$

Then, the leakage current density is

$$J_v(r) = kV_b\exp(-\sqrt{\frac{k}{t\sigma}}(r\text{-}r_0)), \qquad (2.34)$$

When a-Si:H p-i-n diode is designed as a photosensor, it is thin and can operate at low reverse bias. The bulk generation current due to Poole-Frenkel effect and the tunneling current are negligible. Components of the reverse current are the thermal generation current and the edge leakage current. To compare relative contribution to total reverse current from thermal generation and from the edge leakage, we should consider their currents instead of current densities. The thermal current simply is

$$I_{th} = \pi r_0^2J_{th}, \qquad (2.35)$$

The edge leakage current is obtained by integrating J_v from to ∞

$$I_v(r) = 2\pi k V_b \sqrt{\frac{k}{t\sigma}} (\sqrt{\frac{k}{t\sigma}} + r_0), \qquad (2.36)$$

Fig.4.12 shows the relative importance of the reverse current components from thermal generation and from the edge leakage at a low bias. When the diode size becomes smaller, the surface leakage will surpass the thermal current and dominate the dark current. Thus when designing small pixel diodes, the surface treatment around the electrode needs to be considered.
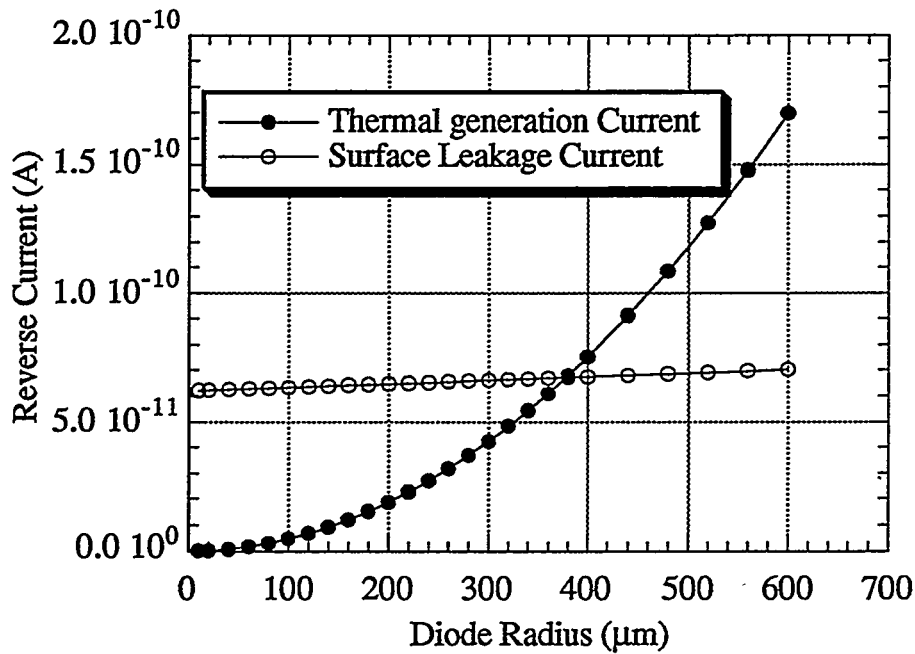
Fig.2.12 Thermal generation and edge leakage currents for different sizes of sensors

2.2.4 Effect of a p-type a-SiC:H layer on the dark current

A p-layer as a blocking contact in a photodiode is important for a low dark current. The optimization of the p layer dopant depends on the B_2H_6 flow rate. Fig.2.13 shows the dependence of the photodiode dark current on the B_2H_6 flow during the deposition of the p-type a-SiC:H layer. The photodiode dark current decreases with increased B_2H_6 flow up to

12 sccm due to the decreased electron injection from the ITO electrode to the a-Si:H photo-electric conversion layer. This dark current increases in the B_2H_6 flow range over 12 sccm, possible due to the generation of defects caused by the diffusion of excessively doped B into the a-Si:H layer and more injection current raised from electron hopping through defect states to reach the p-i interface and then tunnel to the conduction band. The p-type layer has high defect density in the gap[19].
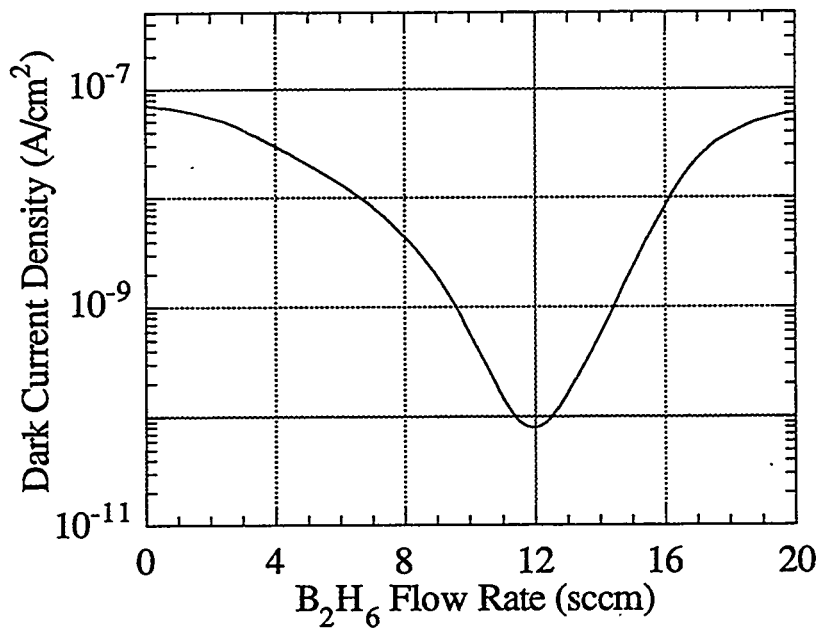
Fig.2.13 Dark Current density as a function of B_2H_6 flow rate for p-layer deposition.

2.2.4 Summary

The reverse current originates from contact injection, bulk thermal generation, and edge leakage. At low applied bias, thermal generation current contributes most to the dark current. Under high bias, the contact injection dominates the dark current. Thermal generation will decrease rapidly with lowering temperature and tunneling may become important. For a thick p-i-n diode, the Poole-Frenkel effect may occur at the high field region near the p-i interface and increase dark current. One way to avoid such effects is

artificially shaping the electric field across the device by inserting one or more lightly doped thin p layers inside the intrinsic region. When the size of diode needs to be small < 300 μmx300 μm for better resolution imaging, the edge leakage will dominate the dark current. An appropriate passivation needs to be implemented, such as oxidation of the nonactive doped layer or etching away the unnecessary layer.

2.3 Sensor Operation

The readout of an image sensor is characterized by switching a large number of sensor elements in sequence to a single output for recording their signals. In an array with a total number of N elements scanned with a frequency f_0, each element in the array is then periodically addressed for $\Delta t = 1/f_0$ seconds every $N\Delta t$ seconds. The elements can be operated in two modes: storage and non-storage mode.

In the non-storage mode the instantaneous photocurrent I_{ph} in the sensor element is measured within a short time interval Δt when addressed during scanning. The non-storage mode is consequently used mainly with photoconductive elements having a photoconductive gain much greater than unity.

In the storage mode, the photocurrent in an element, or the photogenerated charge in a pixel is integrated in each pixel's capacitance during readout of all the other elements until it is addressed again. The capacitance may be that of a discrete capacitor connected to the pixels, or it may arise from the internal shunt capacitance of the element itself.

In the storage mode, reverse-biased photodiodes are generally used. Such a diode may be considered as a combination of a capacitance and a light-controlled current source independent of the applied voltage. The storage mode is based on the principle that in a reverse-biased diode with floating electrodes an electrical charge in the diode capacitance decays at a rate proportional to the illumination, due to the independence of the photocurrent from the applied voltage in photodiodes[20].

Photoconductors combined with a discrete capacitor can also be used in storage mode. However, in this case the photocurrent under continuous illumination changes during the charge storage process because of the inherent voltage change at the capacitance.

(a)

(b)
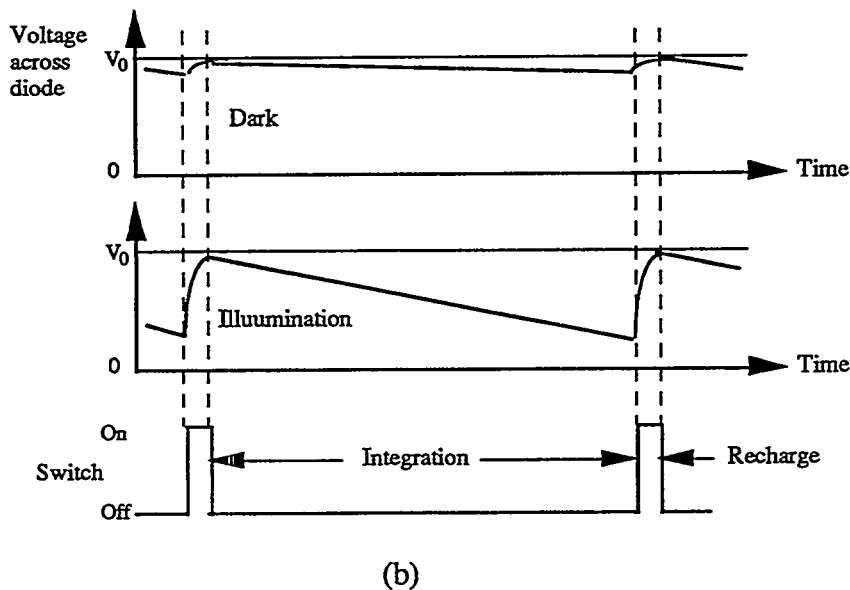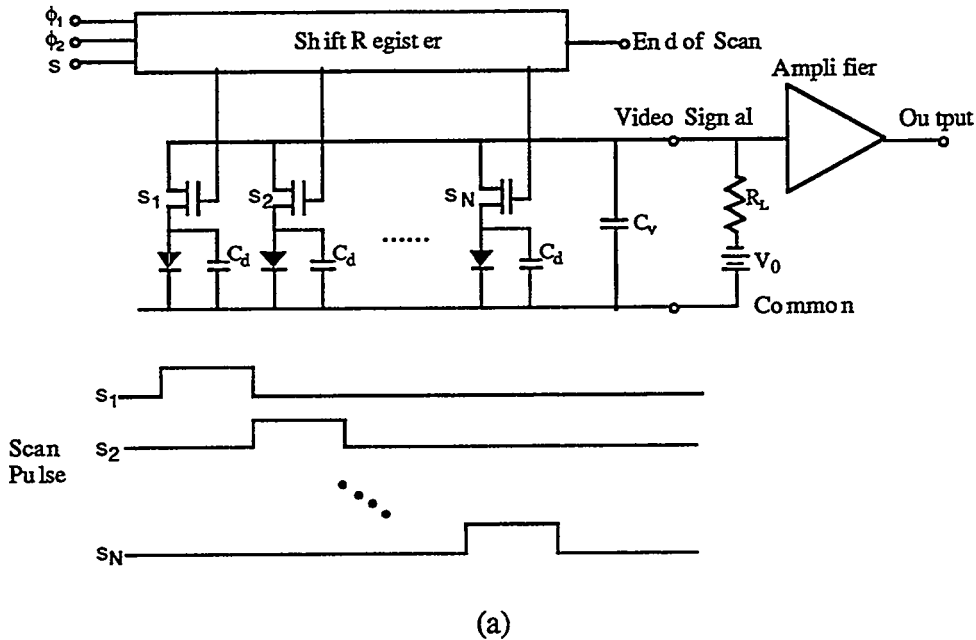
Fig.2.14 Operational model for the charge storage mode: (a) linear array of photodiodes connected to transfer switches(TFT); (b) storage and readout of the charge generated in a photodiode.

36

The capacitance of a thin-film photodiode in an image sensor application is mainly given by its geometrical capacitance, because the diode is under depletion when reverse biased,

$$Cs = \varepsilon_0 \varepsilon_r f A / d \qquad (2.37)$$

where ε_0 and ε_r, are the dielectric constants, and $\varepsilon_r = 12$ for a-Si:H. A is the area of the diode, d the thickness.

Fig. 2.14 shows the principle of the storage mode in the example of a linear array of photodiodes connected to switches, sequentially addressed by scan pulses. Charge storage requires an RC constant of the diode in series with the switch in the offstate to be longer than the integration time, and therefore requires a low dark current of the diode and a low leakage current of the switch in the off state. When the switch is turned on, once in every line scan, the diode capacitance is reset to the applied voltage V_0, as shown in Fig. 2.14(b). The recharge current, replacing the charge removed by the dark or the I_{ph}, generates a voltage signal across the external load resistor R_L, which represents the total exposure during the line-scan time. Another requirement for the switches results from the demand for complete charge transfer during the addressing time Δt when the switch is closed: the RC constant of the diode capacitance C_s in series with the on-resistance R_{on} of the switch and the external load resistor R_L has to be much smaller than the addressing time Δt. The shunt capacitance across the switch should be much smaller than that of the diode, to avoid problems due to parasitic capacitances.

In general, parasitic capacitances are of importance for the performance of image sensor arrays operating in storage mode. Depending on the details of the sensor design, the readout circuitry and the signal processing, they result in signal reduction and in crosstalk of sensor signals and noise. Signal nonuniformity along the sensor array is due to the nonuniformities of these capacitances.

2.4 Position-Sensitive Radiation Detectors

In some cases, the position and transit time of each particle is of interest and recorded as such by the configuration of detector structure and its associated detecting electronics. Position sensitive devices of this type often consist of a large area detector subdivided into strips or pixels. The signal from each strip or pixel is readout by associated electronics as described in following.

2.4.1 TFT readout schemes for 2-D array

Fig.2.15 shows a pixel array in which each element is read out by an a-Si:H switching transistor. The array can be read out line by line by sending out an enable signal to the TFT in that line. The charge in the elements in the tagged line can be read out by some integrated circuit chip with multiple inputs such as the SVX chip made at the Lawrence Berkeley Lab. This chip has 128 parallel low noise inputs and other features[21].
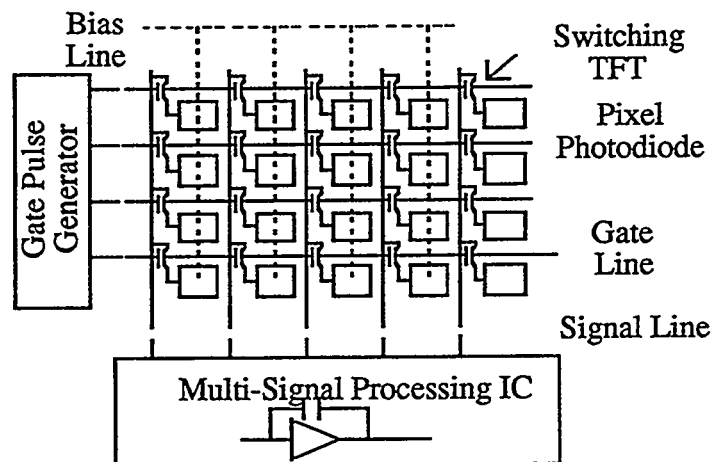
Fig. Fig.2.15 TFT readout scheme.

2.4.2 Diode switching for 2-D array

Alternative readout methods involve a single diode connected to each element Fig.2.16(a)[22], or two diodes as shown in Fig.2.16(b)[23]. The two diode readout is faster and has a larger dynamic range than the single diode scheme; it also minimizes switching transients. Diode readouts have the following advantage compared to TFT (a) they require fewer production masks (b) by not needing a SiO_2 or Si_3N_4 insulator they minimize radiation damage problems.
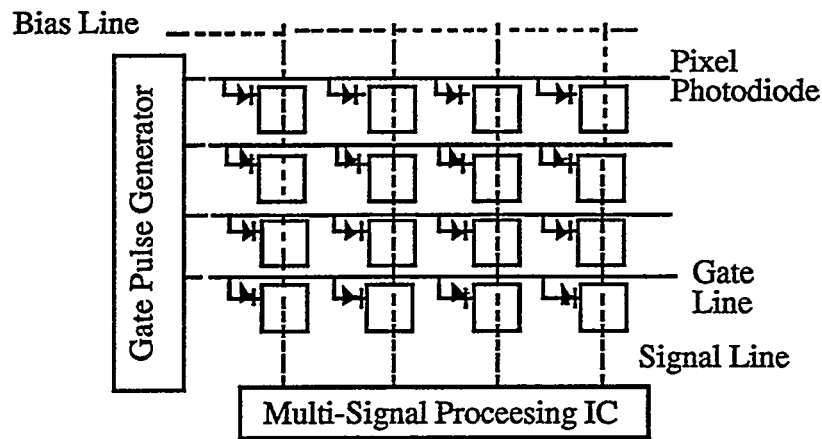
(a)
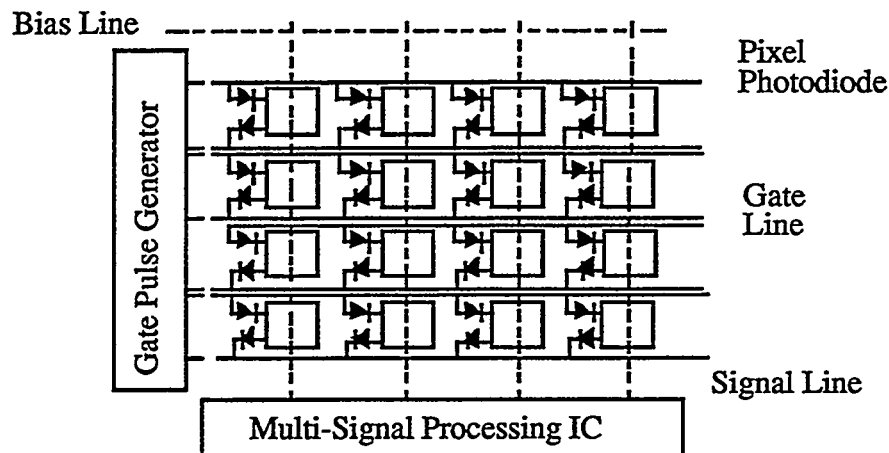
(b)

Fig.2.16 Diode readout schemes (a) single diode (b) two diode switches

2.5 Thin Film Transistor (TFT)

2.5.1 Comparison of a-Si:H and poly-Si TFT

Polycrystalline silicon is composed of grains with each grain containing a periodic array of atoms surrounded by a layer of interconnective or boundary atoms. TFTs of a-Si:H or poly-Si can both be used to switch pixels in imaging arrays or in flat-panel displays[24-28]. A-Si:H TFT are more developed than poly-Si TFT, but the latter offer some performance advantage. A-Si:H can be deposited at low temperature <350°C, which permits the use of a cheap substrate. Poly-Si TFT were first developed at 950°C, thereby limiting the choice of substrate to quartz. A mid-temperature process(550-600°C) for producing poly-Si is under developement[29]. A new process to crystallize a-Si:H by laser annealing into poly-Si seems to be promising; some problems arise with such a crystallization process, such as, overlay zone, nonuniformity of the grain size[30,31].

Electron mobility for the high temperature (HT) poly-Si devices is 100 $cm^2V^{-1}s^{-1}$ compared with 40 $cm^2V^{-1}s^{-1}$ for the mid-temperature poly-Si device. The most pronounced difference between HT and LT technologies is the pchannel performance. The threshold voltage is 8.5 V and the mobility is 13 $cm^2V^{-1}s^{-1}$ for the LT TFT, compared with -2.6 V and 50 $cm^2V^{-1}s^{-1}$ for the HT TFT.

The a-Si device has a mobility of 1 $cm^2V^{-1}s^{-1}$ and therefore, has considerably less drive current than poly-Si TFTs. However, a-Si TFT has several order of magnitude higher Off resistance than the poly-Si TFT, thus a-Si TFT is a first choice for a switch for large area image sensor arrays or for activated-addressing flat-panel display at present..

2.5.2 Thin-Film Transistor Structure

A number of TFT structures have been reported. We chose the top gate structure for a-Si:H and poly-Si TFT as readout switches as shown in Fig.2.17. A-Si:H TFTs are

normally composed of a thin (~ 0.5 μm) a-Si:H i layer as a main current channel and amorphous silicon nitride of 0.3 μm as a gate insulator. The major feature of this TFT is that all the PECVD films are deposited successively, so that the interfaces between undoped aSi:H and insulator layers are hardly affected by contamination during the fabrication process.

Drain   Source

Cr
a-Si:H (500 nm)
Si_3N_4 (300 nm)
Substrate

Gate Cr

(a)

Gate

Poly-silicon

SiO_2 (200 nm)

Substrate

Drain   Source

(b)
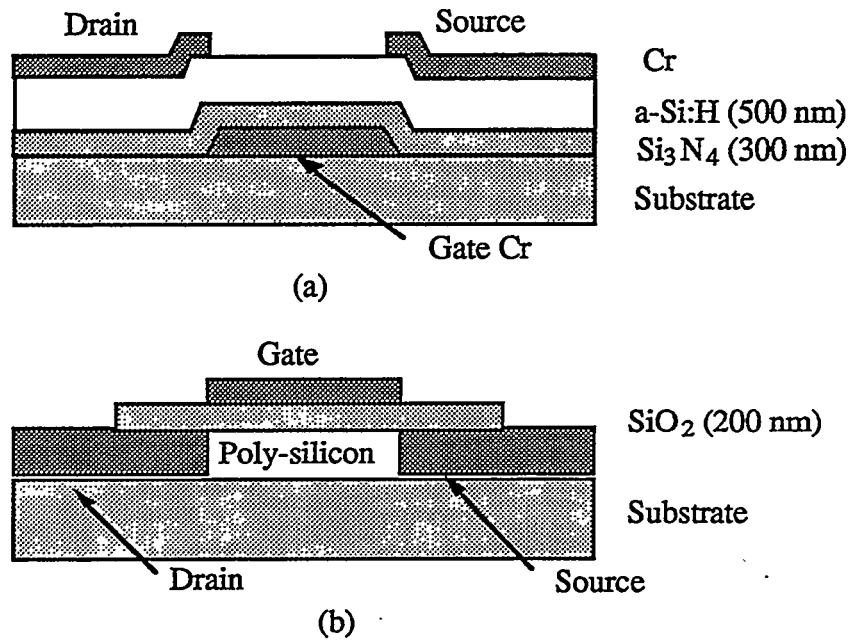
Fig.4.17 Schematic cross-sectional views of (a) a-Si:H and (b) poly-Si TFTs.

Some other materials such as silicon oxide and tantalum oxide [32] are used as gate insulators; however, their characteristics are not reliable. a-Si:H TFTs are the staggered-inverted type as shown in Fig. 2.17(a), and channels are defined by a self-aligning technique using gate metal as a mask for photo-etching by shining light through the glass substrate. Because of the low hole mobility, only n-channel a-Si:H TFTs are practically applicable and they are operated in the accumulation mode which means the electrons are accumulated at the interface of the gate insulator and the intrinsic a-Si:H layer (slightly n-type) under the positively biased gate.

Poly-Si TFTs are becoming very important elements in making driver circuits for large-area image devices such as LCD screens[33] and 2-D scanners because of their

41

capability for fast speed and reliable operation. Both n-channel and p-channel TFTs can be made by ion-implantation doping followed by a high temperature annealing. The sample TFTs described here were made by the annealing technique at Xerox and its schematic diagram is shown in Fig.2.17 (b).

2.5.3 Thin-Film Transistor-Driven Sensors

In TFT-driven sensors every photosensitive element is connected to a corresponding thin-film transistor. For sensor operation the charge storage mode is usually selected.

Charge Transfer

Measurement and computer simulation of the signal transfer from a single photodiode via a TFT to the readout capacitance at the entrance of a multiplexing circuit is shown in Fig. 2.18. Fig.2.18(a) shows the circuitry under consideration. The multiplexing circuit common to matrix-wired TFT-driven sensors has been replaced by a simplified circuit comprising a voltage follower and a reset switch for the readout capacitance.

The signal voltage ΔV_s across the diode at the end of the integrating time is due to the light-induced photocharge, Q_s and the diode capacitance, C_s:

$$\Delta V_s = Q_s/C_s, \tag{2.38}$$

For readout at the end of the integration time, the TFT is switched on by changing the gatevoltage from $V_{g,off}$ to $V_{g,on}$. This voltage change $\Delta V_g = V_{g,on} - V_{g,off}$ at the gate is fed through to the output because of the gate capacitance and other capacitances. This effect is best seen with the dark signal train in Fig.2.25, as in this case there is practically no further contribution by the photodiode. The voltage change in the readout circuit due to the switching noise is given by

$$\Delta V_n = \Delta V_g(\Delta C_{g,on}/C_{on}), \tag{2.39}$$

with the capacitance $C_{g,ro} = C_{g,s} + C_k$ between gate and readout line, which results from

42
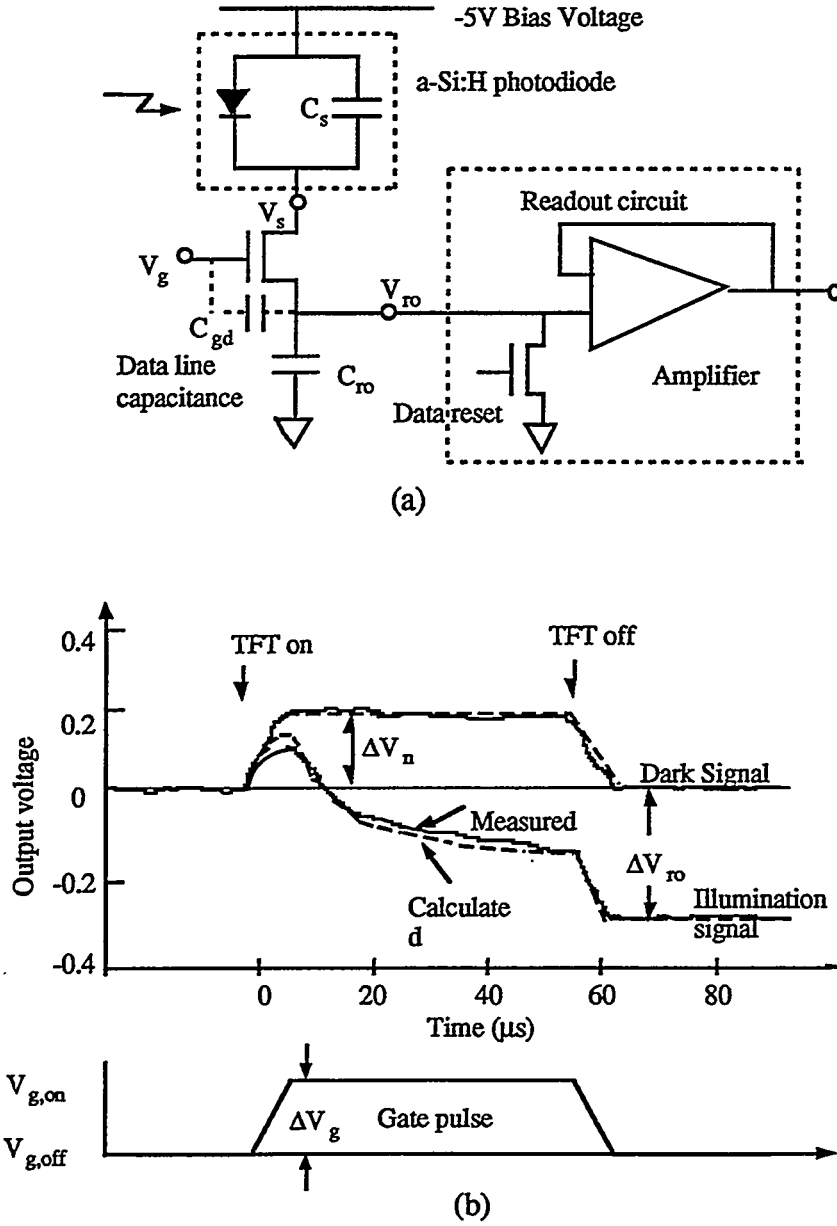
Fig.2.18 (a) a-Si:H photodiode/TFT pixel circuit; (b) charge transfer from photodiode via a TFT during readout.

the gate-source capacitance $C_{g,s}$ and the coupling capacitance C_k between the gate line and the readout line, and the readout capacitance C_{ro} of the readout line to the ground plane.

The signal charge Q_s from the photodiode is transferred via the on-resistance R_{on} of the TFT to the readout capacitance with the time constant:

$$t_{ro} = R_{on}C_s, \tag{2.40}$$

43

if the readout capacitance C_{ro} is much larger than the capacitance C_s of the photosensitive element which is the usual case in practice.

The signal voltage $\Delta V_{ro}(t)$ at the output, a function of the time t, is then given by

$$\Delta V_{ro}(t) = \Delta V_s(C_s/C_{ro})(1-\exp(-t/t_{ro})), \tag{2.41}$$

As $C_{ro}>>C_s$, almost complete charge transfer is possible and the photodiode is thus reset.

Switching off the TFT again gives rise to a switching pulse of about the same height but opposite sign compared to the switching-on pulse. After switching off the TFT, the photocurrent integration in the diode capacitance starts again. The signal voltage is transferred to the output by a multiplexing circuit and then the readout capacitance reset by discharge via a reset switch. In general these time constants can be made sufficiently small.

A problem of TFTs is their threshold voltage shift in the course of applied voltage stress. However, when the TFT operates merely as a switch, such a voltage shift has been shown to be tolerable over a range of several volts[34]. This is because it only influences the time constant for the charge transfer. If the threshold voltage is too high, the transfer time is too long, while if the threshold voltage is too low, the transistor does not switch off correctly and the signal is reduced due to leakage during the integration time. Due to the threshold voltage shift, the voltage bias at the diode also changes. All this has to be taken into consideration for the choice of an appropriate operating voltage.

Sensor with TFT preamplifier

An approach to overcome a poor *S/N* ratio would be to integrate an amplifier with each sensor pixel. In this case, stable properties of the TFTs are of particular importance. Fig.2.19 shows the circuit for a charge-sensitive amplifier, which integrates the photocurrent from an sensor element and produces an output voltage which depends quasi-linearly on the light intensity incident on the sensor pixel [35]. When the sensor element is in the dark, the output voltage is low, because the gate and the drain voltage are almost

equal due to the low dark current flowing through the feedback capacitor. The gate voltage adjusts to a value just above the threshold voltage of the TFT. The achievable gain for the amplification of the gate voltage depends on the values chosen for the resistors. A typical gain value is between 10 and 20, limited by the required speed response of the amplifier.

A-Si:H TFT can only be used as switching devices because the threshold voltage of the gate bias shifts continuously under D.C. bias. True CMOS amplifiers can be made using polysilicon TFT since both electron and hole mobilities are comparable and much higher than the corresponding ones for a-Si:H TFT as show in Table 2.1.

Table 2.1. Typical properties of a-Si:H and polysilicon TFTs

Type	a-Si:H TFT	Poly-Si TFT
μe $(cm^2/Vsec)$	1	150
μh $(cm2/Vsec)$	.005	80
gm $(\mu A/V)$	5	150
Bandwidth(MHz)	5	100
Noise* (e)	500	500

* Equivalent noise charges for an CR-(RC)4 shaping time of 1 μsec.
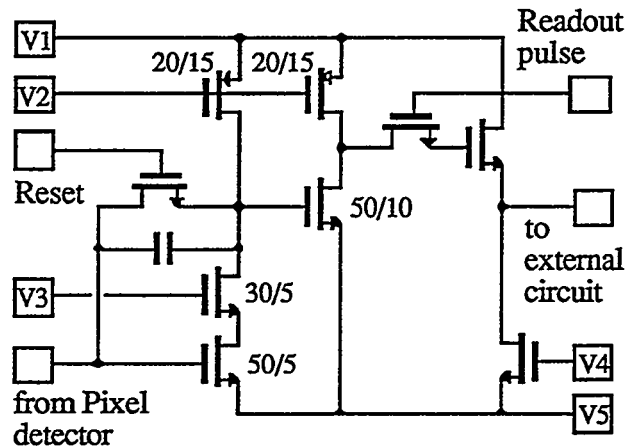
Fig.2.19 Polysilicon TFT charge sensitive amplifier

45

Using the facilities of the Xerox research lab in Palo Alto, our group designed and tested 3-stage CMOS polysilicon amplifiers with a charge sensitive input stage followed by a voltage gain stage, and a low impedance output stage for driving signals through a pixel array. This prototype amplifier design is shown in Fig.2.19. The measured characteristics are given below in Table 2.2 [36].

Table 2.2. Characteristics of polysilicon TFT charge-sensitive amplifier

Dimension	<200x200 μm^2
Charge gain	~0.02 mV/electron
Rise time	100nsec
Gain-Bandwidth	350 MHz
Noise	~1000 electrons
Power dissipation	< 1 mW/pixel

Fully Integrated Sensor with Poly-Si TFTs and a-Si:H Photodiodes

Due to higher carrier mobility, the on-resistance of a poly-Si TFT is much lower than that of a conventional a-Si:H TFT of the same size. Thus, charge transfer is faster, which allows for direct addressing of the elements according to the fundamental readout circuit. The off-resistance of a poly-Si TFT, however, is lower than that of an a-Si:H TFT, which requires reduction of the gap width for low leakage current. A sensor of this kind is superior to one with IC chips, mainly because of the suppression of parasitic capacitances due to integration, and also because matrix wiring is avoided.

The processing temperatures for poly-Si are currently 600°C for deposition and 1000°C for oxidation and annealing, which leads to severe warpage problems in the lithographic steps when using nonsilicon substrates[37]. The thermal expansion coefficients of Si ($1.9x10^{-6}$ K^{-1}) and of the suitable substrate material, fused quartz ($0.54x10^{-6}$ K^{-1}), differ widely. This disadvantage limits the use of poly-Si when the substrate size increases.

References

[1] M. Hack, M. Shur, and C. C. Tsai, "Amorphous Silicon Photoconductive Diode," Appl. Phys. Lett., 54, 96 (1989).

[2] T. Jing, J.C. Delgado, J. Bertomed, J.S. Drewery, W.S. Hong, H.K. Lee, S.N. Kaplan, A. Mireshghi, V. Perez-Mendez, "Charge Collection in a-Si:H/a-Si$_{1-x}$C$_x$ Multilayer Photodetectors," Presented at II Intl. Conf. on Thin Film Physics and Application, Shanghai, China, (April 1994). SPIE Vol.2366 p.345-350 (1994).

[3] S. Qureshi, V. Perez-Mendez, S. N. Kaplan, I. Fujieda, G. Cho, and R. A. Street, "Material Parameters in a Thick Hydrogenated Amorphous Silicon Detector and Their Effect on Signal Collection," Mat. Res. Soc. Symp. Proc., Vol. 149, p. 649 (1989).

[4] G. Cho, Ph. D. Thesis, *Signal and Noise Analysis of a-Si:H Radiation Detector-Amplifier System*, p.34, (1992).

[5] S. Ramo, " Currents Induced by Electron Motion," *Proc. I.R.E.*, Vol. 27, pp. 548, 1939.

[6] A. Madan, M. P. Shaw, *The Physics and Applications of Amorphous Semiconductors*, Academic Press, Inc., p. 68 (1988).

[7] A. Mireshghi, W.S. Hong, J.S. Drewery, T. Jing, S.N. Kaplan, H.K. Lee, V.and Perez-Mendez, "Improved Electrical and Transport Characteristics of Amorphous Silicon by Enriching with Microcrystalline Silicon," Mat. Res. Soc. Symp. Proc., Vol. 336, p. 377 (1994).

[8] A. R. Moore, "Electron and Hole Drift Mobility in Amorphous Silicon," Appl. Phys. Lett. 31, 762 (1977).

[9] D. L. Staebler and C. R. Wronski,"Optical Induced Conductivity Changes in Discharge-produced Hydrogenated Amorphous Silicon," J. Appl. Phys. Vol. 51, p. 3262 (1980).

[10] E. Rosencher, V. Mosser and G. Vincent, "Transient-Current Study of Field-Assited Emission from Shallow Levels in Silicon," Phys. Rev. B, Vol. 59, 1135 (1984).

[11] R. A. Street, *Hydrogenated Amorphous Silicon*, Cambridge university Press, p.327 (1991).

[12] R. A. Street, *Hydrogenated Amorphous Silicon*, Cambridge university Press, p.372 (1991).

[13] W. Shockley and W. T. Read, "Statistics of the Recombination of Holes and Electrons," Phys. Rev., 87, 835 (1952)

[14] R. A. Street, "Thermal Generation Current in Hydrogenated Amorphous Silicon p-i-n Structures," Appl. Phys. Lett., 57, 1334 (1990).

[15] S. Qureshi, V. Perez-Mendez, S. N. Kaplan, I. Fujieda, G. Cho and R. A. Street, "Material Parameters in Thick Hydrogenated Amorphous Silicon Radiation Detectors," J. Non-Crystalline Solids, Vol. 114, 417 (1989).

[16] J. Frenkel, "On Pre-Breakdown Phenomena in Insulators and Electronic Semiconductors," Phys. Rev., 54, 647 (1938).

[17] I. Fujieda, G. Cho, J. Drewery, T. Jing, S. N. Kaplan, V. Perez-Mendez, S. Qureshi, D. Wildermuth and R. A. Street, "Field Profile Tailoring in a-Si:H Radiation Detectors," MRS Symp. Proc., Vol. 192, p.399-404 (1990).

[18] J. S. Drewery, G. Cho, T. Jing, S. N. Kaplan, A. Mireshghi, V. Perez-Mendez and D. Wildermuth, "Improvement of Thick a-Si:H Radiation Detectors by Field Profile Shaping," MRS Symp. Proc., Vol. 258, p.1063-1068 (1992).

[19] R. A. Street, "Physics of a-Si:H p-i-n devices," J. Non-Crystalline Solids 164-166 p. 643-652 (1993).

[20] G. P. Weckler, "Operation of p-n Junction Photodetectors in a Photon Flux Integration Mode," IEEE J. Solid Circuits, Vol. SC-2, 65 (1967).

[21] S. A. Kleinfelder, W. C. Carithers, R. P. Ely, C. Haber, F. Kirsten, H. Spieler, IEEE Trans. Nuc. Sci. NS-35 (1988) 171.

[22] H. Mimura, K. Sai, Y. Ohta, K. Yamamoto, and K. Kitamura, "A Two-dimensional Image Sensor with a-Si:H PIN Diodes," Appl. Surf. Sci. Vol. 48-49 521-525 (1991).

[23] G. Cho, J.S. Drewery, W.S. Hong, T. Jing, H. Lee, S.N. Kaplan, A. Mireshghi, V. Perez-Mendez, and D. Wildermuth, "Utilization of a-Si:H Switching Diodes for Signal Readout from a-Si:H Pixel Detectors," MRS Symp. Proc., Vol.297, p. 969-974 (1993).

[24] K. Yamamoto, K. Sai, Y. Ohta, H. Mimura and K. Kitamura, "Amorphous Silicon 2-Dimensional Image Sensors," Techical Digest of the 8th Sensor Symp., p. 55 (1989).

[25] R. A. Street, S. Nelson, L. Antonuk and V. Perez-Mendez, "Amorphous Silicon Sensor Arrays for Radiating Imaging," Mat. Res. Soc. Symp. Proc., Vol. 192, 441 (1990).

[26] S. H. Morozumi, H. Ohshima, T. Takeshita, and K. Hasegawa,"Completely Integrated a-Si:H Linear Image Sensor with Poly Si TFT Drivers," Extended Abstarts 16th Conf. on Solid State Devices and Materials, Kobe, 1984, pp.559-562.

[27] A. G. Lewis, I-Wei Wu, T. Y. Huang, A. Chiang and R. H. Bruce, "Active Matrix Liquid Crystal Display Design Using Low and High Temperature Processed Polysilicon TFTs," IEDM-90, p. 843 (1990).

[28] W. den Boer, Y. Baron and Z. Yaniv, "Two-terminal Switches for Active-matrix LCDs," Information Display, 10/90. p. 4 (1990)

[29]   M. J. Thompson,"A Comparison of Amorphous and Polycrystalline TFTs for LC Displays," J. Non-Crystalline Solids 137-138 p. 1209-1214 (1991).

[30]   K. Shimizu, G. Sugiura, M. Matsumura,"On-chip Bottom-gate Polysilicon and Amorphous Silicon Thin-Film Transistors Using Excimer Laser Annealing," Jpn. J. Appl. Phys. Part 2-Lett. Vol. 29 N.10 p. 1775-1777 (1990).

[31]   Y. H. Jhon, D. H. Kim, H. Chu, S. S. Choi, "Crystalization of Amorphous Silicon by Excimer Laser Annealing with a Line Shape Beam Having a Gaussian Profile," Jpn. J. Appl. Phys. Part 2-Lett. Vol. 33 N.10B p. L1438-1441 (1994).

[32]   S. Seki, T. Unagami and B. Tsujiyama,"High Transconductance Si-TFTs Using Ta_2O_5 Film as Gate Insulator," 16th Conf. Solid State Devices and Materials., p. 563 (1984).

[33]   Y. Shiraki and E. Maruyama "Poly-Si TFTs and Their Applications to Liquid Crystal Display," Amorphous Semiconductor Technologies and Devices, Vol. 6, p. 266 (1983).

[34]   G. Brunst, H. Harms, J. Ashworth, K. Rosan, and K. Kempter, "a-Si:H TFTs and thier Application in Linear Image Sensors," J. Non-Crystalline Solids 97-98 p. 1343-1346 (1987).

[35]   R. L. Weisfield, "Amorphous-Silicon Linear-Array Device Technology: Applications in Electronic Copying," IEEE Trans. Electron Devices, Vol. 36, No.2, 1989, pp.2935-2939.

[36]   G. Cho, V. Perez-Mendez, M. Hack and A. Lewis, "Charge-Sensitive Poly-Silicon TFT Amplifiers for a-Si:H Pixel Particle Detectors," MRS Symp. Proc., Vol. 258 p.1181-1186 (1992).

[37]   K.Kempter, "Large-Area Electronics Based on Amorphous Silicon," Adv. Sol. Stat. Phys.,Vol. 27, 1987, pp. 279-305.

Chapter 3. Amorphous silicon photoconductor

Hydrogenated amorphous silicon detectors have been shown to be suitable for charged particles, neutrons, and X-rays [1-5], and their potential for minimum ionizing particle detection has been shown[6]. In general there are two main classes of photodetectors. Primary photocurrent devices (such as p-i-n solar cells) which have unity optical gain, very high light to dark sensitivity, and fast ($< 1\mu s$) response times. In contrast, secondary photocurrent structures, such as n-i-n diodes, exhibit high optical photoconductive gain determined by the ratio of the electron lifetime to transit time, low light to dark sensitivity, and slow response times (of the order of milliseconds)[7,8,9]. To make a better sensor one would like to combine the gain associated with secondary photocurrents with the low dark currents and fast response times of the solar cell structures.

3.1 Electronic Transport in a-Si:H

3.1.1 Conduction and photoconduction in a-Si:H

In the amorphous semiconductors the current is determined by charge carriers, electrons and holes, within the energy states distribution N(E)[10] shown in Fig.3.1. These carriers drift under a constant field at steady velocities depending on the field and the corresponding energy states[11].

For fields which are not very high, the drift velocity is proportional to the field E, and a constant mobility $\mu_{n,p}(E)$ can be introduced for carriers (electrons and holes) in the states around energy E and thus

$$v_{Dn,p} = \mu_{n,p}(E)E, \tag{3.1}$$

50

The total current due to all mobile carriers distributed among the energy states can be expressed as the integral

$$J_{n,p} = q \int n(E) v_D(E) \, dE, \qquad (3.2)$$

where n(E) is the density of carriers which will statistically occupy the state's DOS N(E)
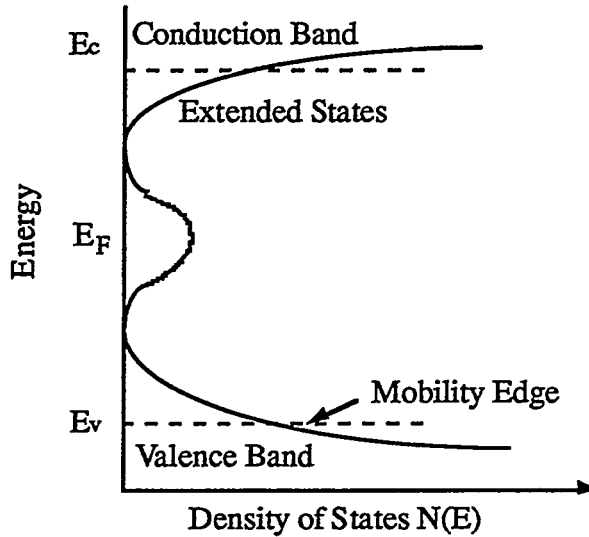
Fig.3.1 The energy band structure of a-Si:H.

around energy E and q is the charge of the electron

$$n(E) = N(E)f(E), \qquad (3.3)$$

the occupation probability being given by a Fermi-type function

$$f_n(E) = 1/[1 + \exp((E - E_F)/kT)] \qquad \text{for electrons} \quad (3.4)$$

$$f_p(E) = 1 - f_n(E) = 1/[1 + \exp((E_F - E)/kT)], \qquad \text{for holes} \quad (3.5)$$

E_F being the Fermi energy level. By using equations (3.1) and (3.3) in the current equation (3.2) one can write it as

$$J_{n,p} = q\varepsilon \int N_{c,v}(E) \mu_{n,p}(E) f_{n,p}(E) \, dE = \sigma_{n,p} E, \qquad (3.6)$$

and define a total conductivity $\sigma_{n,p}$ in terms of various states' contribution to it,

$$\sigma_{n,p} = \int q N_{c,v}(E) \mu_{n,p}(E) f_{n,p}(E) \, dE = \int \sigma_{n,p}(E) \, dE, \qquad (3.7)$$

51

In principle the integrals in the above equations should extend to all states that an electron can occupy, to the full energy range. But as the occupancy function, for both electrons and holes, is a fast decreasing function of energy, when energy departs from the Fermi level E_F, details of $N(E)$ and $\mu(E)$ are significant in conductivity only for energies within the gap which contains E_F and in the adjacent energy bands close to it.

For a-Si:H, mobility edges are defined within the density of states distribution. E_c is close to the conduction band and E_v is close to the valence band (Fig.3.1). There can be considered to be two main contributions to the total conductivity, band conductivity σ_b and localized states conductivity σ_l, both by electrons and holes[12]:

$$\sigma_b = q \int_{-\infty}^{E_v} Nv(E)\mu p(E) fp(E)\, dE + e \int_{E_c}^{+\infty} Nn(E)\mu n(E) fn(E)\, dE, \qquad (3.8)$$

$$\sigma_l = \int_{E_v}^{E_c} \sigma_{ln,p}(E)\, dE \qquad (3.9)$$

3.1.2 The conductivity of localized states

Within the mobility gap between E_v and E_c, the electronic states are localized around some centers randomly distributed through the material[13]. There is a finite probability of tunneling between states provided the energy difference between the tunneling sites is taken over through interaction with the atomic network in which these sites are imbedded. These interactions are temperature dependent emission or absorption of phonons, through inelastic interaction with phonons, the so called 'phonon induced delocalization'[12,14].

This conduction associated with site-to-site tunneling is usually referred to as hopping conduction. The contribution to hopping conduction from two localized states at distance R and ΔE in energy with electronic wave function decay constant α has been shown to be controlled by a hopping probability [15].

52

$$p = \nu \exp(-2\alpha R)\exp(-\Delta E/kT), \qquad\qquad (3.10)$$

where ν is an attempt frequency. The first exponential factor describes the tunneling probability, and the second one the probability of finding the necessary phonon to bridge the energy difference ΔE.

As indicated in equation (3.10), the contribution of localized states to conduction may become significant when temperature is excessively low, the discussion of photoconduction in later sections is based on the band conduction theory.

3.1.3 Photoconduction, non-equilibrium carriers and recombination

Thermal equilibrium carriers can only account for linear low-field electrical conduction in the dark. All other types of conduction must consider non-equilibrium effects: (i) carrier generation by irradiation and associated recombination; (ii) electrical injection of carriers; (iii) carrier 'heating' by high electric fields (energy distribution of carriers corresponding to a temperature higher than the ambient one).

When photons with greater-than-gap energies are absorbed into a semiconductor, electron-hole pairs are generated (an electron jumps from the valence into the conduction band, leaving behind a mobile hole). The presence of these generated photocarriers represents a non-equilibrium condition, and consequently the electrons and holes tend to lose the acquired energy, and finally annihilate each other, or recombine, within a time which depends on the properties of the electron states of the material.

If e-h pairs are continuously generated, a balance is finally reached between the generation and recombination rates, and a steady state is established. The various electronic energy states interact like thermally coupled subsystems which change particles between themselves. As a consequence, even if photocarriers are generated only in bands, even beyond their edges, they usually thermalize before recombining, i.e. they are distributed among all states. Thus, their occupancy function changes from an equilibrium (Fermi) one

53

to a non-equilibrium one. The latter not only depends on the departure from equilibrium and temperature, but also on the nature of the states.

The most important interactions in determining the occupancy function, are those between the localized energy states and bands, i.e. band carriers capture into traps and their re-emission is towards the same band, or the opposite one as illustrated in Fig.3.2[16,17].

The process which ensures a steady state under continuous carrier generation is the opposite process, carrier recombination, which is responsible for bridging the semiconductor back to equilibrium conditions, when illumination ceases. The recombination process in a-Si:H used for photoconductors, takes place usually only through the states which have capture coefficients for both bands and can ensure e-h annihilation. Such states are called recombination states, in contrast to trapping states, which have significant capture coefficients with only one band (with respect to re-emission coefficients toward the opposite band as shown in Fig.3.2. The two types of states behave differently in the steady state regime under illumination.
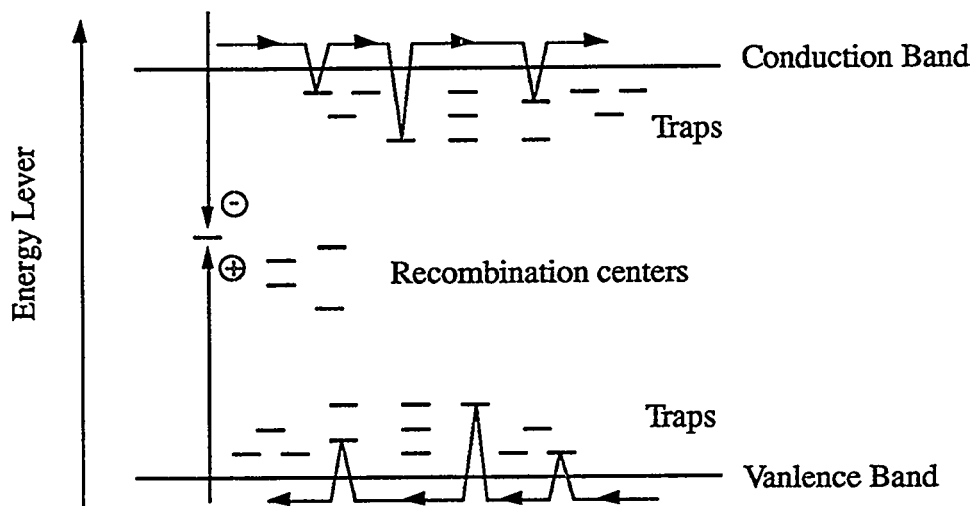

Fig.3.2 Illustration of trap-limited transport and carrier recombination process.

A pure trapping state exchanges carriers only with one band, and in the steady state the trapped carrier concentration is tied to the band carrier concentration, both varying with

the light level. A pure recombination state exchanges carriers with both bands, and in a steady illumination and recombination state it sends each carrier it receives from one band to the other one. To ensure that its carrier occupation may change from the equilibrium one, to balance different capture coefficients for the electrons (from the conduction band) and for the holes (from the valence one) an increase in electron population reduces the electron flow and increases the hole flow into it. When the electron flow balances the hole flow, the level of the electron population stabilizes and remains the same.

When the localized states extend as continuous tails from bands towards the gap, it has been shown [18] that one can assume that there are well-defined limits within the tails, which separate trapping levels near the bands from the recombination levels, beginning from shoulders near the bands, and extending deeper into the gap as shown in Fig.3.2.

The recombination efficiency of the levels around a certain energy E depends not only on capture coefficients, but also on the number of the levels and their occupation. Thus recombination maxima appear between the quasi-Fermi levels (or around the Fermi level for small illumination intensity ($\Delta n \ll n_0$; $\Delta p \ll p_0$). Within a density of states with shoulders, the levels around there tend to accumulate most of the non-equilibrium carriers and prevail in the recombination (except for very high injection levels when quasi-Fermi levels move into the bands beyond the shoulders).

As a consequence, even if there is a continuum of recombination levels one can identify quite a few recombination paths, among which one usually prevails, at certain illumination levels or temperatures.

3.2 Structure and Principles of Operation

Most of photoconductive sensor applications of thin-film amorphous silicon have the two main structures: coplanar and sandwich (Fig.3.3)[19-23].
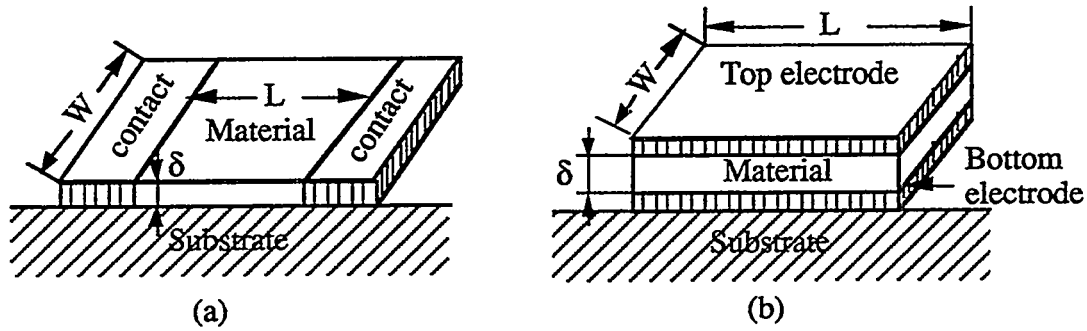
Fig.3.3 Photoconductor configuration: (a)coplanar structure; (b)sandwich structure.

3.2.1 Coplanar structures

Fig.3.3(a) shows the ideal coplanar structure and parameters. This structure is geometrically bidimensional (L, $W \gg \delta$) but its current flow in the dark is one-dimensional, normal to the electrodes (along dimension δ) over the transversal area $A = W\delta$. From an applications point of view it is better to characterize a photoconductor through its conductance, g. Thus for an ideal coplanar structure one has

$$g = A\sigma/L = W\delta\sigma/L. \tag{3.11}$$
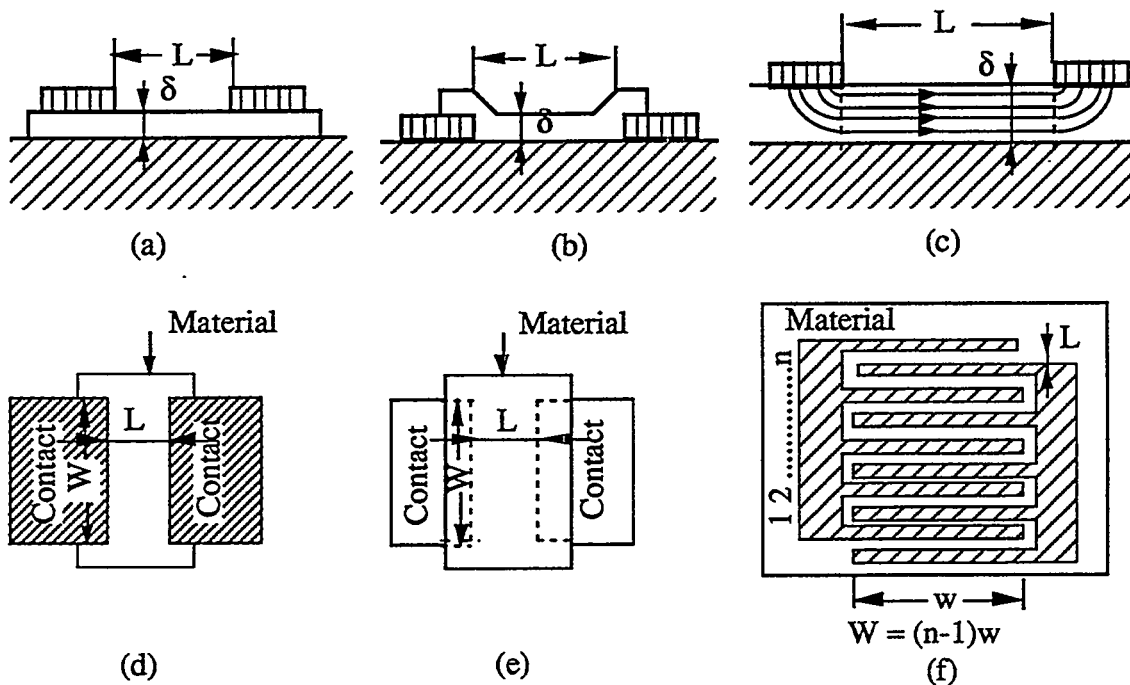
Fig.3.4 Real coplanar structures.

56

Fig.3.4 illustrates practical ways to realize coplanar structures and electrode configurations. The multigap structures, like the one in Fig.3.4(f) are well approximated by an ideal structure of the same total width, $W = (n - 1)w$, provided $L \ll w$.

The photoconductance of the coplanar structure increases above the dark conductance due to local increases in conductivity. The local photoconductivity depends on local photocarrier generation, i.e. the locally absorbed photon concentration $F(x)$.

As seen in Fig.3.4(f), the photocurrent flow is no longer one-dimensional, but two-dimensional along L and δ. An incident photo flux φ_0 decreases inside the material exponentially, at a depth x from the surface, the absorbed photon concentration is given by

$$F(x) = d\varphi(x)/dx = \alpha\varphi_0\exp(-\alpha x) = \alpha\varphi(x). \tag{3.12}$$

As the photon flux and the absorbed photon density decreases from the surface into the depth of the material, the local photoconductivity and current density decrease. For a given electric field $E = V/L$, inside the gap of thickness δ, the total current is

$$I = \int_0^\delta jwdx = wE\int_0^\delta [\sigma_d + \sigma_{ph}(x)]dx = w\delta\sigma E + e\eta\mu\tau wE\int_0^\delta F(x)dx,$$

$$= \frac{w\delta}{L}\{\sigma_d + e\eta\mu\tau\frac{\varphi_0}{\delta}[1 - \exp(-\alpha\delta)]\}V, \tag{3.13}$$

Here η is the percentage of carrier generation rate over the photon absorption rate. Thus the conductance $g(F)$ which can be expressed either as a sum

$$g(F) = g_d + g_{ph}(F) = g_d + \frac{e\eta\mu\tau w\varphi_0}{L}[1 - \exp(-\alpha\delta)], \tag{3.14}$$

or in terms of the $g(F)/g_d$ ratio

$$g(F)/g_d = 1 + \frac{\sigma_{ph}}{\sigma_d} = 1 + \frac{e\eta\mu\tau}{\sigma_d}\frac{\varphi_0}{\delta}[1 - \exp(-\alpha\delta)], \tag{3.15}$$

where σ_{ph} is the average photoconductivity of the semiconductor layer.

For applications in which photoconductive sensors are used as detectors of the level of illumination, the condition imposed is to obtain the highest possible $g_{ph}(F)$ under light and this responds to the condition $\alpha\delta \gg 1$. In such applications, high photocurrents are

important, the low resistance of the contacts to the amorphous semiconductor may become important.

For applications in which photoconductors are used for low illumination measurements, or when a proportional response is important, the highest possible ratio σ_{ph} /σ_d should be ensured. For a given α, the highest σ_{ph} and σ_{ph} /σ_d ratio is obtained for low thicknesses for which the photoconductivity is uniform throughout the semiconductor layer

$$(\sigma_{ph})_{\alpha\delta\ll1} \approx \sigma_{ph}{}^{max} = e\eta\mu\tau\alpha\varphi_0, \qquad (3.16)$$

As the thickness increases σ_{ph} decreases and for $\alpha\delta\gg1$, it becomes independent of α, i.e.

$$(\sigma_{ph})_{\alpha\delta\gg1} = e\eta\mu\tau\frac{\varphi_0}{\delta}, \qquad (3.17)$$

For a given δ the highest σ_{ph} is obtained for sufficiently high α for which $\alpha\delta\gg1$, and corresponds to eq.(3.17).

As already shown in section 2.1.2, the absorption coefficient α depends on the energy of the incident photons, increasing fast above E_g, the absorption edge of the semiconductor. For a given $\alpha\delta$, as $\alpha(hv)$ increases, σ_{ph} increases as $\alpha\delta(hv)$ as long as $\alpha\delta\ll1$ and then reaches a maximum at a value given by equation (3.17) when $\alpha\delta>1$. It further decreases due to diffusion and surface recombination effects, which have been neglected in our discussion.

3.2.2 Sandwich structures

Fig.3.5(b) shows the basic sandwich structure which consists in a semiconductor layer sandwiched between two electrodes which are supposed to ensure ohmic contacts to the semiconductor. To ensure ohmic contacts to the layers, in the case of a-Si:H devices, high photoconductive, high-resistive layers are slightly n-type, the sandwich and coplanar structures are practically realized by using highly doped n+ layers (p+ contact may be used

in some cases, as will be seen later) between the metallic contacts and the a-Si:H photoconductive layer, as shown in Fig.3.5.
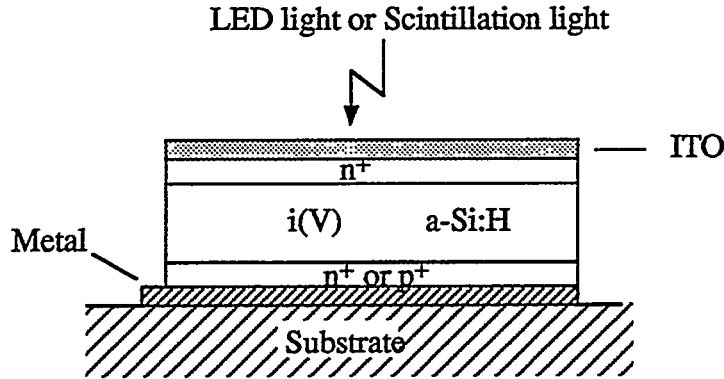
Fig.3.5 Schematic sandwich structure photoconductors which were tested and were also used to measured β particles described in Chapter 5.

Like coplanar structures, sandwich structures are also deposited on a substrate. The sandwich photoconductive structures have at least one electrode which is transparent to the light.

In contrast to coplanar structures, which are two-dimensional as regards both geometry and photocurrent flow, the sandwich structure is one dimensional, along distance δ. The dark conductance is

$$g_d = A\sigma_d/\delta = WL\sigma_d/\delta, \tag{3.18}$$

as the electric field in the structure is constant $E = V/L$.

We suppose, for the ohmic contacts case, that one type of carrier (for instance, electrons) prevails in the photocurrent throughout the sample. As the total current in the stationary state has a constant value ($J_n = J = $ constant), from the conservation law

$$G(x) - R(x) = \eta F(x) - \frac{\Delta n(x)}{\tau} = \frac{1}{e}\frac{dJ}{dx} = 0, \tag{3.19}$$

where $n(x)$ is the photocarrier concentration and the photoconductivity $\sigma_{ph}(x)$ is given by

$$\sigma_{ph}(x) = e\eta\mu\tau F(x), \tag{3.20}$$

59

Under light, due to the non-uniform illumination, the total conductivity varies along the current flow, thus the electric field is no longer constant, but is given by

$$E(x) = \frac{j}{\sigma_d + \sigma_{ph}(x)} = \frac{I/(WL)}{\sigma_d + \sigma_{ph}(x)}, \tag{3.21}$$

as the total voltage on the sandwich structure is given by

$$V = \int_0^\delta E(x)dx, \tag{3.22}$$

By expressing $\sigma_{ph}(x)$ in terms of $F(x)$ as in the case of the coplanar structures we finally obtain

$$g(F) = g_d\,\alpha\delta\,/\left[\ln(\frac{1+(\sigma_d/\overline{\sigma}_{phmax})\exp(\alpha\delta)}{1+\sigma_d/\overline{\sigma}_{phmax}})\right], \tag{3.23}$$

where $\overline{\sigma}_{phmax}$ is given by eq.(16), $g(F)$ is the total conductance. For $\sigma_d/\overline{\sigma}_{phmax}\gg 1$ one obtains

$$g(F) \approx g_d(1+\frac{\overline{\sigma}_{phmax}}{\sigma_d}\frac{1-\exp(-\alpha\delta)}{\alpha\delta}), \tag{3.24}$$

and for $(\sigma_d/\overline{\sigma}_{phmax})\exp(\alpha\delta) \ll 1$

$$g(F) \approx g_{ph}(F) = g_{phmax}(F)\frac{\alpha\delta\exp(-\alpha\delta)}{1-\exp(-\alpha\delta)}, \tag{3.25}$$

where

$$g_{phmax}(F) = WL\,\overline{\sigma}_{phmax}\,/\,\delta = g_d\,\overline{\sigma}_{phmax}\,/\,\sigma_d, \tag{3.26}$$

is the value of $g_{ph}(F)$ for $\alpha\delta\ll 1$ when the photoconductivity is uniform throughout the semiconductor material.

If we analyze eq.(3.23) in terms of spectral response due to $\alpha(h\nu)$, for low energy photons we obtain

$$g_{\alpha\delta\ll 1}(F) \approx g_d(1+\overline{\sigma}_{phmax}\,/\,\sigma_d) = g_d + g_{phmax}(F) = g_d + (WL/\delta)\eta\mu\tau\varphi_0\alpha(h\nu), \tag{3.27}$$

while for strongly absorbed photons the photoconduction becomes generally negligible

$$g_{\alpha\delta\gg 1}(F) \approx g_d, \tag{3.28}$$

except for the case where the condition for equation (3.25) is also fulfilled but this condition is very difficult to obtain for $\alpha\delta \gg 1$.

Let us deduce an expression for the photoelectric gain for a sandwich structure with geometric parameters δ, L, w, in which the dark conductivity can be neglected. The total generation rate is

$$I_G = e\eta WL \int_0^\delta F(x)\, dx, \tag{3.29}$$

and the variable electric field for $\sigma_d < \sigma_{ph}$ is

$$E(x) = \frac{j_{ph}}{\sigma_{ph}(x)}, \qquad\qquad \sigma_{ph}(x) = e\eta\mu\tau F(x), \tag{3.30}$$

and in such a field, the transit time can be written as

$$t_{tr} = \int_0^\delta \frac{1}{v(x)}dx = \int_0^\delta \frac{1}{\mu E(x)}dx = \frac{1}{\mu j_{ph}}\int_0^\delta \sigma_{ph}(x)dx, \tag{3.31}$$

an equation which can be rewritten

$$j_{ph} = \frac{1}{\mu t_{tr}}\int_0^\delta \sigma_{ph}(x)dx = \frac{e\eta\mu\tau}{\mu t_{tr}}\int_0^\delta F(x)dx = \frac{\tau}{t_{tr}}\frac{I_G}{WL} = \frac{I_{ph}}{WL}, \tag{3.32}$$

and the optical gain is given by

$$G_{ph}(V) = \frac{\tau}{t_{tr}(V)}, \tag{3.33}$$

The $t_{tr}(V)$ dependence can be obtained from equations (3.22) (3.29) and (3.30) as:

$$t_{tr}(V) = \frac{\delta^2}{\mu V}\frac{1}{(\alpha\delta)^2}[1 - \exp(-\alpha\delta)]^2\exp(\alpha\delta), \tag{3.34}$$

From equations (3.33) and (3.34), we can conclude that the optical gain is also absorption coefficient (or photon energy) dependent. Fig.3.6 shows the measurement of the optical gain from a 14 μm a-Si:H photoconductor for different light wave length with shaping time 5μs.
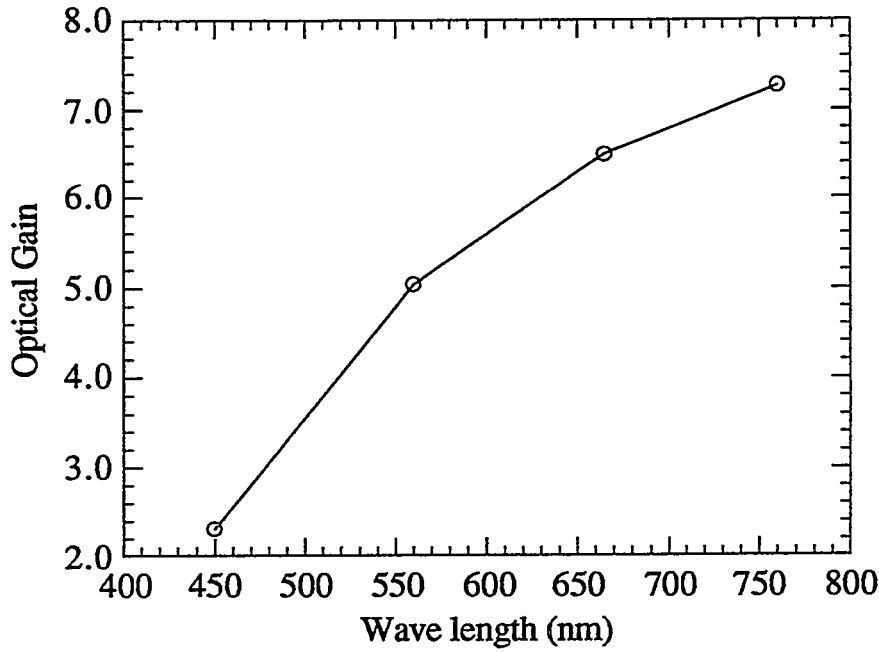
Fig.3.6 The dependence of optical gain on the incident light wavelength for a 14μm a-Si:H photoconductor.

when for quasi-uniform photoconductivity condition $\alpha\delta \ll 1$, reduces to,

$$t_{tr}(V) = \frac{\delta^2}{\mu V}, \quad E = \frac{V}{\delta}, \quad\quad\quad (3.35)$$

3.3 Characterization of Photoconductor

Primary photocurrent devices (such as a p-i-n diode under reverse bias) have unity optical gain and a fast response time (order of ns). In contrast, secondary photocurrent structures, such as n-i-n diodes or p-i-n diodes under forward bias, exhibit high optical photoconductive gain determined by the ratio of the electron lifetime to transit time[24].

3.3.1 . I-V characteristics

I-V characteristics were obtained for n-i-n and p-i-n devices. Fig.3.7 shows typical

62

current-voltage characteristics of a single photoconductive element consisting of 14 μm thick layer. The I-V measurements show that a p-i-n diode under forward bias has a much larger dark current than the n-i-n device under the same bias. This is because the n-i-n device blocks hole injection from both sides[25]. The relatively large current of the p-i-n due to electron and hole injection from the electrodes will degrade the light to dark sensitivity or signal to noise ratio due to the current shot noise. The shot noise can be reduced by using small area pixels, for a 100x100μm pixel with shaping time 1μs and gain of 4, the noise level is about 2300 electrons.
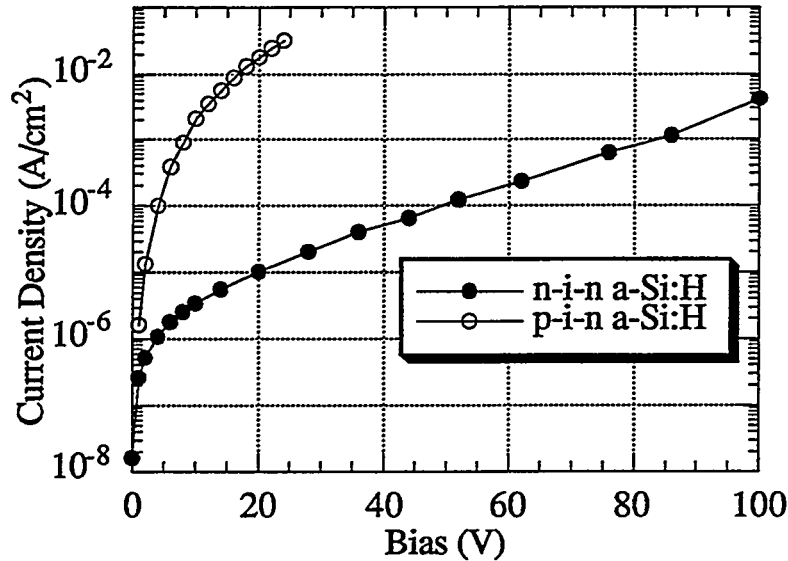

Fig.3.7 I-V characteristics of 14 μm thick n-i-n and p-i-n devices under forward bias.

Fig.3.8 shows optical gains obtained from a p-i-n 14 μm thick diode for different integrating times. The illumination source was a 665 nm LED emitting 200ns pulses.
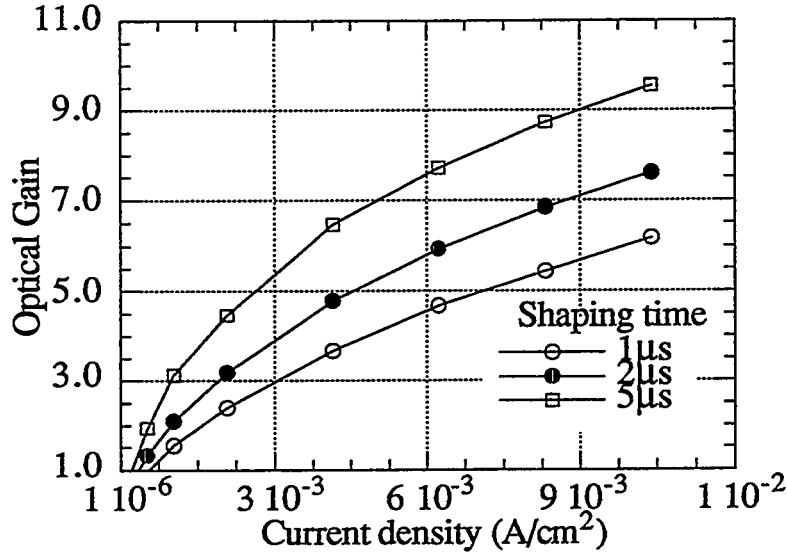
Fig.3.8 Gains obtained from a p-i-n device under forward bias with different shaping times.

3.3.2. Photoconductor transient parameters

The dynamics of time dependent photoconductivity may be described by combining the continuity equations for electrons and holes, the rate equation for trapping kinetics, the drift, diffusion current density equations and Poisson's equation to give[26]:

$$\frac{dn}{dt} = g(r,t) - R_n(r,t) + \frac{1}{q}\nabla \cdot J_n, \qquad (3.36)$$

$$\frac{dp}{dt} = g(r,t) - R_p(r,t) + \frac{1}{q}\nabla \cdot J_p, \qquad (3.37)$$

where g(r,t) is the electron hole pair generation. n(r,t) and p(r,t) are the electron and hole densities respectively, R_n(r,t) and R_p(r,t) are the electron and hole reduction rates, respectively, caused by trapping on deep level impurities, q is the electron charge, and J_n(r,t) and J_p(r,t) are the electron and hole current densities respectively. The model assumes spatially uniform excitation and single trap for each carrier, that is characterized by an average lifetime.

64

These equations can be rewritten in terms of excess densities. Assuming electron and hole densities (Δn and Δp) are large compared to their thermal equilibrium values, we obtain:

$$\frac{d\Delta n}{dt} = g(t) - B_n \Delta n (N_T - n_{To}^- + \Delta n - \Delta p), \tag{3.38}$$

$$\frac{d\Delta p}{dt} = g(t) - B_p \Delta p (n_{To}^- + \Delta p - \Delta n), \tag{3.39}$$

where $B_n = v_n \sigma_n$ and $B_p = v_p \sigma_p$ with v_n and v_p the electron and hole thermal velocities. σ_n and σ_p are electron and hole capture cross sections of trapping site and $N_T = n_T^o + n_T^- =$ total density of trapping. These nonlinearly coupled differential equations have to be solved depending on the duration of excitation, boundary conditions, initial conditions and fluence excitation.

An important nonlinear coupling is due to the electron and hole densities when they are just created by irradiation which greatly affected the electric field in drift terms. This works against the field needed for charge separation of the hole and electrons. As the range of values that the parameters can take under various conditions is large, we consider two kind of conditions: high intensity ($g > 10^{22} \text{cm}^{-3}\text{s}^{-1}$) and low intensity ($g < 10^{18} \text{ cm}^{-3}\text{s}^{-1}$). As main applications are imaging and metrology, we will consider only low intensities. For all cases the photoconductor is supposed to be uniformly illuminated and we distinguish three pulse duration domains.

We can define time constants for electrons and holes in equilibrium. At low intensity the equations are simplified as below:

$$\frac{d\Delta n}{dt} = g(t) - \frac{\Delta n(t)}{\tau_n}, \qquad \frac{d\Delta p}{dt} = g(t) - \frac{\Delta p(t)}{\tau_p}, \tag{3.40}$$

The analytical solutions are

$$\Delta n(t) = g(t)\tau_n \left(1 - e^{-\frac{t}{\tau_n}} \right), \qquad \Delta p(t) = g(t)\tau_p \left(1 - e^{-\frac{t}{\tau_p}} \right), \tag{3.41}$$

65

and we define time constants for electron and holes as:

$$\tau_n = \frac{1}{\sigma_n v_n (N_T - n_{To}^-)}, \qquad \tau_p = \frac{1}{\sigma_p v_p n_{To}^-}, \qquad (3.42)$$

The analytical expression of time dependent current generated by a photoconductor is:

$$I(t) = (\Delta n(t)\mu_n + \Delta p(t)\mu_p)q\frac{VA}{d} \qquad (3.43)$$

with A the electrode surface, d the photoconductor thickness between electrodes, and V the applied voltage. Now we can define the photocurrent gains as

$$G_I = \frac{I(t)}{I_0} = \frac{I(t)}{qg(0)Ad}, \qquad (3.44)$$

$$G_I = \frac{V}{g(0)d^2} g(t)\left[\mu_n \tau_n \left(1 - e^{-\frac{t}{\tau_n}}\right) + \mu_p \tau_p \left(1 - e^{-\frac{t}{\tau_p}}\right)\right], \qquad (3.45)$$

For a special case, when excitation light is a steady source or a long pulse, eq.3. can be simplified as steady state optical gain, i.e. $t \to \infty$, $g(t) = g(0)$, Thus

$$G_s = \frac{V}{d^2}\left(\mu_n \tau_n + \mu_p \tau_p\right), \qquad (3.46)$$

Combine with the facts $tr_n = \frac{d}{\mu_n E} \approx \frac{d}{\mu_n V/d} = \frac{d^2}{\mu_n V}$, and $tr_p = \frac{d^2}{\mu_p V}$, we have

$$G_s = \frac{\tau_n}{tr_n} + \frac{\tau_p}{tr_p}, \qquad (3.47)$$

This is a well-known simplified form of the optical gain. Since the transit time for holes is relative long, the second term of the eq.(3.47) is normally ignored. The optical gain is virtually dominated by electrons. For some applications, signals from a photoconductor is in term of the collected charge by integrating the photocurrent for a certain period. Thus the charge gain can be defined as the ratio of the collected charge to the primary hole-pair generated by photons.

$$G_c = \frac{\int_0^T I(t)dt}{q\int_0^{\Delta t} g(t)dt},$$

(3.48)

where T is the integration time, Δt the light pulse width. Fig.3.7 shows the charge gains for different shaping time by measuring signal response to a 200ns light pulse. Fig.3.10 shows the charge gain by integrating the photocurrent of Fig.3.9.
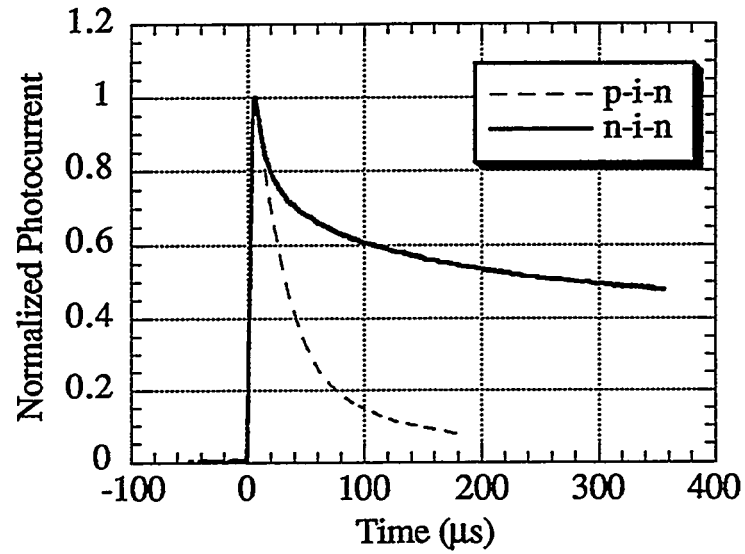

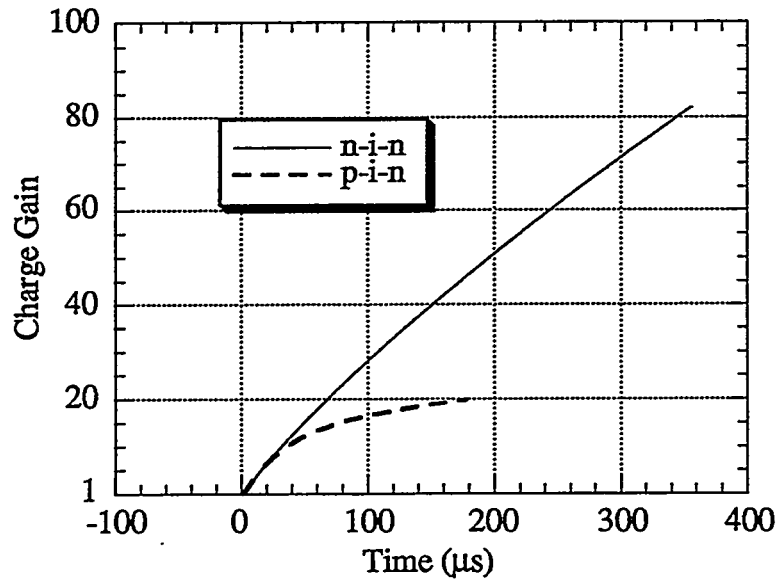Fig. 3.9 Photocurrent decay with time excited by a short light pulse.

Fig.3.10 The collected charge by integrating the photocurrent of Fig.3.9.

67

For a continuous distribution of traps in the forbidden gap, the photocurrent decay can be described by a power of time[27,28]. The time dependence of the photoconductive current is shown in Fig.3.9. When the duration of the excitation Δt_p is very short, the current waveform is mainly due to electrons.
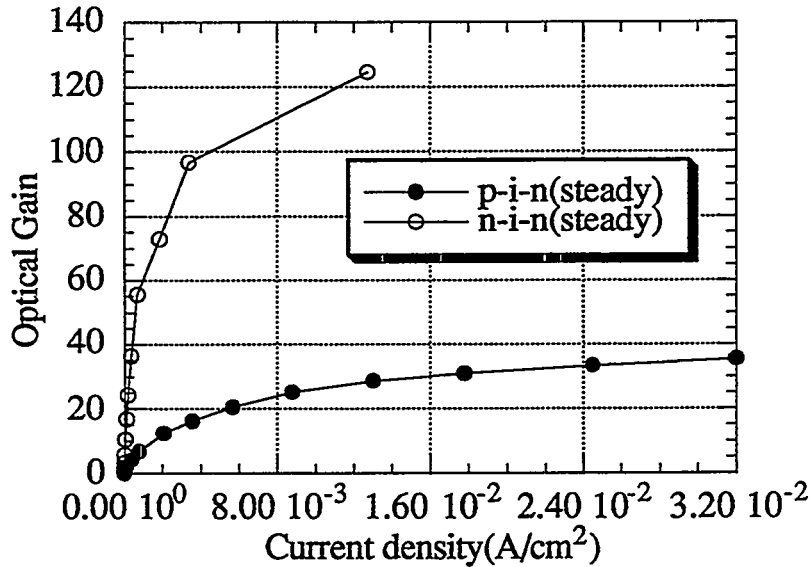
Fig.3.11 Long term optical gains of n-i-n and p-i-n devices.
The current was integrated for 10 ms.

The signal from an a-Si:H device operated as a photoconductor has long time decay components several ms long. By integrating the photoresponse for a long enough time, or measuring a DC response, the photoconductive gain for the steady state can be obtained. For medical imaging where X-ray radiation exposures are typically 10 milliseconds or longer, there is a difference between the integrated pulses from p-i-n and n-i-n devices. An n-i-n device exhibits a larger gain than a p-i-n one because hole injection through a p-i junction increases the recombination rate with the secondary electrons, and therefore reduces the optical gain. Fig.3.9 shows the responses of p-i-n and n-i-n devices to short light pulse ~200ns. The amplitudes of the photocurrents of these two structures are very close for the first 10μs, which result in the same optical gain for a short integrating time.

However, the photocurrent of the p-i-n device decays faster than the n-i-n device after 10 μs. In the other words, secondary current of the n-i-n device lasts a longer time, hence its optical gain for a long-time integral is much higher than the p-i-n one, as seen in Fig.3.9.

Fig.3.11 shows the long term gains of the p-i-n and n-i-n devices, based on integration of current over 10ms. The gain of the n-i-n diode is substantially higher than the p-i-n one because the p-i-n has hole injection through the p layer which decreases the optical current by recombining with the electrons.
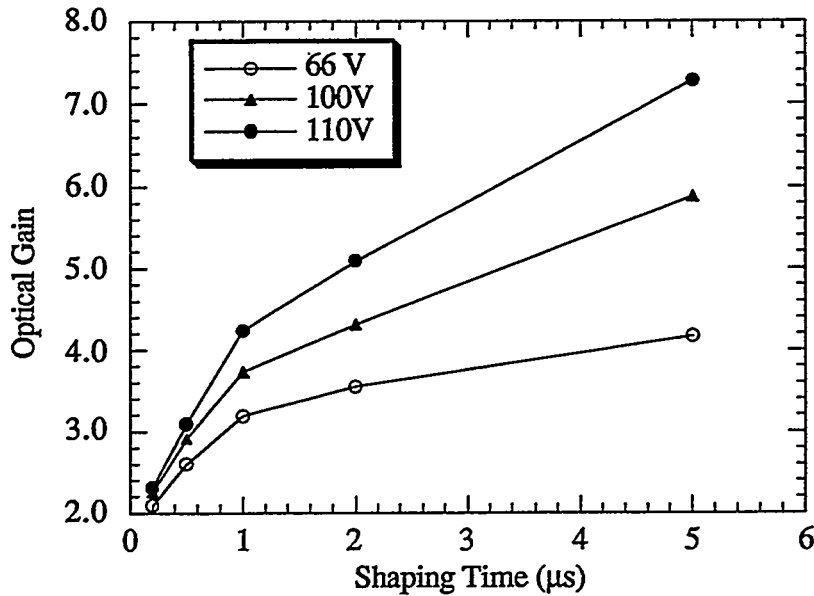
Fig.3.12 The optical gains of a 14 μm thick n-i-n diode for different shaping times.

As noted in Fig.3.9, photocurrents decay very fast in the first 10 μs, it was therefore expected that optical gain larger than unity could be obtained by integrating photocurrent with a short period, say less than 10 μs. Fig. 3.12 shows that such a gain was obtained from a 14μm thick n-i-n diode under different biases for a shaping time from 0.2- 5 μs.

As discussed above, the photocurrent of a p-i-n diode under forward bias has the same decay characteristics in the first 10μs as the n-i-n diode. Thus their optical gains for

short-time measurements exhibit the same values. Fig.3.13 shows optical signal from a 2μm-thick p-i-n diode under reverse and under forward bias. The excitation source is a 665nm LED with a 300ns pulse. Under a reverse bias of 10V, the signal tends to saturate at 1.6V, which is regarded as unity gain. With the same setup, upon changing the bias polarity, the signal rises rapidly with bias and reaches a maximum at 10V, then drops down with further increase of the bias. Clearly, this diode shows a gain of 6 in the photoconducting mode. The reason for reduction of gain under higher forward bias is due to the fact that much more hole injection through the p layer easily recombines with the electrons. This effect cancels any further gain due to higher bias. This effect is also considered to be a space-charge limited effect[29,30].
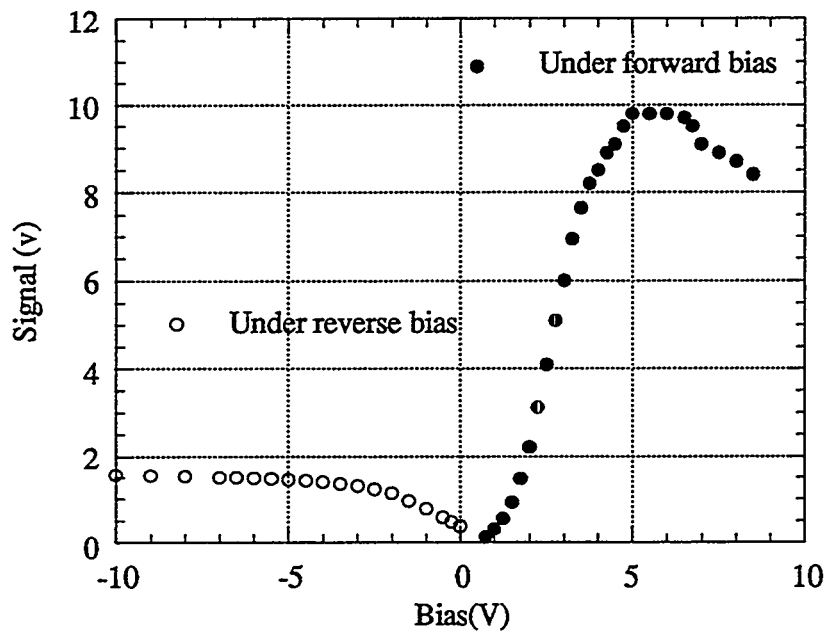

Fig.3.13 The signal from a 2 μm thick p-i-n diode as a function of detector bias with shaping time of 5 μs. The saturation range under reverse bias can be regarded as unity gain. Thus the optical gain under forward bias reaches 6 at 5 voltage.

3.3.3. Linearity of the a-Si:H photoconductors

It is a common observation to find in many semiconductors, photocurrents increase nearly linearly with light intensities over a wide range of light intensities. The dependence of photocurrent I_{ph} upon the light intensity ϕ_{ph} is defined as:

$$\gamma = d(\ln I_{ph})/d(\ln \phi_{ph}), \qquad \text{or} \qquad I = a\, \phi_{ph}{}^{\gamma} \qquad (3.49)$$

where a is a proportionality constant. As in many amorphous semiconductors, it is found experimentally that, in a-Si:H, γ is constant and with $0.5 < \gamma < 1$[22,31,32]. However, the exponent γ is known to depend in a sensitive and complex manner upon temperature and photon energy[33] and upon photo-induced effects[34]. In addition, γ values larger than unity can be found in the thermal quenching range[35] whereas in the field-effect transistor structure it has been shown that γ strongly depends upon the gate potential and reaches values as low as 0.15 for positive voltages[36,37]. In this study, we examine the linearity of the a-Si:H photoconductor within the range of 10^{11}-10^{15} photons/cm^2.
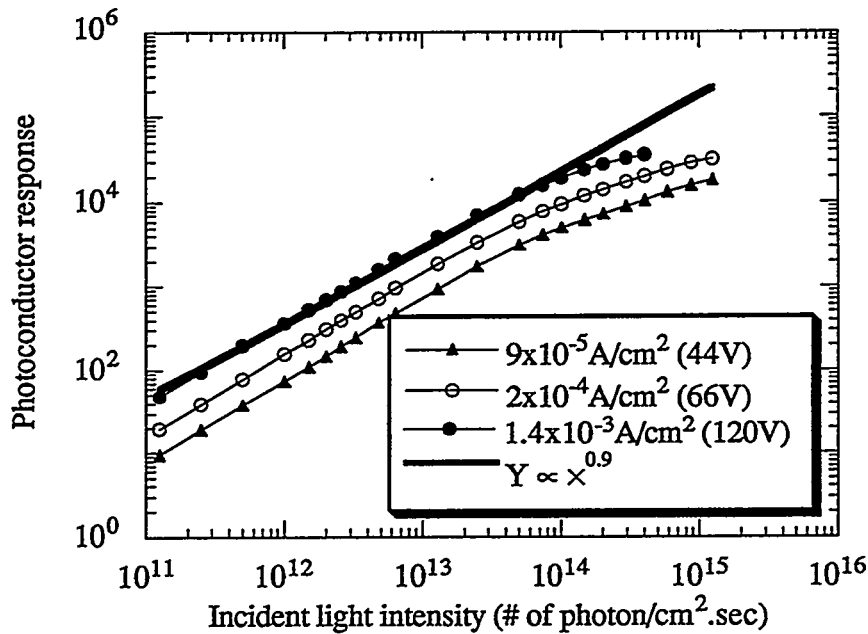
Fig.3.14 response of the photoconductor to incident light intensity.

Fig.3.14 shows data for the photon response of the photoconductor as a function of high incident light intensity to simulate medical X-ray exposures. It is seen that the response increases as the 0.9 power of the incident light flux. Such a sublinearity is acceptable in many application including in medical imaging.

For the incident light intensity below 10^{12} photons/cm^2, the exponent γ is close to unity although it is not shown in Fig.3.14.

References

[1] W. Guang-Pu, H. Okamoto and Y. Hamakawa, "Amorphous-Silicon Photovoltaic X-Ray Sensor," Jpn. J. Appl. Phys., 24, 1105 (1985)

[2] A. Mireshghi, G. Cho, J. S. Drewery, W. S. Hong, T. Jing, H. K. Lee, S. N. Kaplan and V. Perez-Mendez, "High Efficiency Neutron Sensitive Amorphous Silicon Pixel Detectors," IEEE Trans. Nucl. Sci., 41, 915 (1994)

[3] V. Perez-Mendez, "Charged Particle, Gamma Ray, and Light Detection in Amorphous Silicon Devices," Chapter 8 in *Amorphous & Microcrystalline Semiconductor Devices*, edited by J. Kanicki, Artech House, Boston (1991)

[4] I. Fujieda, G. Cho, J. Drewerey, T. Gee, T. Jing, S. N. Kaplan, V. Perez-Mendez and D. Wildermuth, "X-Ray and Charged Particle Detection with CsI(Tl) Layer Coupled to a-Si:H Photodiode Layers," IEEE Trans. Nuc. Sci., NS-38, 255 (1991).

[5] H. K. Lee, J. S. Drewery, W. S. Hong, T. Jing, S. N. Kaplan, A. Mireshghi and V. Perez-Mendez, "Hydrogenated Amorphous Silicon (a-Si:H) Based Gamma Camera - Monte Carlo Simulations," SPIE Vol. 2163, Medical Imaging 1994: Physics of Medical Imaging, 427 (1994)

[6] S. N. Kaplan, I. Fujieda, V. Perez-Mendez, S. Qureshi, W. Ward and R. A. Street, "Detection of Minimum-Ionizing Particles in Hydrogenated Amorphous Silicon," Nuc. Instr. and Meth., A273, p.611-614 (1988).

[7] M. Hack, M. Shur and C. C. Tsai, "Amorphous Silicon Photoconductive Diode," Appl. Phys. Lett., 54, 96 (1989)

[8] R. S. Crandall, "Photoconductivity," Chapter 8 in *Semiconductors and Semimetals*, Vol. 21, Part B, edited by J. I. Pankove, Academic Press, Inc., Orlando (1984)

[9] T. Saito, K. Suzuki, T. Nakai, Y. Suda, S. Takayama, K. Mori, O. Shimada, K. Sasaoka, T. Sakano, Y. Fukumoto and K. Ambo, "Amorphous Silicon Photoconductive Contact Image Sensor," Extended Abstracts of the 18th Conference on Solid State Devices and Materials, Tokyo, 703 (1986)

[10] K. D. Mackenzie, P. G. LeComber and W. E. Spear, "The Density of States in Amorphous Silicon Determined by Space-Charge-Limited Current Measurements," Philos. Mag. B., 46, 377 (1982)

[11] R. Williams and R. S. Crandall, "Carrier Generation, Recombination, and Transport in Amorphous Silicon Solar Cells," RCA Rev., 40, 371 (1979)

[12] H. Overhof and P. Thomas,"Electronic Transport in Hydrogenated Amorphous Semiconductors," Vol 114, Springer, p 69 (1989).

[13] G. G. Roberts and F. W. Schmidlin, "Study of Localized Levels in Semi-Insulators by Combined Measurements of Thermally Activated Ohmic and Space-Charge-Limited Conduction," Phys. Rev., 180, 785 (1969)

[14] M. Kikuchi, "Phonon-induced Delocation of Band Tail States in Amorphous Semiconductors," J. Non-Cryst. Solids 59 &60, 25 (1983).

[15] N. F. Mott and E. A. Davis, *Electronic Processes in Non-Crystalline Materials*, Clarendon, p. 40 (1971).

[16] R. J. Fleming, "Trap-Controlled Transient Photoconductivity in Dielectrics," J. Appl. Phys. 50, 8075 (1979)

[17] J. -H. Zhou and S. R. Elliott, "Deep Trapping and Recombination in Hydrogenated Amorphous Silicon," Philos. Mag. B, 69, 147 (1994)

[18] T. C. Arnoldusen, R. H. Bube, E. A. Fagen and S. Holmberg, "Analysis of Photoconductivity in Amorphous Chalcogenides," J. Appl. Phys. Vol. 43, p. 1798 (1972).

[19] T. Hamano, H. Ito, T. Nakamura, T. Ozawa, M. Fuse and M. Takenouchi, "An Amorphous Si High Speed Linear Image Sensor," Jpn. J. Appl. Phys., 21, 245 (1982)

[20] T. Kagawa, N. Matsumoto and K. Kumabe, "Amorphous Silicon Photoconductive Sensor," Jpn. J. Appl. Phys., 21, 251 (1982)

[21] K. Rosan, "Amorphous Semiconductor Image Sensors: Physics, Properties, and Performance," Chapter 7 in *Amorphous & Microcrystalline Semiconductor Devices*, edited by J. Kanicki, Artech House, Boston (1991)

[22] R. G. Stearns and R. L. Weisfield, "Two-Dimensional Amorphous-Silicon Photoconductor Array for Optical Imaging," Appl. Optics, 31, 6874 (1992)

[23] H. K. Lee, J. S. Drewery, W. S. Hong, T. Jing, S. N. Kaplan and V. Perez-Mendez, "Utilization of Photoconductive Gain in a-Si:H Devices for Radiation Detection," To be presented at MRS Meeting in April at San Francisco (1995)

[24] J. I. Pankove, *Semiconductors and Semimetals*, Vol. 21, Part B, Academic Press, Inc.   1984 p.264.

[25] M. Hack and W. den Boer, "A Comparison of Single- and Double-Carrier Injection in Amorphous Silicon Alloys," J. Appl. Phys., 58, 1554 (1985)

[26] A. E. Iverson and D. L. Smith, "Mathematical Modeling of Photoconductor Transient Response," IEEE Trans. Electron Devices ED-34 (10) p.2098 (1987).

[27] F. W. Schmidlin, "Theory of Trap-Controlled Transient Photo-conduction," Phys. Rev. B, 16, 2362 (1977).

[28] R. Pandya and E. A. Schiff, "A Multiple-Trapping Model with Optical Bias," Philos. Mag. B, 52, 1075 (1985).

[29]   A. Rose, *Concepts in Photoconductivity and Allied Problems*, Interscience Publishers, New York (1963).

[30]   A. Rose, "Space-Charge-Limited Currents in Solids," Phys. Rev., Vol.97, p. 1538 (1955).

[31]   R. H. Bube, *Photoconductivity of Solids*, John Wiley & Sons, Inc., New York (1960).

[32]   W. E. Spear, R. J. Loveland, and A. Al-Sharbaty, "The Temperature Dependence of Photoconductivity in a-Si," J. Non-crystalline Solids, Vol. 15, p. 410 (1974).

[33]   D. L. Staebler and C. R. Wronski,"Optical Induced Conductivity Changes in Discharge-produced Hydrogenated Amorphous Silicon," J. Appl. Phys. Vol. 51, p. 3262 (1980).

[34]   M. Hoheisel, R. Carius, and W. Fuhs, "Low Temperature Photoconductivity in a-Si:H Films,"J. Non-crystalline Solids, 59-60, p457 (1983).

[35]   W. B. Jackson, M. J. Thompson, Physica B, 117-118, p 883 (1983).

[36]   C. Van Berkel and M. J. Powell, "The Photoconductivity of Amorphous Silicon Thin Film Transistors," J. Non-crystalline Solids, 77-78, p. 1393 (1985).

[37]   R. Vanderhaghen, R. Amokrane, D. Han and M. Silver, "Effect of Light-Induced Degradation on Photoconductive Gain in a-Si:H n-i-p devices," J. Non-Cryst. Solids, 164-166, 599 (1993)

Chapter 4. High Spatial Resolution Scintillator

4.1 Introduction

One of the essential components of a radiation imaging chain is a radiation input converter. In most applications of position-sensitive radiation detection, conventional radiography[1-3], and digital radiography[4-6], a scintillator screen is used to convert the incoming radiation into visible light which is then detected on film or other position sensing device. Such scintillators are usually required to have high spatial resolution and high output brightness characteristics. The brightness of the light output is, in part, a function of the thickness of the scintillation layer, which determines the amount of x-ray energy absorbed, and of the inherent scintillation efficiency. As this layer is made thicker, the spatial resolution is decreased because light photons emitted in response to the absorption of x-ray photons or charged particles will emerge from the scintillator surface at points further away in the transverse direction, as shown in Fig.4.1. Such lateral light spreading is caused by two factors: first, the scintillator emits light photons isotropically from the point at which the radiation particle, x-ray photon or charged particle, is absorbed; second, even light photons which are traveling more or less perpendicularly to the surface may be scattered in the lateral direction before they reach the surface. Thus, the actual thickness of the scintillation layer is a compromise between the desired high radiation absorption that may be obtained from thicker layers and the required or desired resolution which improves as the thickness of the layer is reduced. Obviously, it would be desirable to increase the thickness of the scintillation layer without degrading the spatial resolution. This can be accomplished by suppressing the lateral light spread within the layer. Certain techniques for forming small cracks perpendicular to the scintillator surface to limit light spread have been developed[7-9], and the characteristics of evaporated CsI(Tl) layers coupled to a-Si:H photodiodes have been reported[2].

76

X-ray photon

CsI
film
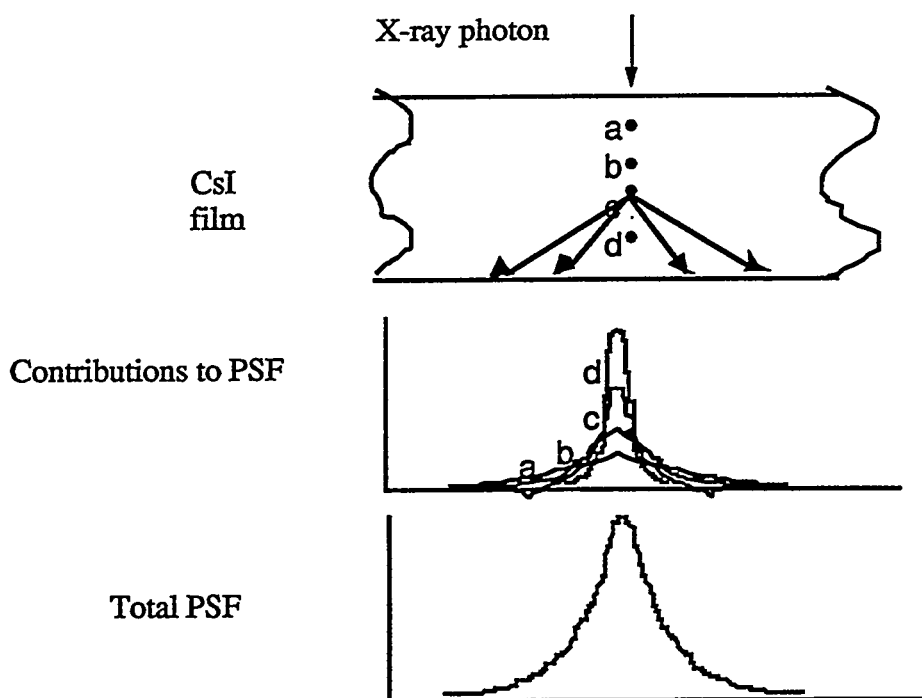
Contributions to PSF

Total PSF

Fig.4.1 How the point spread function of a scintillator screen is determined
by integrating contributions from individual layers (a), (b), (c), (d).

One early approach to form a light-guide structure in a luminescent layer was to deposit a thin scintillation layer of CsI on the substrate[7] and impart thermal shocks to the CsI layer, producing cracks therein due to the different thermal expansion coefficients of the substrate and the CsI layer. Another light-guide structure fabrication method was made [9], in which the substrate had a very thin AlO_3 layer on the top; when baked it cracked the AlO_3 layer, forming small grooves on the substrate. This type of cracked or net-like mosaic substrate further enhances the columnar structure of the scintillation material deposited on it. However, a scintillation layer prepared by these processes has the following drawbacks:1), the columns defined by cracks have an irregular structure, which decreases the light collimation and thus decreases the resolution. 2), it is difficult to ensure the reproducibility of the size of the columns. For these reasons, CsI x-ray scintillation layers (150-200µm thick) made by these methods have spatial resolution measured as a modulation transfer function (MTF) of 4 to 6 line-pair/mm at the 10 percent level.

77

Thin films manufactured by one of the various physical vapor deposition (PVD) methods have a microstructure, which in general differs from the structure of bulk material of the same mean composition. This microstructure depends on the conditions during the film formation and is governed by the kinetics of the process. Understanding the morphology formation will help us to understand in more detail the origin of the physical properties of thin films. Since the morphological properties of thin films are not explicitly dependent on their composition, they can be systematized in terms of a small number of reduced deposition parameters.

In this chapter, starting from the well-known idea of atomic shadowing during growth (i.e. ballistic aggregation) a model is employed which includes sufrace relaxation by thermally induced sufrace diffusion, desorption, angular distribution of the oncoming atoms, and atomic attraction. This enables us to consider such deposition parameters as substrate temperature, energy of oncoming particles, deposition geometry, and inert gas pressure. The model is applied to investigate the influence of various deposition parameters on the morphology of thin film of CsI. We then describe a new approach for the fabrication of a scintillation layer by forming a sequence of columns of regular, controlled size (diameter) perpendicular to the substrate (or detector), which provides a high light collimation property, thereby improving the resolution of the radiation detection. The performances of CsI films are described in the last section. The optical properties of evaporated CsI(TI) layers, such as light yield, transmission and light emission decay are discussed below.

4.2 Mechanism of Scintillation

4.2.1 The energy band model

In a scintillator crystal, variations due to lattice defects and impurities occur in the energy bands, producing local electronic energy levels in the normally forbidden region

78

between the conduction and valence bands. If these levels are unoccupied, electrons (or excitons) moving in the conduction band in their vicinity may enter these centres. The centers are of three main types:

1. Luminescence centers, in which the transition to the ground state is accompanied by photon emission.

2. Quenching centres, in which radiationless thermal dissipation of excitation energy may occur.

3. Traps, which have metastable levels from which the electrons (or excitons) may subsequently return to the conduction band by acquiring thermal energy from the lattice vibrations, or fall to the valence band by a radiationless transition.

The same center may contain luminescence, quenching and trapping levels, their relative population being determined by the Boltzmann statistical distribution.
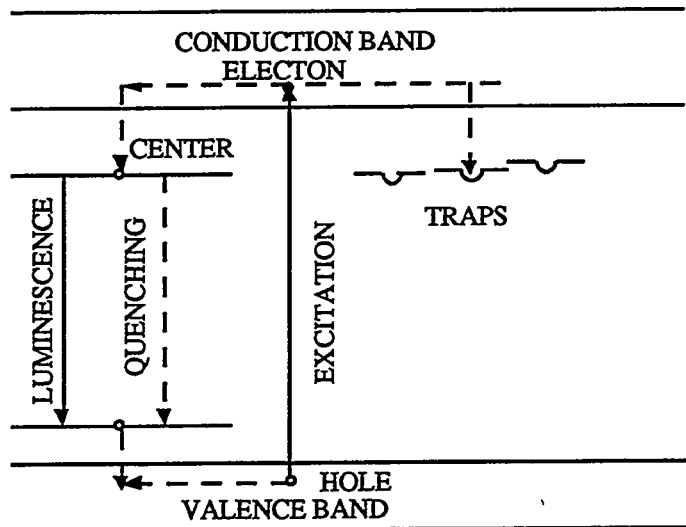

Fig. 4.2 Energy bands in impurity-activated crystal phosphor, showing excitation, luminescence, quenching and trapping processes.

The luminescence and quenching centers arise from impurities; interstitial ions and or defects, and they introduce local discrete energy levels corresponding to the ground and excited states of the center. The centers usually include not only the impurity ions etc., but also the neighbouring lattice ions. One important point, often overlooked in the early

literature, is that the excitation of a centre requires the capture of an electron from the conduction band and the capture of a hole from the valence band, either simultaneously by the capture of an exciton, or by electron-hole recombination at a center.

Traps arise from other lattice disturbances and provide additional levels for electrons below the conduction band. Similarly, hole traps may arise, which provide additional levels for holes above the valence band. In crystal CsI(Tl), the electron traps are lattice points from which negative ions are missing (cation vacancies), and the F-centres are formed when the defects capture electrons from the conduction band. The energy level system for an impurity-activated crystal phosphor is shown schematically in Fig. 4.2.

4.2.2 Conditions for luminescence of a center

The potential energies of the ground and excited electronic states of the luminescence center are plotted against some configurational coordinate (x) of the center as shown in Fig.4.3. The curves aAa' and bBb' represent the vibrational amplitudes of the
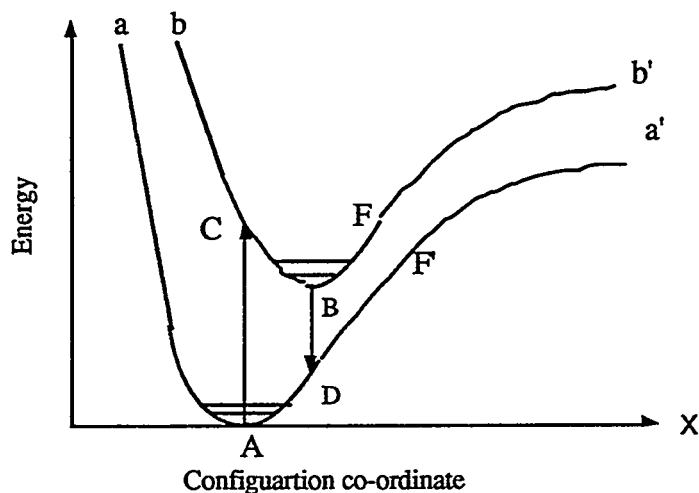

Fig.4.3 Potential energy diagram of luminescence center. aAa', ground state. bBb', excited state. AC, absorption transition. BD, luminescence emission transition. FF', he region of internal quenching.

center in the ground and excited electronic states respectively. The minima A and B correspond to the stable energy positions in the two states. At normal temperatures the thermal vibrations cause displacements from the minimum potential energy positions corresponding to energies of the order of kT.

The direct absorption of a photon hv by the center (or its excitation by capture of an exciton) causes a transition from the ground to the excited state of the system. Such a transition occurs along a vertical line AC on the diagram, since electronic transitions involved in absorption or emission occur in a time short compared with that of atomic or ionic movements[10]. Immediately after this transition the system is not in a state of minimum potential energy, and so it moves from C to B, the excess vibrational energy being dissipated thermally to its neighbours. The time spent in the region of B depends on the probability of the optical transition BD which gives rise to the luminescence emission hv. After this transition occurs the center, now in its electronic ground state, returns from D to A with further thermal dissipation of excess vibrational energy.

4.2.3 Scintillation in CsI

When ionizing radiation is absorbed in CsI doped with small amounts of Tl, CsI(Tl), scintillation light is produced and the emission spectrum of the light is similar to the thallium ion fluorescence excited by non-ionizing radiation at wavelenths where there is no optical absorption for CsI. Since the maximum luminescence efficiency occurs at low concentrations of Tl (0.05 to 0.4 mole percent) and the energy efficiency is high 12%, it is inferred that the ionizing radiation is absorbed by the CsI host lattice and deposited energy subsequently transferred by some mechanism to the thallium traps giving thallium luminescence.

The Tl impurity enters CsI as a substitutional monovalent ion on a cation site, Tl^+. Hole capture at a thallium site produces the Tl^{++} ions. Subsequent recombination of an

electron with the Tl^{++} [11,12] leads to an excited states $(Tl^+)^*$ which returns to the ground state with the emission of a scintillation photon.

One important consequence of luminescence through activator sites is the fact that the crystal can be transparent to the scintillation light. In the pure crystal, roughly the same energy is required to excite an electron-hole pair as that liberated when that pair recombines. As a result the emission and absorption spectra will overlap and there will be substantial self-absorption. However, the emission from an activated crystal occurs at an activitor site where the energy transition is less than that represented by the creation of the electron-hole pair. As a result the emission spectrum is shifted to longer wavelength and will not be influenced by the optical absorption band of the scintillator.

4.3 Principles of the Growth

The advantages of vapor-deposition technology should be obvious after considering the details of the process. It is possible to volatilize selectively a feed material, transport it to a desired location, and precipitate it as a controlled structure. Thus we employed the Physical Vapor Deposition (PVD) technology to deposit CsI(Tl) layer because it provides a high deposition rate and also produces desirable columnar structure when certain parameters are controlled well[13]. The deposition of thin films by vacuum evaporation consists of several distinguishable steps:

1. Transition of a condensed phase, which may be soild or liquid, into the gas state.

2. Vapor traversing the space between the source and the substrate at reduced pressure.

3.Condensation of the vapor upon arrival on the substrate.

Accordingly, the theory of vacuum evaporation includes the thermodynamics of phase transitions from which the equilibrium vapor pressure of materials can be derived, as well as the kinetic theory of gases which providees models of the atomistic processes. Vapor deposition may be defined as the condensation of elements or compounds from the vapor

state to form solid deposits. Thermodynamically, the only requirement for condensation to occur is that the partial pressure of the film material in gas phase be equal to or larger than its vapor pressure in the condensed phase at that pressure[14]. However, this is true only if condensation takes place on film material already condensed or on a substrate made of the same material. In practice, the substrate has a chemical nature different from that of the film material. Under these conditions still a third phase must be considered, namely, the adsorbed phase, in which vapor atoms are adsorbed on the substrate but have not yet combined with other adsorbed atoms. Condensation is initiated by the formation of small clusters through combination of several adsorbed atoms. These clusters are called nuclei, and the process of cluster formation is called nucleation. In the next section, the pricinpal of condensation will be reviewed, and then we will apply this theory in the CsI deposition processes.

4.3.1 Nucleation and growth on preferred sites

Nucleation is an initial stage of any phase transformation, including crystallization. Two principal cases of nucleation are usually considered: (1) homogeneous (i.e., spontaneous formation of nuclei in the bulk of supersaturated or supercooled systems) and (2) heterogeneous (i.e., formation of nuclei on interfaces such as solid substrates, foreign particles, and vessel walls).

(a) Homogeneous Nucleation

Gibbs[15] first analyzed nucleation of droplets from supersaturated vapors. He calculated the free-energy change ΔG of the system (the so-called "Gibbs work of nucleation") in the form

$$\Delta G = - 4\pi r^3 \Delta\mu / 3\Omega + 4\alpha\pi r^2, \qquad (4.1)$$

where r is the radius of the droplet, $\Delta\mu = \mu_v - \mu_c$ is the change in chemical potentials μ of the initial (vapor) and final (condensed) phase transformation, Ω is the atomic (or

molecular) volume, α is the specific free energy of the surface formed. For $\Delta\mu{>}0$ (the case that has practical sense only for homogeneous nucleation), the dependence is shown schematically in Fig.4.4(a) for two different values of $\Delta\mu$, $\Delta\mu_2$ being larger than $\Delta\mu_1$. From the condition $\partial(\Delta G)/\partial r = 0$, it is found that the maximum of ΔG is achieved at the critical value

$$r_c = 2\Omega\alpha/\Delta\mu, \tag{4.2}$$

where $\Delta\mu = kT\ln(p/p_0)$, p_0 is the equilibrium vapor pressure, p is the real pressure, we obtain from equation (4.2) the well-known Gibbs-Thomson equation:

$$p = p_0 \exp(2\Omega\alpha/kTr_c), \tag{4.3}$$

This equation [more often in the form of equation (4.2)] is the principal one in all nucleation theories, because it determines the so-called "critical radius" of the nucleus.

For not too high supercooling, $\Delta\mu$ can be written as:

$$\Delta\mu \approx \Delta H \Delta T/T_0 \tag{4.4}$$

where T_0 is the melting point of a given material, $\Delta T = T_0 - T$ is the supercooling, ΔH is the enthalpy of melting.

The value $\Delta G_c = (16\pi/3)\Omega\alpha^3/(\Delta\mu)^2$ corresponding to the critical radius r_c is the potential barrier that must be overcome by the system for such a transformation to proceed. The larger the $\Delta\mu$, the smaller is the barrier (cf. curves I and 2 in Fig. 4.4(a)).
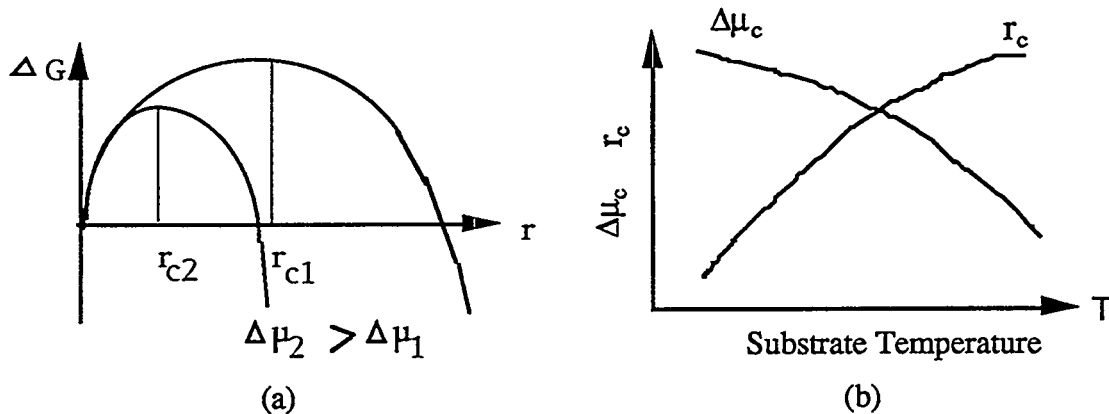

Fig.4.4 (a) Free-energy ΔG of a system containing a droplet of radius r.

(b) Variation of critical nucleus properties with substrate temperature.

Consider the effect of the substrate temperature on the critical radius. In Fig4.4(b), r_c, as given by eq.(4.2), and $\Delta\mu_c$, from eq.(4.4), are plotted versus substrate temperature T. Because $\Delta\mu_c$ increases with decreasing substrate temperature, r_c decreases. It is straightforward to understand that the critical radius will determine the column diameters of the further growth, thus the column diameters have the similar relation with the substrate temperature. Fig.4.5 shows such a dependence of the CsI column diameter on the substrate temperature. One should note at very low temperature < 50 °C (high sopersaturation in case of condensing vapors), the nucleus structure itself may become, in essence, amorphous.
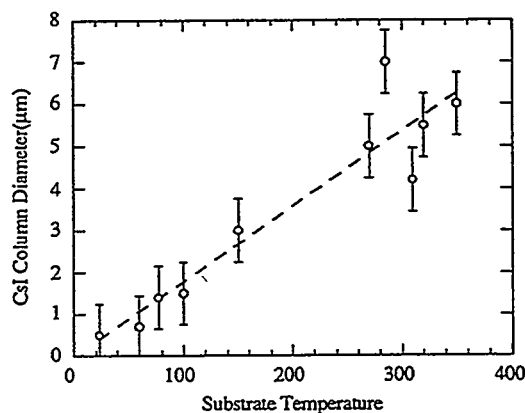

(a)
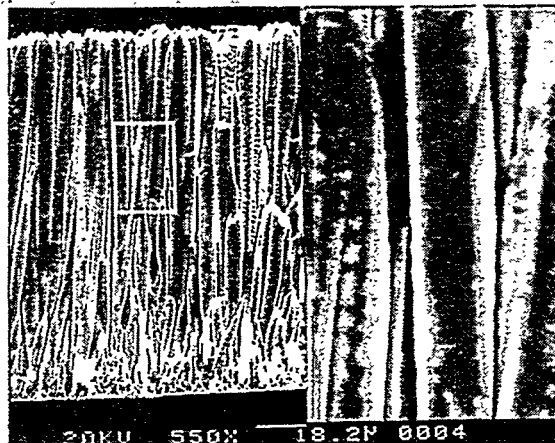
(b)
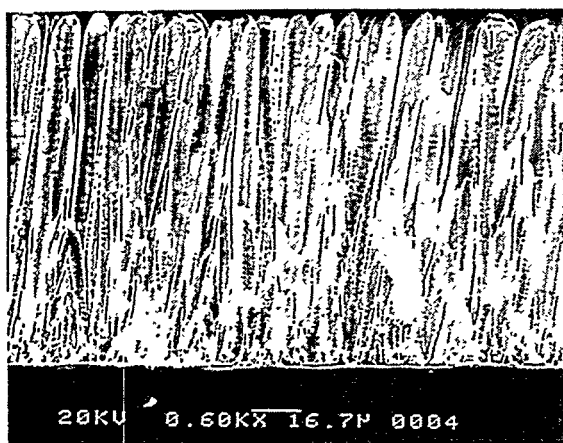
(c)

(d)

Fig.4.5 The dependence of the CsI column diameter on the substrate temperature.
(a) T=100°C; (b) T=150°C; (c) T=200°C; and (d) diameter vs. Temperature.

85

The dependence of the free energy of an aggregate on its size is also shown in Fig.4.4(a). Below this critical size the free energy will increase with increasing r so that the nucleus will tend to disappear, i.e. an atom is taken away from the critical nucleus, it dissociates again as illustrated in Fig.4.6(a); above r* the free energy will decrease with increasing radius so that the nucleus will tend to grow, in other words, if an additional atom is added to an aggregate of the critical nucleus, it becomes more stable and will, on the average, not dissociate into single atoms but will grow to form a larger, permanent island. Such a formation of nucleus is best illustrated by Fig.4.6(b). The SEM picture shows that nuclei with bigger diameters ($>r_c$) grow faster, and form permanent columns. While smaller nuclei tend to disappear, leaving empty area around the big columns.
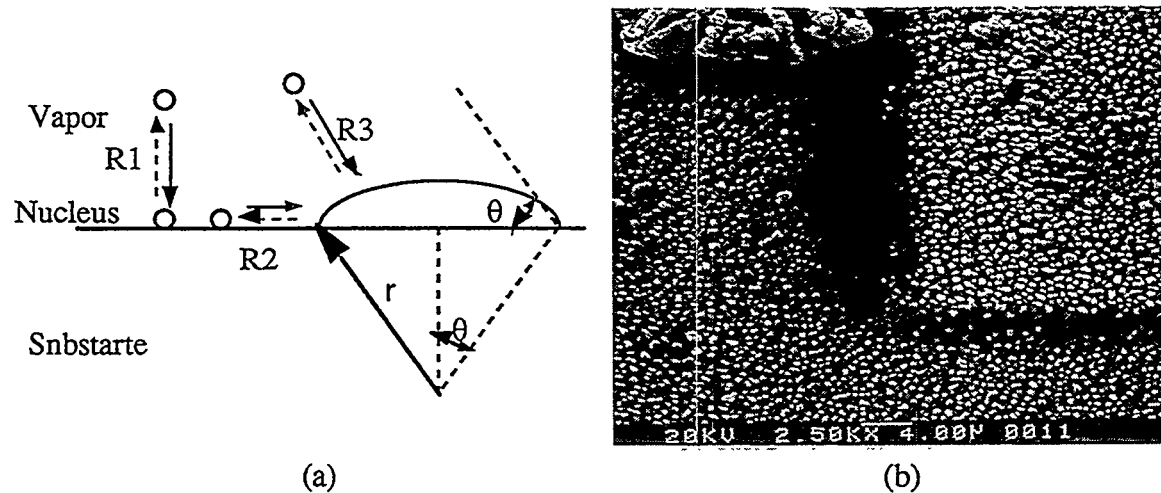

(a)   (b)

Fig.4.6 (a) Schematic of spherical cap-shaped nucleus on substrate. When r $>r_c$, more atoms move in solid arrow direction; if r$<r_c$, more atoms dissociate from nucleus along dashed arrow direction. (b) Initial stages of nucleus of CsI, smaller nucleus tend to disappear, the larger diameter nucleus grow higher and form the layer.

Another characteristic of homogeneous nucleation is the so-called "rate of nucleation", J, i.e., the number of nuclei formed in a unit of nontransformed volume per unit of time

$$J = A \exp(-\Delta G_c/kT) = A \exp\left[-\frac{16\pi\Omega^2\alpha^3}{3kT\Delta\mu^2}\right],$$ (4.5)

86

Here, A is a constant or slowly changing parameter. As can be seen, the nucleation rate depends very strongly on supersaturation $\Delta\mu$ or supercooling ΔT, and there exists a critical supersaturation (or supercooling) below which practically no nucleation takes place and above which it proceeds vigorously. The critical driving force (supersaturation or supercooling), in fact, determines the range of metastability of a given system. The value of the preexponential factor A is not known; however, owing to the strong dependence of J on $\Delta\mu$ or ΔT, it is possible to estimate the factors if one makes reasonable assumptions for J.

(b). Heterogeneous Nucleation

In practice, we almost always deal with heterogeneous nucleations, i.e., with formation of nuclei on some interfaces. Moreover, in principle, the interfaces can be nonuniform, i.e., can contain some irregularities; in this case, microheterogeneities of the interfaces should be considered.

This section will present a brief description of the principal ideas of heterogeneous nucleation, with emphasis on the shape and behavior of crystalline nuclei on substrates. The ideas will then be applied to CsI growth on patterned substrate.

The classic scheme of heterogeneous nucleation is depicted in Fig.4.7. In the isotropic approximation, a nucleus on a substrate is represented by a sphere segment the surface of which forms a wetting angle θ with the substrate, and for surface energies we have the relationship

$$\alpha \cos \theta = \alpha_{SM} - \alpha_{SS}, \qquad (4.6)$$

where S denotes the substrate and α_{SM} and α_{SS} the substrate medium and substrate-solid nucleus interface, respectively.
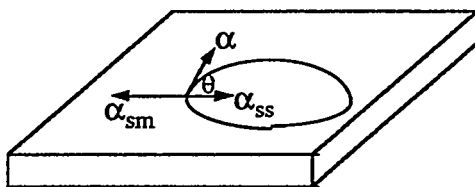

Fig.4.7 Schematic of the surface
energies of a nucleus on
a substrate.

87

The free-energy change (i.e., the potential barrier) for the heterogeneous nucleation is given by[16]

$$\Delta G_c^* = \frac{16\pi\Omega^2\alpha^3}{3\Delta\mu^2} \cdot \frac{(1-\cos\theta)^2(2+\cos\theta)}{4} , \tag{4.7}$$

where the second multiplier represents the so-called "Volmer factor"[17]. It has values from 0 (at $\theta=0$) to I (at $\theta=180°$); i.e., heterogeneous nucleation is in every case more favorable than homogeneous nucleation.

The first extreme case ($\Delta G_c^*=0$) corresponds to complete wetting: No potential barrier for condensation or crystallization should be overcome in this case; moreover, under some conditions, condensation or crystallization is possible even at undersaturation (see below). The second extreme case corresponds to complete nonwetting (the substrate is absolutely ineffective for nucleation). In an intermediate case, the barrier is significantly lowered, and, for example, even at $\theta=45°$, its height is about one order of magnitude smaller than that for homogeneous nucleation. The critical radius of the nucleus in this case is determined by an equation identical to equation (4.2). This means merely that at a given $\Delta\mu$, the equilibrium over any area of the substrate depends only on the curvature of this area, and not on the shape of the remaining surface, whether it is a complete sphere or is truncated. From this, the physical sense of heterogeneous nucleation becomes clear: A given amount of the material, when it wets a substrate, forms a sphere with a radius that can be far larger than the radius of a sphere formed from the same amount in homogeneous nucleation. This is why a large nodular defect or hillock can start from a small foreign particle (impurity) on a substrate, as we will discuss it in detail later.

For a disk-shaped critical nucleus, corresponding to usual crystal growth, we have

$$\Delta G_c=\pi\Omega\alpha^2 a/\Delta\mu ; \qquad r_c=\Omega\alpha/\Delta\mu, \tag{4.8}$$

where r_c is the radius of the disk, a the lattice parameter. These formulas were first obtained by Volmer. If a crystal grows by two-dimensional nucleation, its growth rate is in fact determined by the nucleation rate, J, which is expressed in this case as follows

$$J = C \exp\left[-\frac{\pi\Omega\,\alpha^2 a}{kT\Delta\mu}\right], \tag{4.9}$$

The coefficient C, in this case, is measured in $cm^{-2}\,sec^{-1}$.

One important point should be noted in connection with equations (4.8) and (4.9). The nucleation rate depends strongly on surface energy (or edge energy), which is very sensitive to the kind of crystallization medium, to adsorption of impurities, and so forth. For this reason, ledges, cracks, and other such imperfections on a substrate will, in general, catalyze nucleation. For example, for the case of a substrate corner with a 90° angle, the nucleation rate at the corner will exceed the rate on a flat surface for all contact angles as shown in Fig.4.8. Furthermore, there will be little surface-energy barrier to nucleation at such a edge, so that the preferential nucleation at edge is very pronounced under such conditions. In general, nucleation catalysts will lower ΔG. Thus the presence of such preferred sites will enhance the nucleation rate J. With the same principles, we will demonstrate the formation of CsI hillocks in the section 4.3.3 and 4.3.5. Based on the theory of the preferred nucleation discussed above and the mechanism of hillock formation, we developed the technology of the fabrication columnar structure CsI enhanced by substrate patterning as shown in section 4.
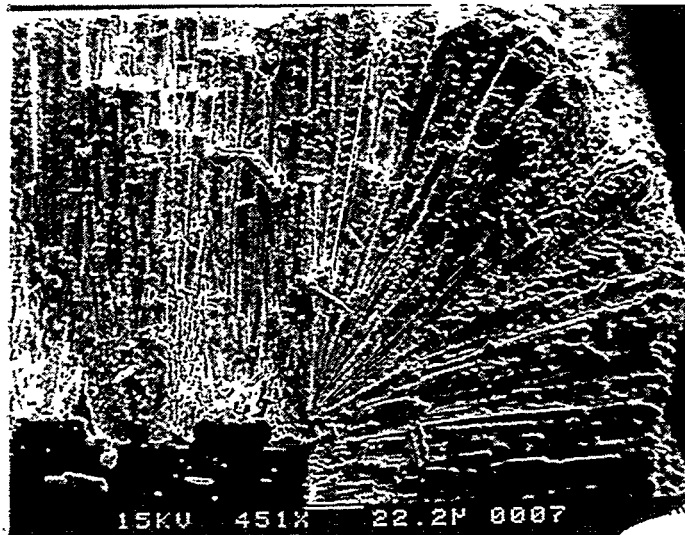

Fig.4.8 CsI layer grows on the edge of the substrate, growing rate at the corner is faster than the rest of the substrate.

89

4.3.2 Structure zone diagrams

The first phenomenological scheme was given by Movchan and Demchishin [18] in terms of a structure zone model (SZM), where the morphology (columns, crystallites) was set into relation to the reduced substrate temperature T/T_m (T substrate temperature, T_m melting point of the deposit) during deposition. Later, Thornton [19,20] and Messier et al. [21], extened this scheme was to include typical sputtering parameters (inert gas pressure, bias voltage,) as well as the thickness dependence to give a more comprehensive picture of the PVD grown film structures. According to the generalized SZM as shown in Fig.4.9, at low substrate temperatures ($T/T_m < 0.3$), i.e. in zone I, we meet fibrous crystallites with domed tops, which are separated by open boundaries. The structure of zone I films is essentially determined by the aggregation process, because at low temperatures most of the relaxation processes are frozen in.
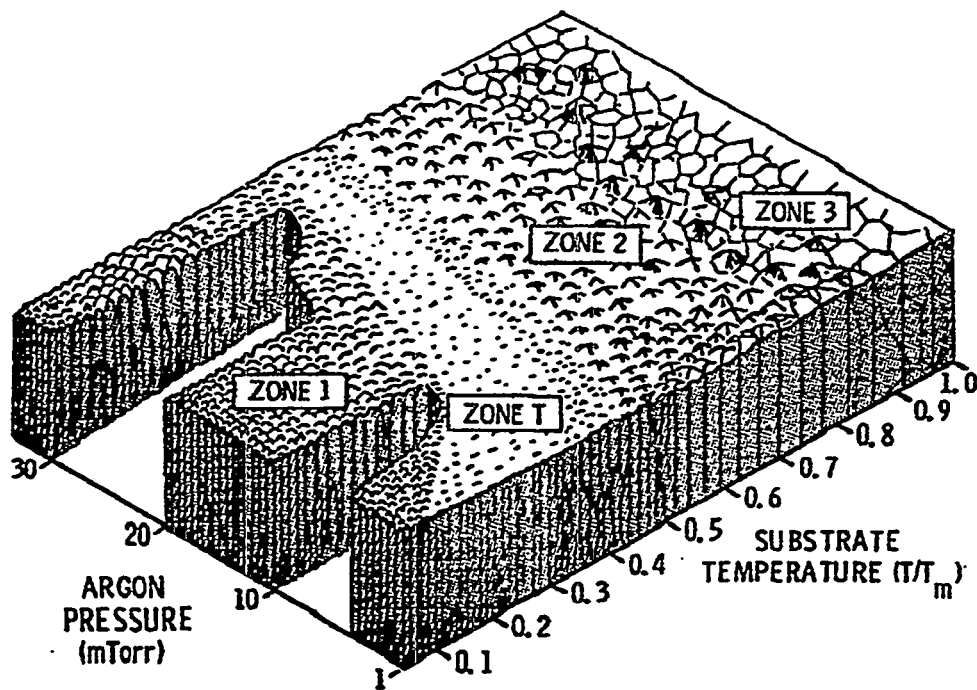

Fig.4.9 Structural zones in condensates at various substrate temperature and working gas pressure.

90

In zone II ($0.3 < T/T_m < 0.5$) the film consists of well defined columns, separated by dense grain boundaries. Dislocations are located predominantly in the neighborhood the grain boundaries. The grain size increases with increasing T/T_m, and near the transition region to zone III, with increasing film thickness. The diameter of the columns is governed by the mobility of the adatoms.

The structure of zone III ($0.5 < T/T_m < 1.0$) is characterized by well formed crystallites with smooth, faceted faces. The grain size depends on the reduced substrate temperature T/T_m. Additionally, in sputtered films a so-called zone T (T transition) can be found, which is intermediate between zone I and zone II: the film consists of a dense-packed array of thin, well-defined fibers. For sputtered films[22-24], zone I appears only at relatively high inert gas pressures, because at low inert gas pressures the impact of ions and neutrals would destroy the fragile zone I structure. Other deposition parameters, like deposition rate[25] in relation to the impinging rate of residual (reactive) gas atoms, also have a certain influence on the structure development, but they have not been included in the SZM.

As demonstrated in a later section, for higher collimating light properties, CsI structure should fall in Zone I of the SZM.

A growth model should explain as well as possible the above mentioned dependence. From the experimental data the following structure-growth philosophy for thin films can be derived: the morphology of thin films is a result of a number of competing processes, resulting in a destabilizing aggregation and a stabilizing relaxation.

### 4.3.3 General features of hillocks to be explained by a model

Hillocks (nodular defects) are a general phenomenon in thin film deposition processes, mostly leading to some deterioration of the film properties[26,27]. However, when the growth of such hillocks is well controlled, it could be beneficial to its properties,

91

such as better columnar structure and less stress. We will discuss the principle of nodular defects in detail, because this leads the idea of using patterned substrates to enhance CsI columnar structure, further improving the spatial resolution. The shape of the hillocks is of a cone type; hillocks appear as isolated, fused or clusters of nodules (for more detailed information see [28 to 30]. In general, their growth starts at surface asperities like debris, scratches, inclusions, dust particles, and so on. Fig.4.10(a) and (b) show such a hillock
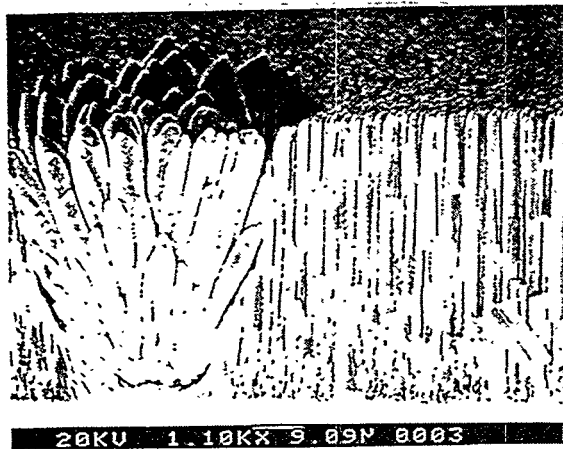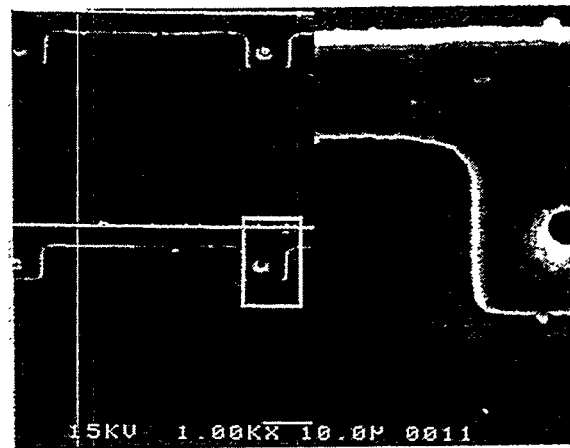

(a)
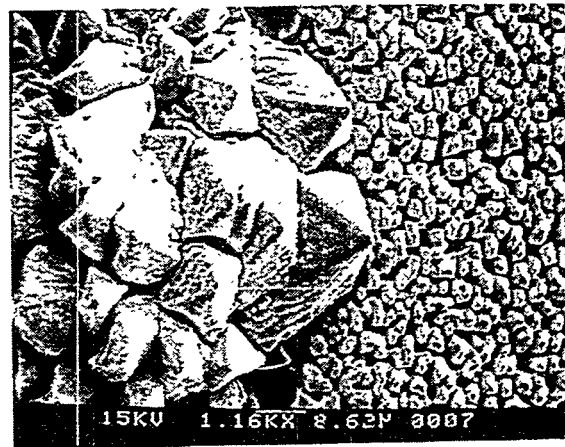
(b)
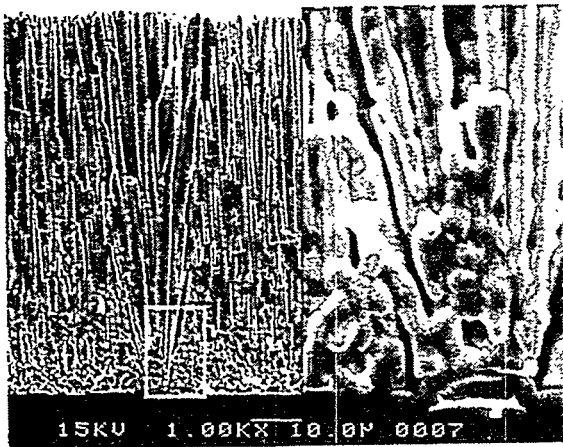
(c)

(d)

Fig.4.10 SEM of nodular growth of CsI (a) cross section of a nodule due to a
particle on a substrate; and (b) top view of the nodule.
(c) the metal connection dot induces a nodular defect and (d) the top view
of the substrate before deposition.

92

growth starting from a defect particles. Fig.4.10(c) shows the CsI deposited in a photosensor array; the similar hillock growth is initialized from a metal dot which connects the diode pixel to the reading line as seen in Fig.4.10(d). Clearly, this nodular defect will degrade the resolution of the imaging and the uniformity of the light transport path. There is some evidence that chemical inhomogeneities can also cause hillock growth[31]. The connection between the hillocks and the adjacent columns is not as strong as between the columns mutually, so that the nodular defects are loosely bound to the thin film. Cracking around the nodule appears often, so that these places represent weak points in the mechanical properties of the film.

As revealed by cross-sectional SEM Fig.4.10(a), the hillock has a cone-like internal structure. The close-packed crystallites reach, however, significantly greater diameters in the nodule than in the columns of the surrounding film. No significant difference in the composition between the hillock and the adjacent film could be observed. The presence of (gaseous) impurities seems to promote the occurrence of conical hillocks. High working gas pressure (connected with low floating potential as well as with low kinetic energy of impinging particles and large impinging angles) promotes hillock formation.

As hillock formation is essentially induced by surface inhomogeneities, where the underlying growth processes are the same as in usual thin film growth, we assume that a growth model as described in Section 4.3.2 is also able to outline the main phenomena of nodular growth.

4.3.4. Description of the generalized ballistic aggregation (BA) model

The starting point for developing the growth model is the ballistic aggregation process of hard disks, introduced by Leamy et al. [32] for the explanation of the columnar structure in evaporated thin films, especially of the inclination of the columns, which significantly differs from the direction of incidence of the particles. However the approach

of sticking atoms was too crude, and for a better explanation of the experimental results the BA model was developed further, first by Henderson et al. [33] by introducing an appropriate atomic relaxation scheme.

(a) Mass transportation and aggregation

Fig.4.11 shows schematically the aggregation process. The particles move on straight trajectories towards the film surface until they collide with an already deposited particle or with the substrate. After that, they relax into the next stable position.

Considering an evaporation process, the particles move on their way from the localized source to the substrate on parallel trajectories with a certain angle of inclination, which depends on the geometrical arrangement of the source and the substrate holder. When the chamber pressure is elevated with inert gas, the particles will experience multiple collisions on their way toward the substrate, thus they move with larger angle of inclination. The particles arrive stochastically with a certain angular distribution $N(\varphi)$. The function $N(\varphi)$ is influenced by the geometry of the deposition arrangement, the inert gas pressure inside the deposition chamber, and has to be determined experimentally or is subject of a separate theoretical investigation (for instance see [34]).
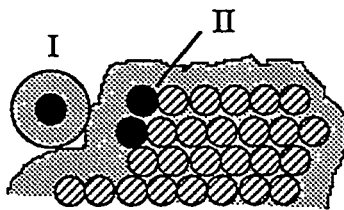

Fig. 4.11 An impinging atom (full circle,I) with its capture (i.e. dotted) area, sketched for various times Atom I was captured by a previously deposited atom (II) and relaxed into the next stable position.

In this model, the angular distribution of the oncoming atoms is mostly considered as a homogeneous distribution in the angular range $\varphi_0 \pm \frac{1}{2}\Delta\varphi$, where φ_0 is the mean of angle of incidence and $\Delta\varphi$ the mean square deviation of the distribution. If we consider a gas pressure of some 10^{-1} to 10 Pa, the mean free path of the vapors is in the range of some tens of millimeters to some centimeters. That means that an atom on the way from the

94

source to the substrate will collide several times with neutral gas atoms, which results in the case of small free paths in a thermalization of the deposited atoms. On the other hand, the mean free path is large in comparison with the size of typical structural units of the growing film (columns), so that the ballistic aggregation regime need not to apply and is to be substituted by the diffusion limited aggregation regime.

Immediately before reaching the film surface, the trajectory of the particle does not remain straight due to the interatomic potential between the approaching particle and the film surface atoms. If we take into account that the range of the interatomic potential is very short (only a few 0.1 nm), it is not necessary to calculate the whole trajectory using Newton's law, but it is possible to take into consideration the effect by introducing some capture cross section area for each atom, the diameter of which depends on the particle's kinetic energy and the binding energy between the atoms as well. For a better estimation of that parameter we refer to [35]; after the first collision (with respect to the capture area) the incoming atom "rolls" into the next cradle; the direction of rolling depends on the angular momentum of the atom after sticking to the "collision partner" [33]. Therefore we assume the interaction potential to be isotropic.

(b) Relaxation processes, surface kinetics, and desorption

After reaching the surface, in general an atom will not reside at the place where it was deposited. At first, due to the surface diffusion the surface will be reconstructed all the time, and second particles will desorb with a certain probability from the surface. Both processes are thermally induced. The desorption rate as well as the diffusion rate for each atom will depend on the binding energy and thus on the local configuration of the atoms. For desorption, a surface atom should receive an impact with an energy greater than the binding energy of the atom. If we assume Boltzmann statistics, the resulting probability P_i^- for a surface atom with the binding energy E_{bi} is

$$P_i^- = \exp(-\frac{E_{bi}}{kT}), \tag{4.10}$$

95

where k is the Boltzmann constant and T the absolute temperature of the substrate. The desorption rate K_i^- will be connected with the phonon frequency v_s, which is assumed to be independent of the local configuration, and is given by

$$K_i^- = v_s P_i^-,$$ (4.11)

The that the local surface temperature may differ from the substrate temperature due to the kinetic energy of the oncoming particles(in our study, we shut off the substrate heater and use cooling system to maintain the stability of the substrate temperature) will be neglected . If the binding energy is assumed to be additive and isotropic, and if only nearest neighbors are taken into account, we get

$$E_{bi} = \sum_{j \in n(i)} \Phi_{s(i)s(j)},$$ (4.12)

In eq.(2) Φ_{AB} means the energy of "one" bond between an atom A and an atom B, which is independent of other neighbors, s(k) denotes the sort of the atom number k and n(i) the set of the next neighbors of the atom number i. In this case a "next neighbor" is an atom, the center of which is located inside a circle of a radius αr_p around the center of the reference atom, because we consider a certain truncated range of the interaction potential. An atom can desorb by thermal activation, as well as it can diffuse due to the same process. The corresponding jumping rate is given by

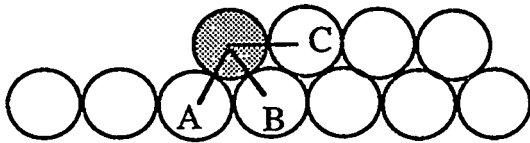$$K_{k \to l} = v_s \exp(-\frac{E_{bi}}{kT}),$$ (4.13)

Fig.4.12. The hatched surface atom has three next neighbors A, B, and C. To jump to the right, it has to break its bonds to atoms A and B, to jump to the left the bonds to B and C.

In Fig.4.12, for the estimation of the activation energy E_{kl}, the following typical situation is outlined: if, for instance, the hatched labeled surface atom attempts to jump to the right, it has to overcome its bonds to the neighboring atoms A and B, where the bond to atom C (it works as a "joint") is not influenced (remember central symmetry). In the opposite case (i.e. jump to the left), the bonds to the atoms B and C have to be broken. Therefore, the diffusion barrier for a jump of the atom i from site k to site l can be written as

$$E_{kl,i} = E_{bi} - \Phi_{s(i)s(\text{first neighbor in jumping direction})} \, ,$$ (4.14)

so that in general the jumping probability does not depend only on the local configuration.

Only surface atoms with two or three next neighbors are allowed to diffuse, because under the described conditions the jumping probability for atoms with four and more next neighbors is so small, that it can be neglected. The growing structure will be determined essentially by the ratio τ_s/τ_{ml}, where τ_s is the mean time between jumps, and τ_{ml}, the mean time for the deposition of one monolayer. It determines, how many trials remain for the relaxation of the sparse ballistic aggregate.

The corresponding mean time between two jumps for a "mobile" surface atom (i.e. with only two next neighbors) will be given by[36]

$$\tau_s = v_s^{-1} \exp(6 + \frac{5T_m}{T}),$$ (4.15)

The time for the deposition of one monolayer τ_{ml} can be considered as experimentally determined number and strongly depends on the conditions of the experiment. From that, it is possible to obtain the model parameter $\{n_s/n_e\}_i$, which gives the mean number of successful jumps for every mobile surface atom of the sort i and all types of binding. It is quite easy to obtain with ($L/2r_p$ as the number of surface atoms of the substrate) the result

$$\frac{n_s}{n_e} = \frac{3\tau_{ml}r_p}{\sqrt{2}\tau_s L},$$ (4.16)

If common deposition rates (0.1 to 1 μ/min) are considered, the surface diffusion becomes significant for $T/T_m \sim 0.25$ (at that value n_s/n_e becomes ~0.05 for $L \sim 5000r_p$). This value coincides quite well in zone I in Thornton's structure zone diagram.

In connection to equations (4.13) to (4.16), let us examine their physical meaning in our experimental deposition of CsI. When working gas pressure is elevated , vapors reduce their kinetic energies though multiple collisions with inert gas atoms. Thus their diffusion energy barriers, E_{kl} from eq.(4.14), will become higher, the corresponding jumping rate $K_{k \to l}$ from eq.(4.13) will be lower. Clearly, this low diffusion process will ensure further growth of CsI columns. On the other hand, with increasing substrate temperature, the jumping rate will be higher and jumping time, τ_e from eq.(4.15), will be shorter, therefore the fast diffusion process will result in columns to coalesce to form larger ones and gradually join up.

4.3.5 Growth of hillocks and topological induced columns.

In this section we investigate the consequences of a hillock "seed" for the growing structure, which is according to Section 4.3.3 the main reason for hillock growth.

Concerning the internal structure of the hillocks a fan-like pattern can be recognized, indicating the formation of cone-shaped crystallites with an upper diameter which essentially exceeds the diameter of regular columns in the film.

As shown in Fig.4.13, a certain surface diffusion is necessary for the growth of well-defined hillocks. If surface diffusion vanishes, the structure of the film is very sparse, and an asperity at the surface cannot cause structure disturbation effectively. On the other hand, if the surface diffusion is extremely high, only very large dust particles can induce nodular growth, because the diffusion would level out the nodule in such a case. Fig.4.14 shows the CsI growth on a rough surface which is roughed by very fine sandpaper.

Because there are many irregular surface asperities, nodule growth can not be induced by every particle, only a big site as pointed in Fig.4.14(b) promotes a nodular growth.

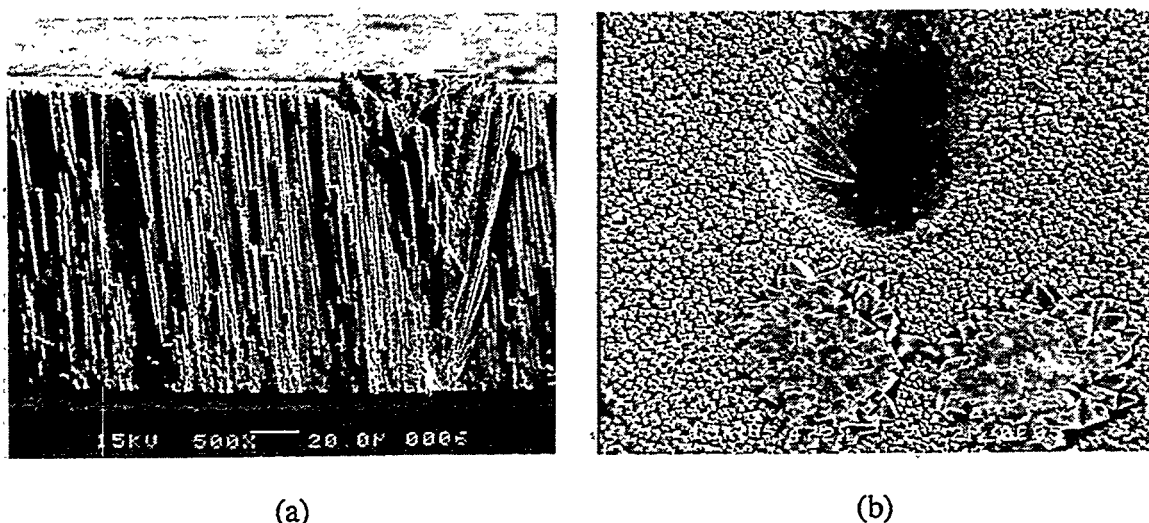(a)   (b)

Fig4.13 The nodular growth of CsI. (a) cross section of the nodule; (b) top view of three nodules, one of these is removed from surface due to its loose bond.

Growing nodules are relatively stable against surface diffusion, because the gap between the nodule and the undisturbed surrounding film enhances the diffusion path for the adatoms, so that the filling up of the gap will go on very slowly as shown in Fig.4.13(a).
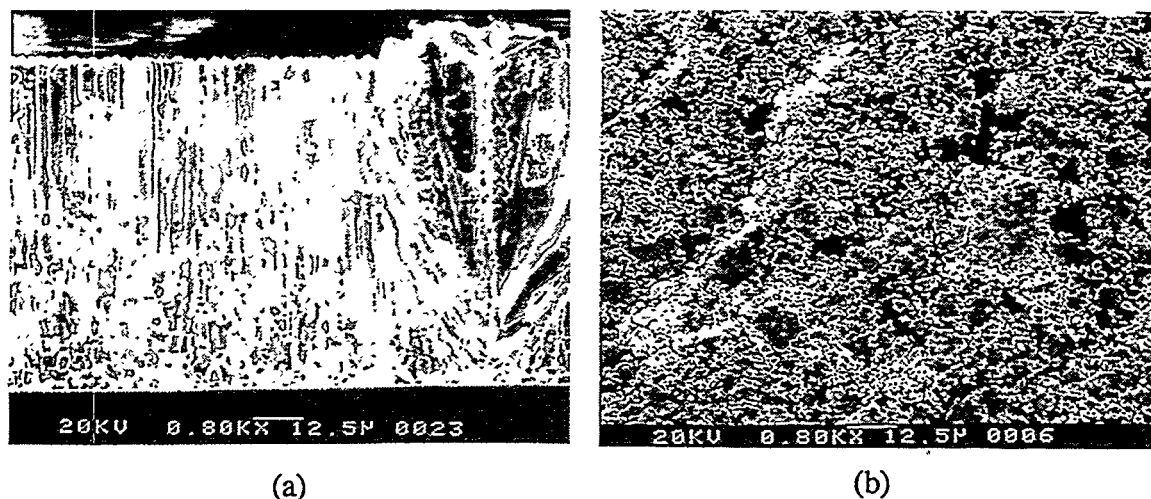

(a)   (b)

Fig.4.14 The nodular growth on a rough surface.(a) cross section (b) bottom view.

99

As demonstrated in Fig.4.14, for pronounced hillock formation a certain angular distribution of the incoming particles seems to be necessary. For a steady collimated particle beam the surface asperity causes almost no disturbance in the growing structure. Wide angular distributions yield open grain boundaries and a lose bond of the nodule to the surrounding film. Fig.4.13(b) shows the top view of three nodules, two of these remain within the CsI film, the another was removed from the surface due to its loose bond to the surrounding columns and small contact to the substrate, and left a cave behind.

So far we have analyzed the mechanism of the formation of hillocks or nodules. By analogy, we can induce a similar nodule-like columns in a controllable manner and further influence the surrounding film growth with better column structure. Line ridges instead of particles were patterned on a substrate with square pattern to form a mesh-like strcture as shown in Fig.4.15. CsI will preferably initialize heterogeneous nucleation on the ridge lines similar to the formation of nodules since less free energy change of the adatoms is required (refer to eq.4.9) due to the larger incident angles caused by curvatures of lines. By controlling the parameters properly as shown below, leading columns are formed starting from ridge lines. These leading columns function as guides to the surrounding film growth. Due to the uniform forcing action between the leading columns and surrounding columns through out all the film during the all growth process, a well organized columnar structure of CsI can be obtained as shown in Fig.4.15. Such columns extend up to 450 µm high from the substrate without any discontinuity.

As a contrast, Fig.4.16 shows a CsI growth on a flat substrate at the same deposition condition. It is clearly seen that One can see clearly that this layer consists of a number of gains whose boundary will scatter the scintillation light, hence degrading the imaging resolution. Certainly, line sizes and ridge heights affect the formation of the growth, which will be addressed in the next section.
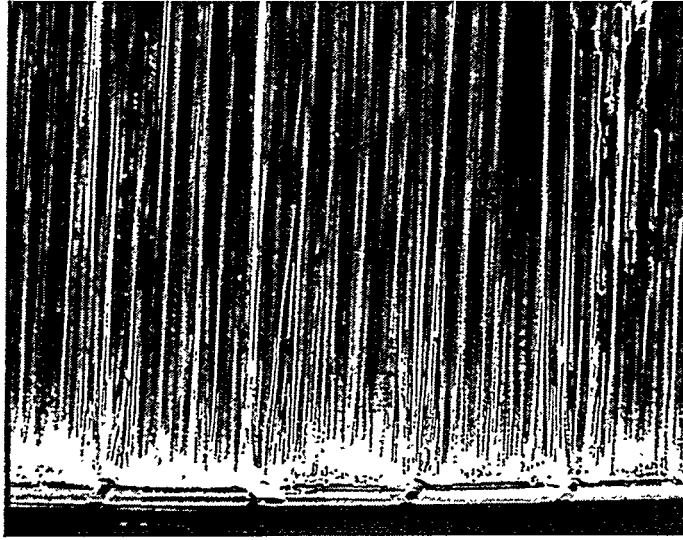
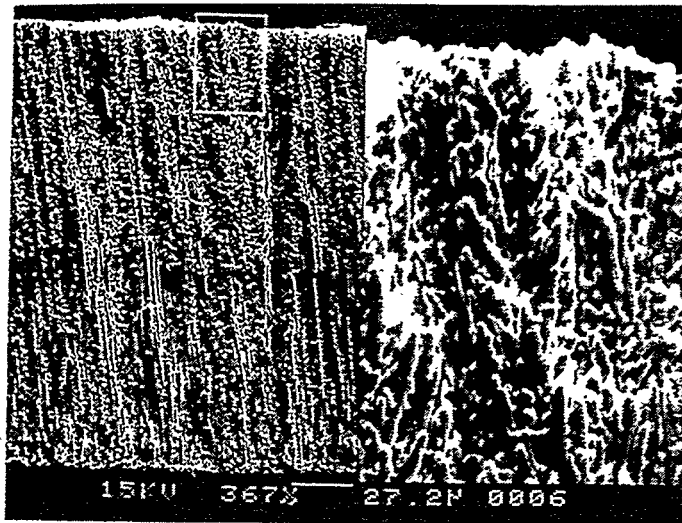Fig.4.15 Columnar structures of CsI induced by patterned ridges.

Fig.4.16 Cross section view of CsI deposited on a flat substrate.

The application of such patterns also extends to using other geometrical substrates. The formation of columns is promoted by a relatively high working gas pressure. Increasing the capture radius of the particles also leads to a pronounced hillock formation and a weaker bond of the nodule to the surrounding matrix of the undisturbed film, due to open grain boundaries and to an enhanced protrusion above the film surface as seen in Fig.4.14(a)..

101

4.3.6 Substrate pattern geometry effect on CsI growth

As seen above, a particle or impurity on a substrate will lead to hillock formation with a fan-like pattern with much larger diameter than the surrounding columns in two dimensions. This is the type of structure we should avoid. The favorable structure is as shown in Fig4.15, where the ridge induced columns are not significantly larger than the surrounding columns. This requires a suppressing force to expanding growth of the columns induced by ridges. Along the ridge line there is no space for the column expansion, thus a suppressing force normal to lines should be applied to the ridge induced columns.
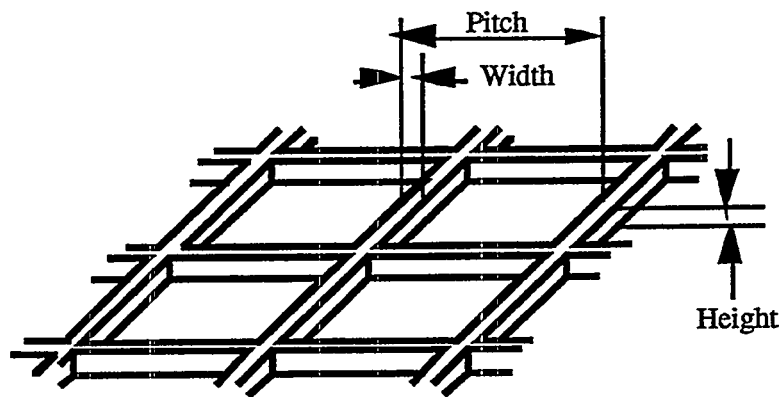
Fig.4.17 Mesh pattern of polyimide defined on a glass substrate
by photolithography.

One way to achieve this is that neighbor columns should have the same growth rate as the main columns, which requires that ridge heights should be small ~2-5 μm, and flat portions should be of the same material as the ridges in order to have the same nucleation rates. Another requirement is that lines should not so be close that not enough space needed for regular column growth is left. Thus line-line pitch should be larger than 40 μm and line width be comparable to the column size, 2-5 μm.
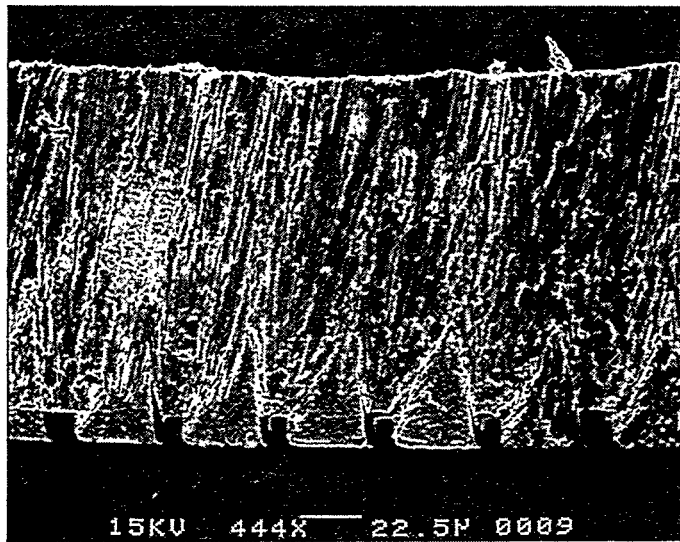
Fig.4.18 CsI fan-like structure on a inappropriate patterned substrate.

With an inappropriate geometry size of pattern, nodular growths normally formed. For exmaple, Fig.4.18 shows such a CsI structure with cone-shaped structure due to higher ridges. Considering the initial growth at the ridge sites, at the first 10 μm, the growth starting from the ridge has no competition growth around it; there is space for it to expand since growth from flat portion comes up later, thus growth expands quickly and forms typical nodular defects. They grow continuously and gradually close each other.
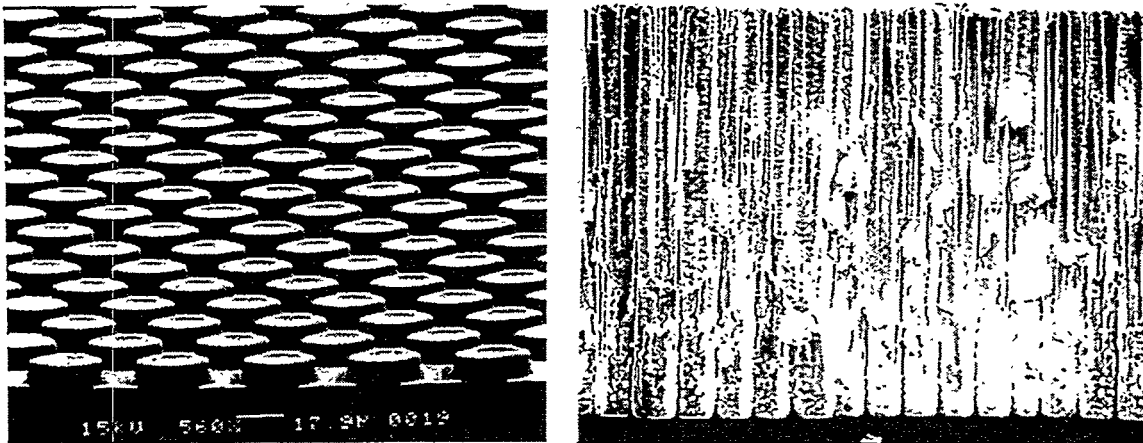

Fig.4.19 CsI growth on a "puck" pattern substrate.(a) The patterned substrate.
(b) Cross section of the CsI layer;

103

Another scheme to form columnar structure in CsI is by suppressing the expanding of the nodular-like columns. If the low portion of a substrate is small compared to the upper portion, there will be little growth in the lower portion or between the upper sites. Fig4.19(a) shows a "puck" substrate. The raised portions are larger than the lower ones. Since each growth starting from the puck has 6 neighbor column s, there is no room to expand to form a nodular defect. Moreover, the interactive suppressing force will promote the columnar formation as shown in Fig4.19(b). In this case, the height of the raised portion is not important as long as it can promote fast nucleation on it.

4.3.7 Kinetic promotion of column growth

As deposition continues these columns begin to grow and also may coalesce to form larger ones which, in turn, gradually join up. This sequence is illustrated in Fig.4.19(b), which shows a growth sequence for CsI on a puck pattern substrate.

There are two routes by which atoms can reach a column island and thereby cause it to grow. These are, as discussed in connection with nucleation, by direct addition from the vapor above the substrate and migration across the substrate surface. If the former were the dominant process we should expect the column to grow more rapidly in height than in area. However, for this to occur a very high rate of deposition combined with a large value of surface diffusion energy barrier and a low substrate temperature would be required. In practical cases the surface diffusion energy barrier, E_d, is small and growth of the nuclei is dominated by surface migration. Clearly there must, at some stage, be a transition from migration-dominated growth to direct addition from the vapor since when the film is continuous only the later can occur.

It is well-known that varying the interaction between the adatoms and the substrate leads to various growth modes[37]: layer by layer or Frank-van der Merwe growth for strong interaction, island or Volmer-Weber growth for a weak one and, as a special case

between the two, the Stranski-Krastanov growth, where the interaction between the adatoms and the deposit additionally depends on the thickness of the already deposited film. Nevertheless, it is a well established fact that the growth mode depends on the growth kinetics, too, i.e. column growth can be promoted kinetically by an elevated working gas pressure.
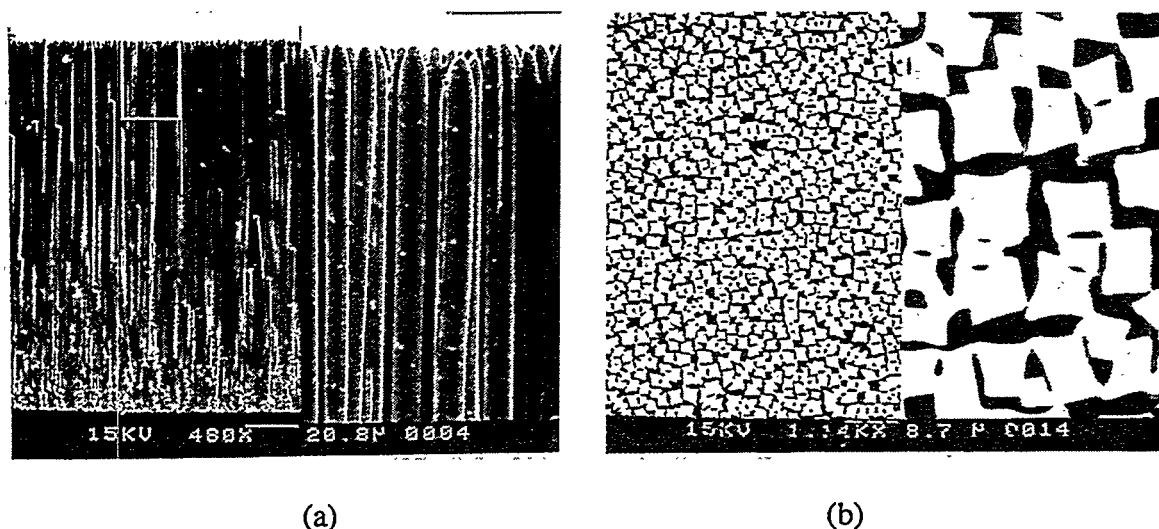

(a)   (b)

Fig.4.20 (a) Columnar structure CsI deposited on a flat substrate with evaluated inert gas pressure. (b) Top of view of the layer.

As stated in section 4.3.4, vapor atoms can reduce their kinetic energies through the collisions with the inert gas atoms, hence increase their diffusion barriers. Recalling equation (4.9), larger incident angle due to multiple collisions will also reduce the free-energy change of the adatom, hence enhance columnar formation. In experimental situations this means that increasing the kinetic energy of the incident particles (i.e. decreasing capture radius) causes less pronounced hillock formation, which is not desirable for columnar structure formation. In order to reduce the kinetic energy of the incident particle, elevated pressures with inert gas are employed, thus the vapor reduces its energy by collisions before it reaches the substrate. In this way, the mobility of new adatom is

105

slowed down with less diffusion, which limits the column expanding. Moreover, the incident angle of incoming particle is increased through the collision. Therefore, with inert gas pressure, the film of CsI exhibits columnar structure even on flat substrate. Fig.4.20(a) shows such a columnar structure on a flat substrate. Fig.20(b) shows the top view of the columnar layer, each column is well separated with surrounding columns, thus it has a good light-collimating properties.

.

4.4 Experimental and Performance of Columnar Structure CsI

4.4.1 Evaporator setup

It is well known that dopant thallium atoms in alkali halide scintillators work as activators which play an important role in increasing the scintillation efficiency and in producing a longer wavelength emission spectrum than CsI(Na). This is a better match to the a-Si:H detector as shown in Fig.1.5. A homogeneous concentration of the Tl is necessary in order to optimize the performance of the CsI(Tl) scintillator. The conventional evaporation techniques do not produce deposits having the same composition as the source material when the vapor pressures of the constituents TlI and CsI in the evaporation boat are dramatically different[38]. The CsI(Tl) layers produced by this method have large gradients in Tl concentration. To avoid this problem we adopted a powder flash evaporation technique[39].
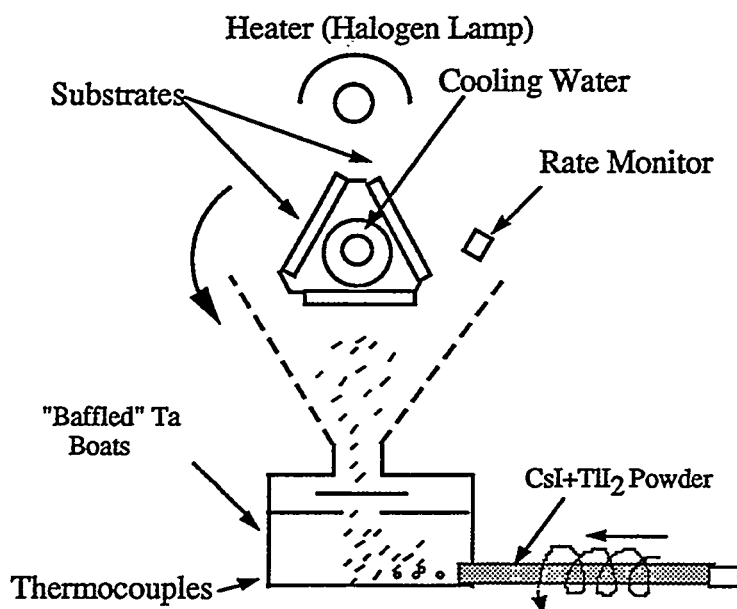
Fig.4.21 Schematic of setup for depositing CsI(Tl) layers.

The setup of the evaporator we used is shown schematically in Fig.4.21. The

source material is a powder mixture of CsI and TlI according to the predetermined Tl concentration. The CsI and TlI powder is pressed into pellets and then transported through a tube by a controllable motor and continuously fed into the heated boat. The boat is hot enough to ensure that the mixture vaporizes rapidly. The deposition rate is determined by the feed speed which is controlled by the motor. The substrates were placed on a rotating holder which was cooled by a water tubing system to maintain the substrates at 100-150 C^0 during the evaporating process. The chamber initially was pumped down to 10^{-6} Torr. An inert gas, in this case, Ar, was then admitted into the chamber which was then maintained at about 5m Torr during the process. Ar atoms modify the transport paths of the vapor toward the substrate by scattering, which enhances the columnar structure of the CsI layers, thus improving the spatial resolution of the detector.

4.4.2 Light transmission

The experimental study of light transmission (or absorption) in the scintillator layer is conveniently performed by direct excitation of the CsI(Tl) layers by a LED light source with wave length 565 nm, which simulates well the peak (λ =550 nm of the CsI(Tl) emission spectrum[40]. A Hamamatsu photodiode, S1723-04, was used to measure the light intensity. Six CsI(Tl) samples evaporated on patterned substrates and on flat substrates with 300~600μm thickness were measured. The results showed that the light transmission of CsI on the patterned substrate was about 10-15 percent greater than that of the flat substrates. The main reason is probably that the thermally induced columns of CsI on flat substrate are not as straight as the ones on the patterned substrate, as shown in Fig.4.15 and Fig.4.16. Moreover, many grains exist randomly inside the CsI film; the boundaries of these grains will absorb as well as scatter the scintillation light. Furthermore, since the distribution of these grains is random, it will affect the uniformity of the scintillating efficiency, hence will increase the noise of the whole imaging system. By

contrast, columns of CsI on patterned substrates extended perfectly through all of the bulk, with little or no grain structure. Thus the light transmission is enhanced by the light guide mechanism.

4.4.3 Light output vs Tl concentration

The Tl concentration is known to affect the light yield in crystalline bulk crystalline Cs(Tl) [41]. A concentration of 0.1-0.2 mole percentage is required for an optimal light output[42]. The Tl concentrations in the evaporated layers were evaluated by Reflection Fluorescence analysis (XRF)[43]. The scintillation light output was measured using a Hamamatsu S1732-04 silicon photodiode coupled to the CsI(Tl) film. The light output was measured in terms of the number of photoelectrons produced on the photodiode per Mev of energy deposited in the CsI(Tl) film by a calibrated 50 KVp x-ray source. The light yields were plotted against the Tl concentration as shown in Fig.4.22. This graph indicates that for a good light yield, the Tl concentration should not be less than 0.02 mole percentage.
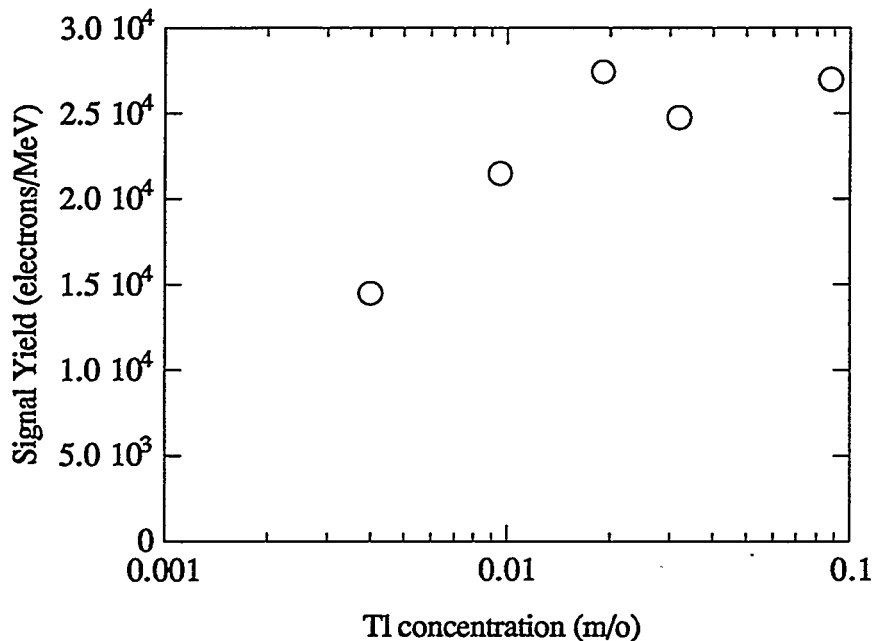

Fig4.22. Light yield vs Tl concentration

4.4.4 The effect of the heat treatment

The heat treatment of the CsI layer, not only changes its morphological structure but also affects the light emission efficiency. CsI samples were annealed at temperatures $200^{0}C$ to $500^{0}C$ for 30 minutes. The light output systematically increases with increasing the annealing temperature. As seen in Fig. 6, the initial annealing (from $150^{0}C$ to $250^{0}C$) causes a larger increase in the light yield than the higher temperature annealing. This light output effect of the heat treatment indicates that the annealing can cause the Tl atoms to relocate in the CsI by thermal diffusion processes, which therefore create more Tl^{+} luminescent centers and thus more effectively activate the CsI to emit the light. In addition, it should be emphasized that at the temperatures beyond $550^{0}C$ the annealing will degrade the CsI light yield because some of Tl atoms will escape from CsI surface due to the high equilibrium vapor pressure of the Tl. One should note that when CsI film is deposited on an a-Si:H substrate, annealing temperature is limited below $250^{0}C$ due to the emission of hydrogen of a-Si:H film at a higher temperature.
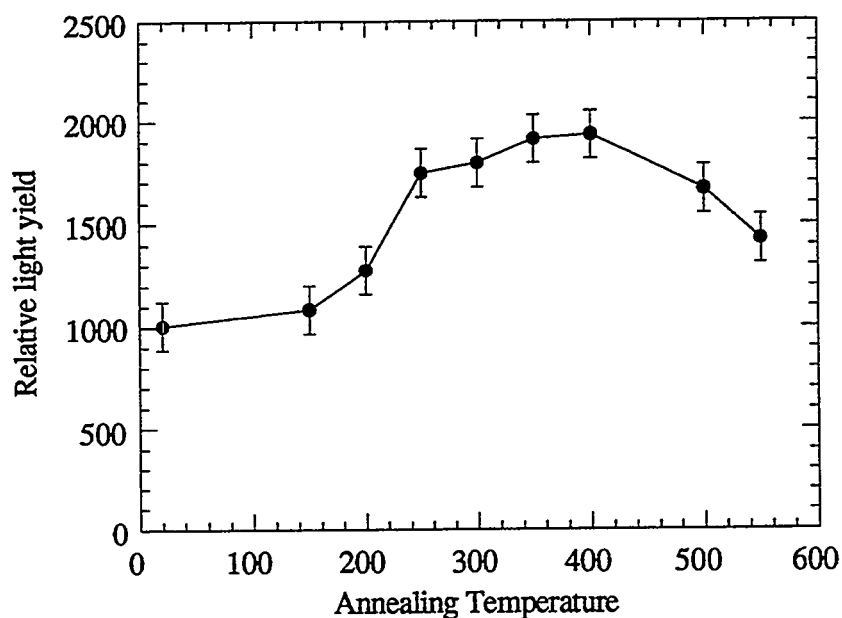

Fig.4.23 Light yield vs annealing temperature.

4.4.5 Radiation resistance of the bulk and film CsI

A scintillation screen, as the input radiation converter, absorbs most of the incoming radiation energy during long term medical imaging or high rate particle detection. It will undergo radiation damage, thereby decreasing the light yield. Thus there is concern over the sensitivity of the CsI(Tl) film which may limit its use in stable radiation detection. Previous data[44,45] has shown that the pulse height reduction from bulk CsI(Tl) is already significant at a dose level of 100 rad. We exposed an evaporated CsI(Tl) layer 125 μm thick to various radiation levels to determine its radiation tolerance. The irradiation was done with a strong γ-ray Cobalt-60 source at the irradiation facility at LBL. The nominal activity of the Co-60 source was 6000 Ci. The CsI sample was placed at calibrated positions 10-30 cm away from Co-60 source. An ion chamber detector was used to monitor the dose which determined the exposure time required for the total dose. The signal yield was measured after each exposure. It was normalized relative to its original signal output. Fig.4.24 also shown the data for a 1cm thick crystal CsI(Tl) taken from ref[46].
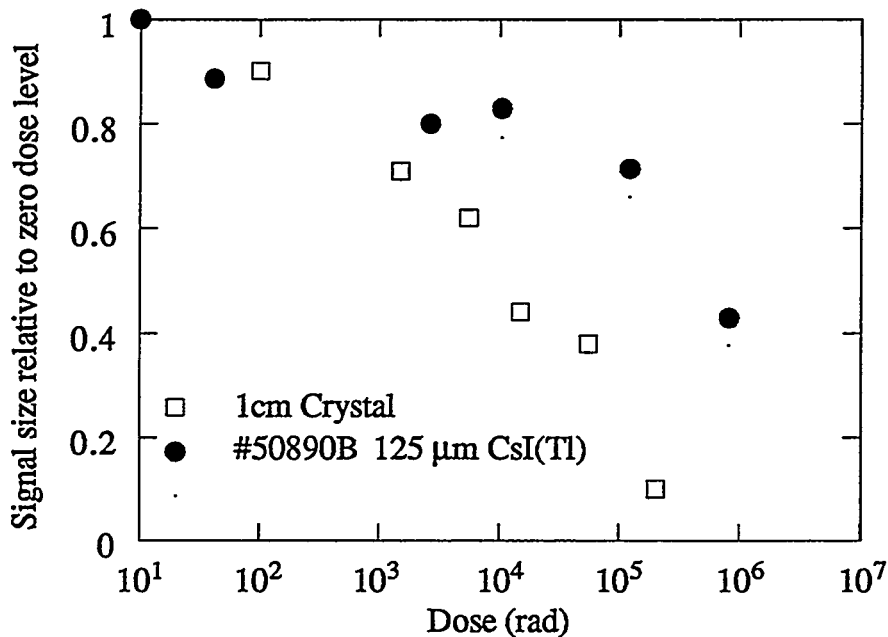

Fig.4.24 Radiation resistance.

As shown in Fig.4.24, the dose required to reduce the signal size by a factor of two for this evaporated layer is about 50 times larger than that for 1 cm thick bulk CsI sample. This suggests that the radiation damage changed optical transmission properties of the scintillator, in agreement with more detailed studies on crystal CsI[46].

Generally, there are two sources of radiation damage in CsI[46]. One is intrinsic. which causes coloration due to the F-center (a negative ion vacancy with one excess electron bound at the vacancy) and to other more complicated color centers. The other is extrinsic, which causes coloration and afterglow due to impurities. Both cause transmission loss of the scintillation light. Recovery from radiation damage, both transmission and light output, has been studied extensively[47,48]. A small amount of natural recovery was observed in CsI kept in the dark at room temperature for a period 30 days. Very little recovery was observed with exposure to UV light[47]. However, the quick damage recovery was reported by exposure to sunlight[46].

4.4.6 Fluorescence decay time

CsI and CsI(Tl) film with different Tl concentration were deposited by evaporation. The light yield timing spectra were measured by a table-top pulse x-ray system with a timing accuracy of about 100 ps, which combined a state-of-the-art laser diode and a light-excited x-ray tube as shown in Fig.4.25.

Analysis of the decay spectra of the bulk CsI(Tl) crystal which is the source material for the deposited CsI layer resulted in three decay periods: 900 ns, 1500 ns, and 3500 ns. The fast component dominates the total light yield. The rise time of the light peak ~80 ns can be easily seen by expanding the time scale of Fig.4.26(a). For the layers made from the above crystal with different Tl concentrations, the three decay components are still found with the same relative amplitudes, which are independent of Tl concentration. In addition an ultrafast component wasobserved in these evaporated layers, with intensities
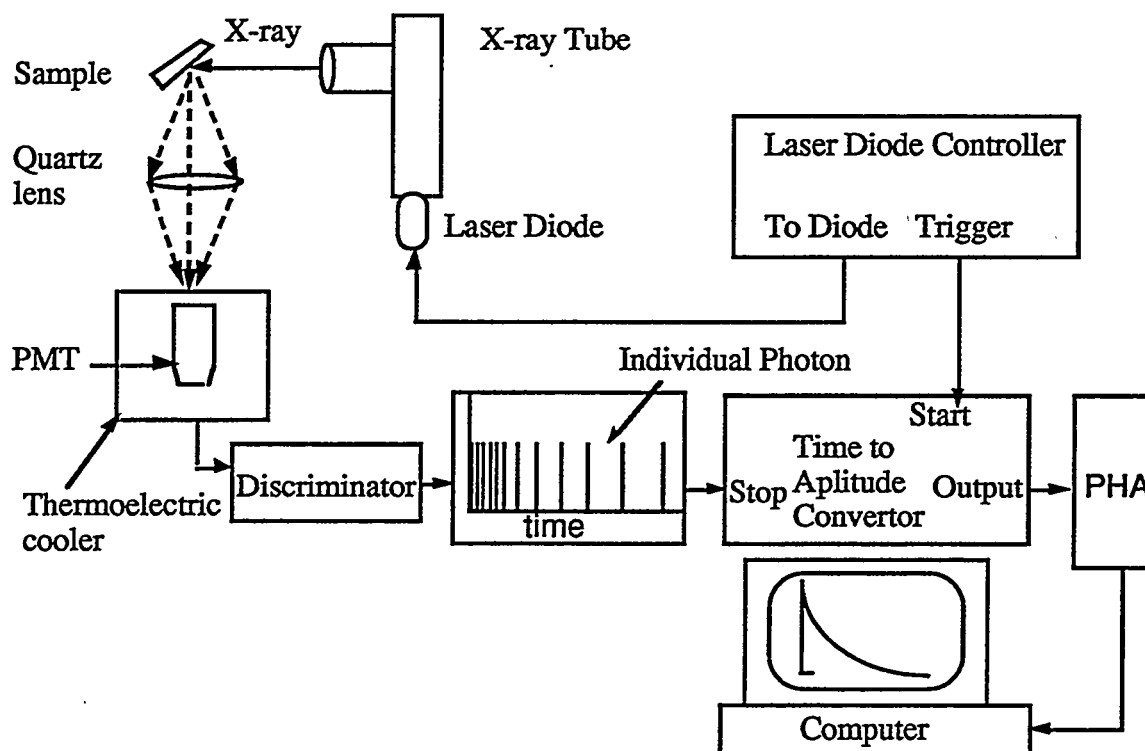
Fig.4.25 Schematic of the measurement setup for timing spectrum.

which are correlated with the Tl concentration. Fig.4.26(b) shown the light yield spectra of the evaporated layers at the Tl concentrations of 0.3 mole percentage and 0.6 mole percentage. The amplitude of the ultrafast component of the sample with less Tl is larger than that of higher Tl one and has two components roughly t1=2 ns, t2=6 ns. The reason for the appearance of this unique ultrafast component in the evaporated layer may be due to the redistribution of the Tl^+ luminescent center during the fabricating of the layer.

y1=619.45*e(-x/875)
y2=397*e(-x/1436)
y3=189*e(-x/3433)

(a)

CsI(0.3%Tl)
CsI(0.6%Tl)
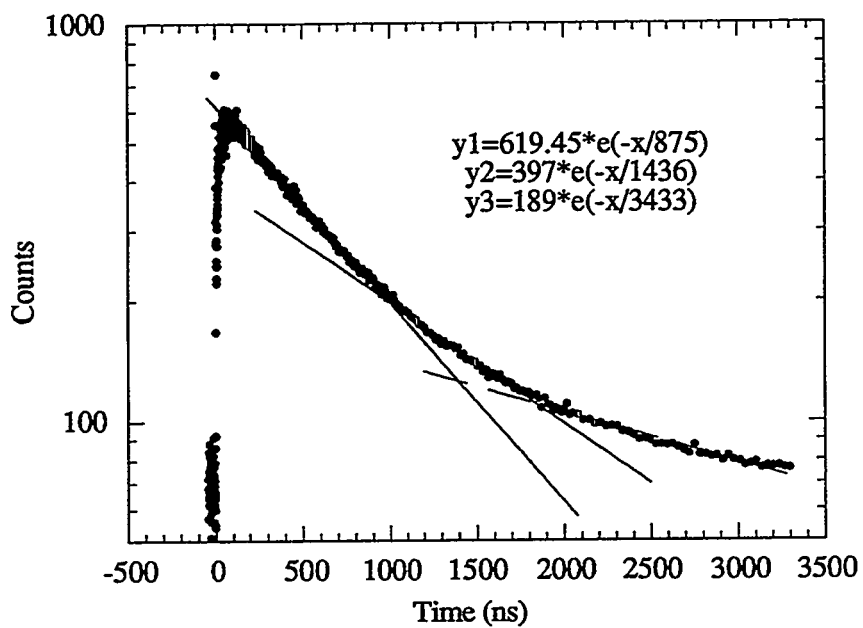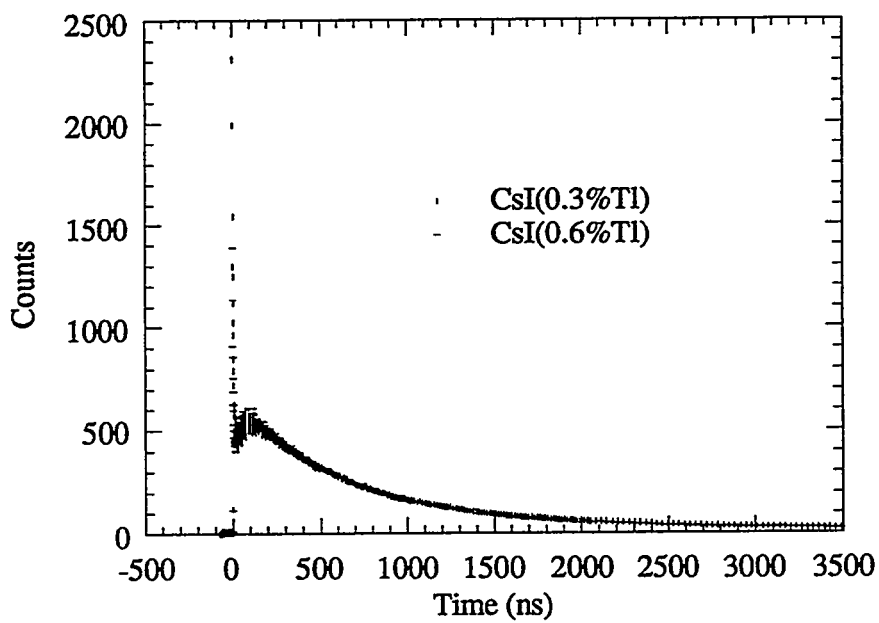
(b)

Fig.4.26 Decay time (a)CsI(Tl) crystal, (b)Evaporated CsI(Tl) layers
with Tl concentration of 0.3 mole% and 0.6 mole %.

REFERENCES:

[1] V. Perez-Mendez, G. Cho, J. Drewery, T. Jing, S. N. Kaplan, S. Qureshi, and D. Wildermuth," Amorphous Silicon Based Detector," J. Non-crystalline Solids, vol. 137, No.12, 1991, 1291-1296.

[2] I. Fujieda, G. Cho, J. Drewery, T. Gee, T. Jing, S. N. Kaplan, V. Perez-Mendez, D. Wildermuth and R. A. Street," X-ray and Charged Particle Detection with CsI(TI) later Coupled to a-Si:H Photodiode layers," LBL-29477, IEEE Trans. Nucl. Sci. vol. 38, No. 2, 1991, pp. 255-262.

[3] H. Ito, S. Matsubara, T. Takahashi, T. Shimada and H. Takeuchi," Integrated Radiation Detectors with a-Si Photodiodes on Ceramic Scintillatiors," Jpn. J. Appl. Phys. vol. 28,1989, pp. L1476-L1479.

[4] W. Hillen, W. Eckenbanch, P. Ouadfliey and T. Zaengel," Signal-To-Noise Performance in Cesium Iodiode X-ray Fluorescent Screens," Medical Imaging V, Proc. SPIE, vol. 1443, San Jose, California, Feb., 1991, pp. 120-131.

[5] R. Chechik, A. Breskin, A. Akkerman, A. Gibrekhterman, I. Frumkin, H. Aclander, and V. Elkind,"Towards fast Transition Radiation Imaging Detectors with CsI Convertors," IEEE Trans. Nucl. Sci. vol. 39, No. 4, 1992, pp. 728-737.

[6] C. M. Castelli, N. M. Allinson, K. J. Moon, and D. L. Watson,"High Spatial Resolution Scintillator screens coupled to CCD Detectors for X-ray Imaging Applications," Nucl. Instr. and Meth. vol. A348, N.2-3, 1994, pp. 649-653.

[7] C. W. Bates," Scintillation Processes in Thin Films of CsI(Na) and CsI(TI) due to low Energy X-rays, Electrons and Protons," Adv. Electron Phys. vol.20A,1968, pp. 451-459.

[8] A. L. N. Stevels and A. D. M. Schrama de Pauw," Vapor-Deposited CsI:Na layers, I. Morphologic and Crystallographic Properties," Philips Res. Repts., vol 29, 1974, pp. 340-352.

[9] H. Washida and T. Sonoda," High Resolution Phosphor Screen for X-ray Image Intensifier," Adv. Electron Phys. vol 52, 1979, pp. 201-207.

[10] J. B. Birks, *The Theory and Practice of Scintillation Counting*, Pergamom Press, 1964, pp. 72.

[11] R. B. murray, "Energy Transfer in Alkali Halide Scintillators by Electron-hole Diffusion and Capture," IEEE Trans. Nucl. Sci. Vol. 22, No.2, pp. 54-57 (1975).

[12] R. G. Kaufman, W. B. Hadley, and H. N. Hersh,"The Scintillation Mechanism in Thallium Doped Alkali Halides," IEEE Trans. Nucl. Sci. vol.17, No.3, pp. 82-88 (1970).

[13] T. Jing G. Cho, J. Drewery, I. Fujieda, S. N. Kaplan, A. Mireshghi, V. Perez-Mendez, and D. Wildermuth," Enhanced Columnar Structure in CsI Layer by

Substrate Patterning," IEEE Trans. Nucl. Sci. vol. 39, No. 5, 1992, pp. 1195-1198.

[14] L. I. Maissel and R. Glang, *Handbook of Thin Film Technology*, Mc Graw-Hill, Inc., New York, p.8-5 (1970).

[15] J. W. Gibbs, *Collected Works*, Vol.I, Yale University Press, New Haven, 1948.

[16] C. F. Powell, J. H. Oxley, and J. M. Blocher, Jr., *Vapor Deposition*, John Wiley & Sons, Inc., New York, p.129 (1966).

[17] M. Volmer, Kinetik der Phasenbildung, Steinkopff, Dresden und Leipzing, 1939.

[18] B. A. Movchan and A. V. Demochishin, Phys. Metals Metallogr. vol.28, p.83 (1969).

[19] J.A. Thornton, Ann. Rev. Matter. Sci., Vol.7, p.239(1977).

[20] J.A. Thornton," The Microstucture of Sputter-deposited Coatings," J. Vac. Sci. Technol., A4(6), p.3059 (1986).

[21] R. Messier, A. P. Giri, and R. A. Roy,"Revised Structure Zone Model for Thin Film Physical Structure," J. Vac. Sci. Technol., A2, p.500 (1984).

[22] A. M. Haghiri-Gosnet, F. R. Ladan, C. Mayeux, and H. Launois,"Stress and Microstructure in Tunsten Sputtered Thin Films," J. Vac. Sci. Technol., A7(4), p.2663 (1989).

[23] J.A. Thornton," Influence of Apparatus Geometry and Deposition Conditions on the Structure and Topography of Thick Sputtered Coatings," J. Vac. Sci. Technol., Vol. 11, No.4, p.666 (1974).

[24] K. Itoh, M. Kamiya, K. Hara, T. Hashimoto,"Argon Gas Pressure Dependence of the Columnar Grain Structure in Iron Films Deposited Obliquely by Sputtering," Thin Soild Films, Vol.195, N1-2, p.245-255 (1991).

[25] J.A. Thornton," Influence of Substrate Temperature and Deposition rate on Structure of Thick Sputtered Cu Coatings," J. Vac. Sci. Technol., Vol. 12, No.4, p.830 (1975).

[26] D. M. Mattax and G. J. Kominiak, "Structure Modification by Ion Bombardment During Deposition," J. Vac. Sci. Technol., Vol. 9, No. 1, p.528 (1972).

[27] J. L. Hughes, Metals eng. Q. Vol.14, p.1 (1974).

[28] T. Spalvins and M. Brainard, "Nodular Growth in Thick-sputtered Metallic Coatings," J. Vac. Sci. Technol., Vol. 11, p.1186 (1974).

[29] R. Mattheis, F. Thrum, and H. J. Anklanm, "Nodular Growth in Thin Films-Preparation and Transmission Electron Microscopy Characterization in Co-Cr Layers on Silicon Substrates," Thin Solid Films, Vol.188, N.2, p.335 (1990).

[30] H. J. Anklanm, L.Fritzsch, R. Mattheis, S. Muller-Pfeiffer, and F. Thrum, Wiss. Ber. Phys. Tech. Inst. No.4, 34 (1989).

116

[31]   R. J. Artley, K. Ouchi, and S. Iwasaki,"The Origins of Defects in Sputtered Co-Cr Perpendicular Magnetic Recording Media," IEEE Trans. Magnetics Vol.24, p.2335 (1988).

[32]   H. J. Leamy, G. H. Gilmer, and A. G. Dirks, Current Topics Mater. Sci. Vol.6, p.309 (1980).

[33]   D. J. Henderson, M. H. Brodsky, and P. Chaudhari,"Simulation of Structural Anisotropy and Void Formation in Amorphous Thin Film," Appl. Phys. Lett. Vol. 25, p641 (1974).

[34]   T. Motohiro,"Application of Monte Carlo Simulation in the Analysis of a Sputter-deposition Process," J. Vac. Sci. Technol., A4, No.2, p.189 (1986).

[35]   S. Muller-Pfeiffer, Thesis, Jena (1990).

[36]   G. Neumann and W. Hirschwald,"The mechanisms of Surface Self Diffusion," Z. Phys. Chem., N.F. B81, 163 (1972).

[37]   B. Lewis and J. C. Anderson, *Nucleation and Growth of Thin Films*, Academic Press, New York, p. 314-435 (1978).

[38]   J.A. Shepherd, S.E. Sobottka, and M.B. Williams," Performace and Fabrication of Thin Film NaI(Tl) Scintillators for Use on Imaging Photomultiplier Tubes," IEEE Trans. Nucl. Sci. vol. 40, No. 4, 1993, pp. 413-416.

[39]   T. Jing, C.A. Goodman, G. Cho, J. Drewery, W.S. Hong, H. Lee, Y. Kitsuno, S.N. Kaplan, A. Mireshghi, V. Perez-Mendez, and D. Wildermuth, "Amorphous Silicon Pixel Layers with Cesium Iodide Converters for Medical Radiography," Presented at IEEE NSS and MIC in San Francisco at Nov. 1993. IEEE Trans Nuc. Sci., NS-41 p. 903-909 (1994).

[40]   H. Grassmann, E. Lorenz and H. G. Moser," Properties of CsI(Tl) - Renaissance of an old scintillation material," Nucl. Instr. and Meth. vol. 228, 1985, pp. 323-326.

[41]   J. B. Birks, *The Theory and Practice of Scintillation Counting*, Pergamom Press, 1964, pp. 436.

[42]   P. Schotanus, R. Kamermans and P. Dorenbos," Scintillation Characteristics of Pure and Tl-doped CsI Crystal," IEEE Trans. Nucl. Sci. vol. 37, No. 2, 1990, pp. 177-182.

[43]   R. D. Giauque, F. S. Goulding, J. M. Jaklevic and R. H. Pehl," Trace Element Determination with Semiconductor X-ray Spectrometers," Analytical Chemistry, vol. 45, 1973, pp. 671-681.

[44]   C. Bieler, D. Burkart, J. Marks,M. Riebesell, H. Spitzer, K. Wittenburg and G.G. Winter," Radiation Damage of BGO and CsI(Tl) Crystals," Nucl. Instr. and Meth. vol. A234, 1985, pp. 435-442.

[45]   S. Schlogl, H. Spitzer, and K. Wittenburg," Radiation Damage of CsI(Tl) Crystals in a Long Term Exposure at Petra," Nucl. Instr. and Meth. vol. A242, pp. 89-94 (1985).

[46] M. Kobayashi and S. Sakuragi," Radiation Damage of CsI(Tl) Crystals above 10^3 rad," Nucl. Instr. and Meth. vol. A254, 1987, pp. 275-280.

[47] C.L. Woody, J.A. Kierstead, P.W. Levy, and S.Stoll," Radiation Damage in Undoped CsI and CsI(Tl)," IEEE Trans. Nucl. Sci. vol. 39, No. 4, 1992, pp. 524-531.

[48] C.L. Woody, P.W. Levy, J.A. Kierstead, T. Skwarnicki,Z. Sobolewski,M. Goldberg, N. Horwitz, P. Souder, and D.F. Anderson," Readout Techniques and Radiation Damage of Undoped CsI," IEEE Trans. Nucl. Sci. vol. 37, No. 2, 1990, pp. 492-499.

Chapter 5. Radiation Detection

5.1 MIPs Detection in Particle and Nuclear Physics

Particle and nuclear physics experiments require position information using pixel or strip configurations. Most of the time, minimum ionizing particles- MIPs are detected. Three configurations are possible (1) using a detector > 50 μm thick in which each MIP produces ~80 e,h pairs/μm[1-3]. (2) The second possibility is to use the scintillator/a-Si:H thin photodiode structure. (3) using the a-Si:H photoconductor instead of the photodiode in order to increase the sensitivity of the detector[4]. In later sections, we will demonstrate the capability for detecting minimum ionizing electrons based on the last two configurations.

5.1.1 Stopping power and electron range in the CsI

For electrons of up to 10MeV the dominant modes of energy loss are excitation and ionization of the electrons of the absorber. the rate of energy loss is:

$$-\frac{dE_\beta}{dx} = \frac{4\pi e^4 ZN}{mv} \cdot B, \qquad (5.1)$$

where e, m are the electronic charge and mass, v the particle velocity, Z the atomic number of the absorber and N the number of absorber atoms per cm^3. For $v \ll c$ (light speed) the stopping number, B, is[5]:

$$B = \ln(0.583 \ mv^2 I), \qquad (5.2)$$

Here I is the mean ionization potential of the absorber atom. At higher energies B increase in a manner given by Moller's formula[6]:

$$2B = \ln[mv\ ^2E_\beta/2I^2(1-\beta^2)] - \ln2(2\sqrt{(1-\beta^2)} - 1 + \beta^2) + 1 - \beta^2 \qquad (5.3)$$

where $\beta = v/c$. There is a minimum of the rate of energy loss based on the eq.(5.1, 5.2, 5.3). Particles with that energy are called minimum ionizing particles- MIPs.

The rate of energy loss of electrons in CsI is shown in Fig.5.1, while Fig.5.2 shows the range of electrons in CsI.
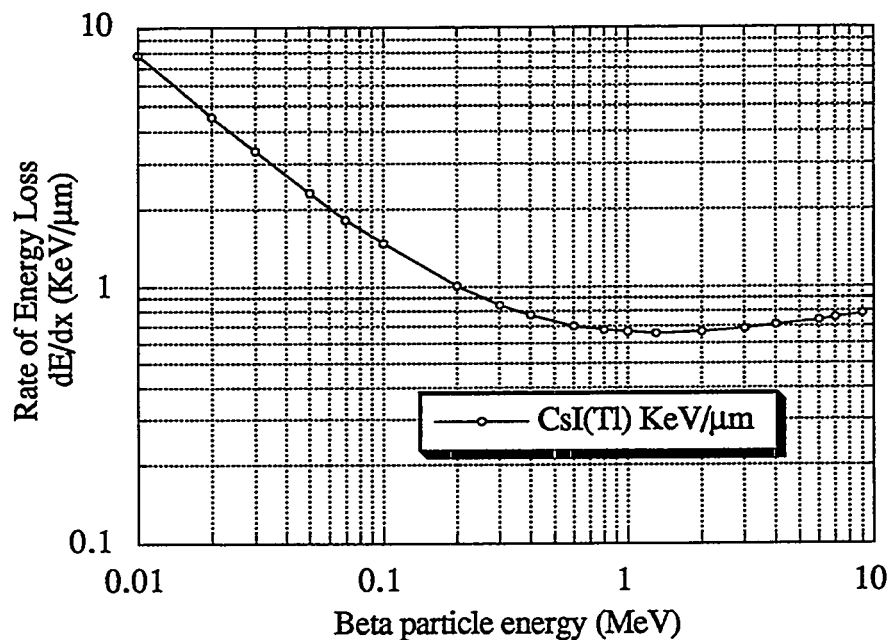

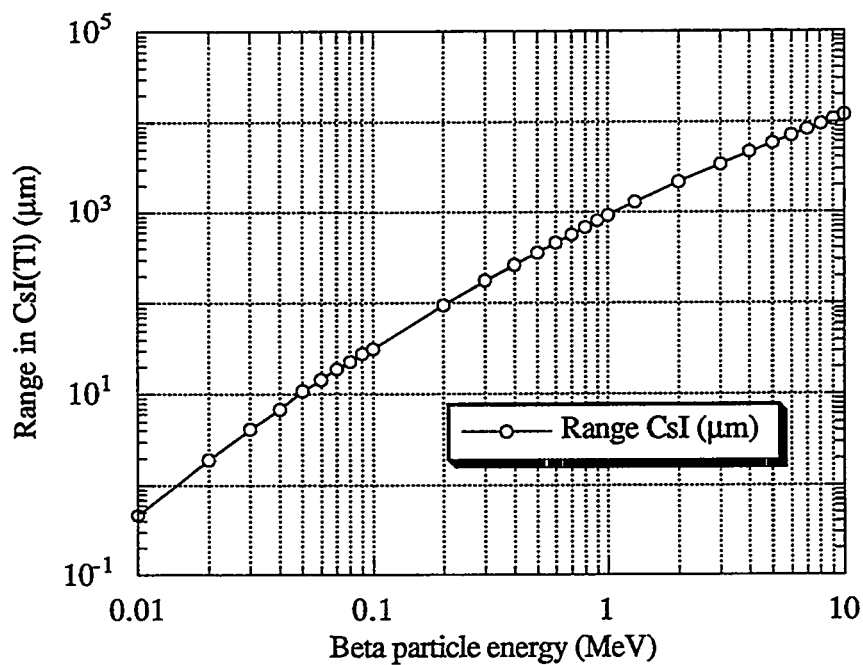Fig.5.1 Rate of energy loss,-dE/dx, for electrons in CsI as a function of energy.

Fig. 5.2 Range of beta particles in CsI as a function of energy.

5.1.2 Detection of β particles from Bi²⁰⁷

The scintillator of choice is CsI(Tl) with the columnar structure discussed in chapter 4. A a-Si:H diode with ITO top contact and light detection efficiency ~70% was coupled to the CsI layers with thickness 315mm, 461 μm and 894 μm. The output of the photodiode was amplified by a charge-sensitive preamplifier and then shaped by a quasi-Gaussian shaping amplifier. Fig.5.3 shows the measured pulse height spectra in CsI/photodiode combination for incident electrons from Bi²⁰⁷.
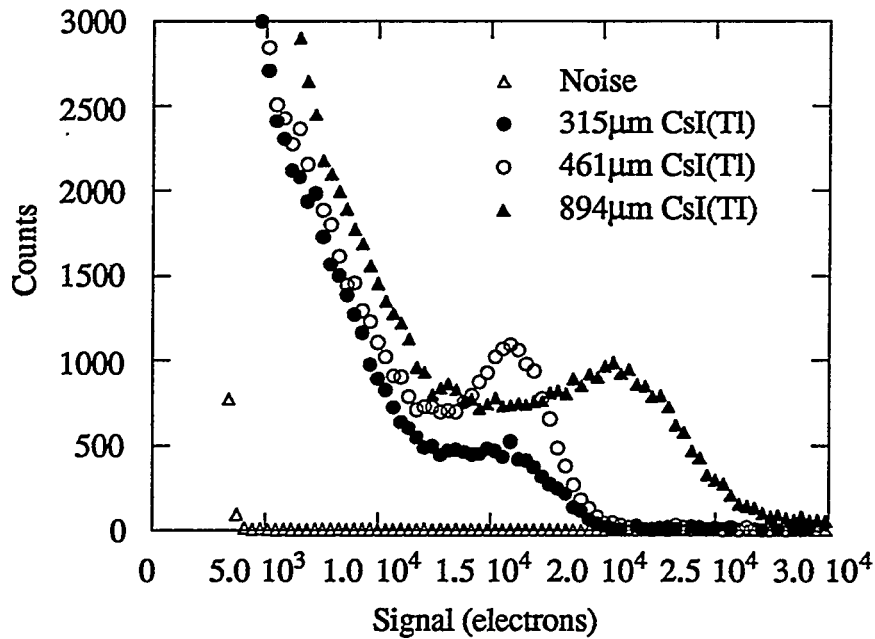

Fig.5.3 Detection of b particles from a Bi207 source by CsI(Tl) layers coupled to a photodiode.

The high count rate at low energy is due (aside from noise) to the fact that electrons often undergo large-angle deflections along their track which leads to the phenomenon of backscattering[7]. An electron entering one surface of an absorber(scintillator) may undergo sufficient deflection so that it reemerges from the surface through which it entered.

121

These backscatterred electrons do not deposit all their energy in the CsI later and therefore can have a significant effect on the response of detectors to measure the energy of externally incident electrons. Backscattering is most pronounced for electrons with low energy and absorber with high atomic number such as CsI in this case. To reduce this backscattering effect and suppress the noise, a coincidence method was used to measure the β particles as described in next section.

5.1.3 Detection of ß particles from a Sr^{90} source

We measured signals produced by minimum-ionizing electrons from a Sr^{-90} source with the CsI/a-Si:H pin diode detector. A 10 μm thick a-Si:H pin was used to decrease the detector capacity in order to reduce the noise level of the output. A 950μm thick evaporated CsI(Tl) layer was coupled to a-Si:H photodiode. A thin aluminum foil was placed on the top of the scintillator as reflector to increase light collection. The measurement setup is shown in Fig.5.4(a). A Hamamatsu photodiode S3590-01 was placed below the CsI/a-Si;H pin detector as a trigger counter to count only the high energy > 1.5 MeV tail of the beta spectrum. The count is recorded by passing the pulse from the CsI(Tl)/a-Si:H photodiode through an electronic gate that is open if a coincident pulse is detected by the Hamamatsu photodiode. In this way backscattering electrons and some of the device noise were rejected. The ß particles were collimated by a 8mm thick aluminum collimator with 1.5 mm diameter hole. The output of the photodiode was amplified by a charge-sensitive amplifier and then connected through a shaping amplifier to a PHA. The shaping time was set at 1 μs.

A typical pulse-height distribution for the measurement is shown in Fig.5.4(b). The peak of the spectra corresponds to approximately 22,000 electron-hole pairs. This is equivalent to a generated light yield of 40,000 visible scintillation photons. This signal size

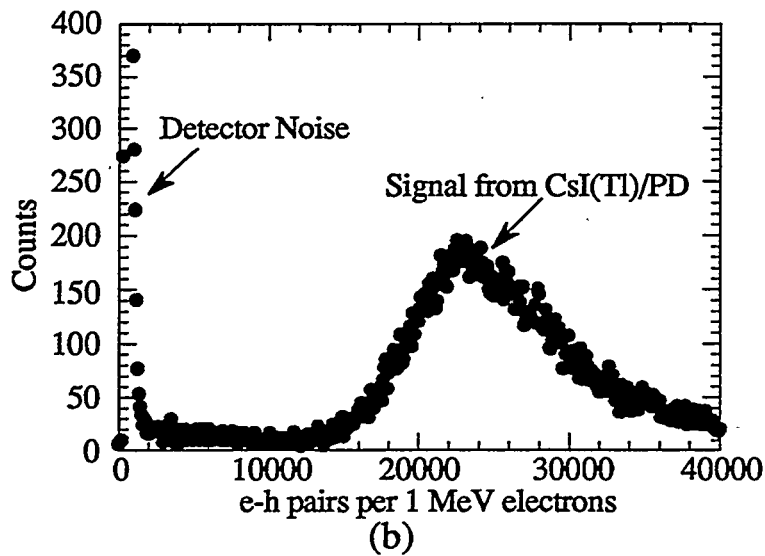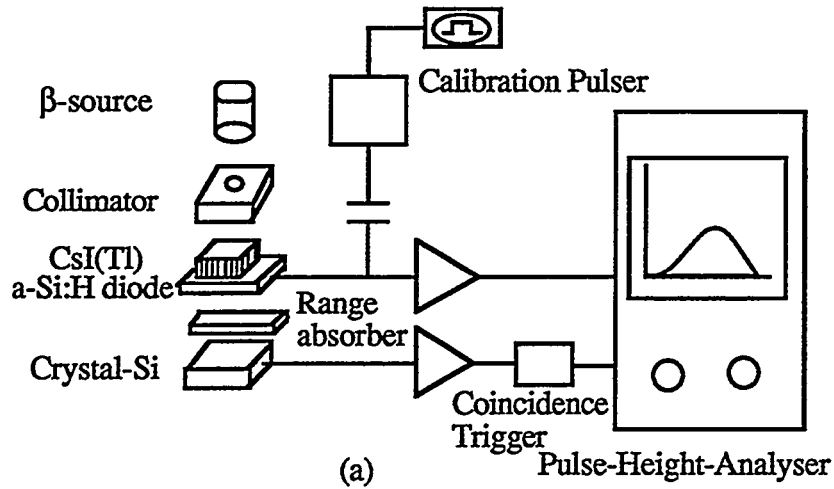can be increased by a factor ~ 3-6 using the photoconductive gain mechanism discussed in the next section.

Fig.5.4 MIPs measurement (a) experimental setup;(b) pulse height distribution
1 MeV betas.

5.1.4 Detection of ß particles by CsI(Tl)/photoconductor combination

As discussion in section 3.5, a p-i-n diode operated under forward bias exhibits a faster photocurrent decay than the n-i-n one, moreover it has the same optical gain as n-i-n one for a short integrating time. Thus we use a p-i-n diode as a photoconductor coupled to CsI(Tl) to detect the Beta particles. The measurement setup and procedure are the same as described above. Fig.5.5 shows the pulse height distribution measured in a a-Si:H photoconductor coupled to a CsI layer. The amplifier shaping time was set at 1 µs for suppressing noise level. Even so the noise level is high for a diode with large current and
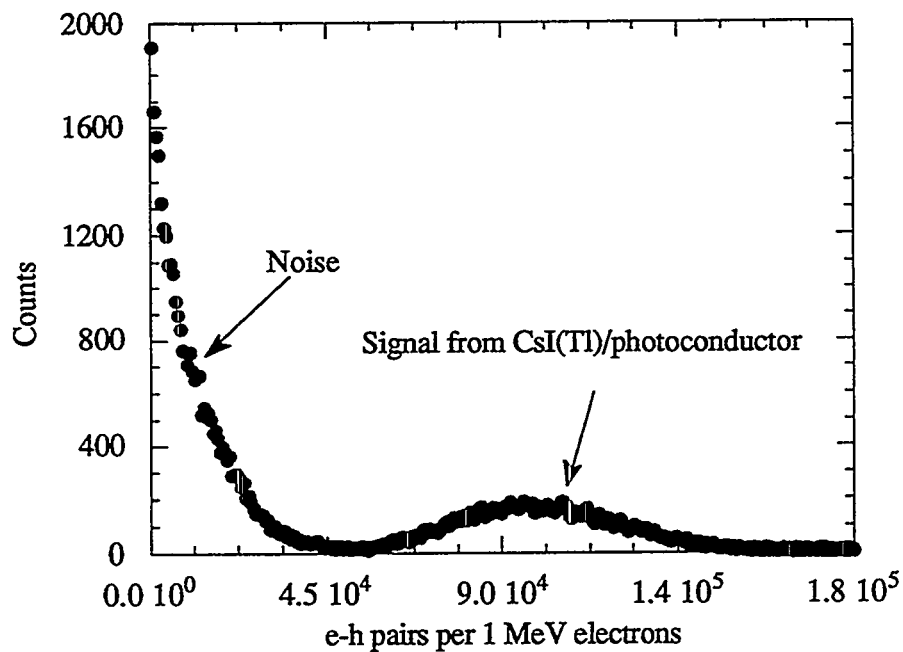

Fig.5.5 The detection of b particles from Sr^{90} by a CsI layer coupled to photoconductor with shaping time 2 µs.

124

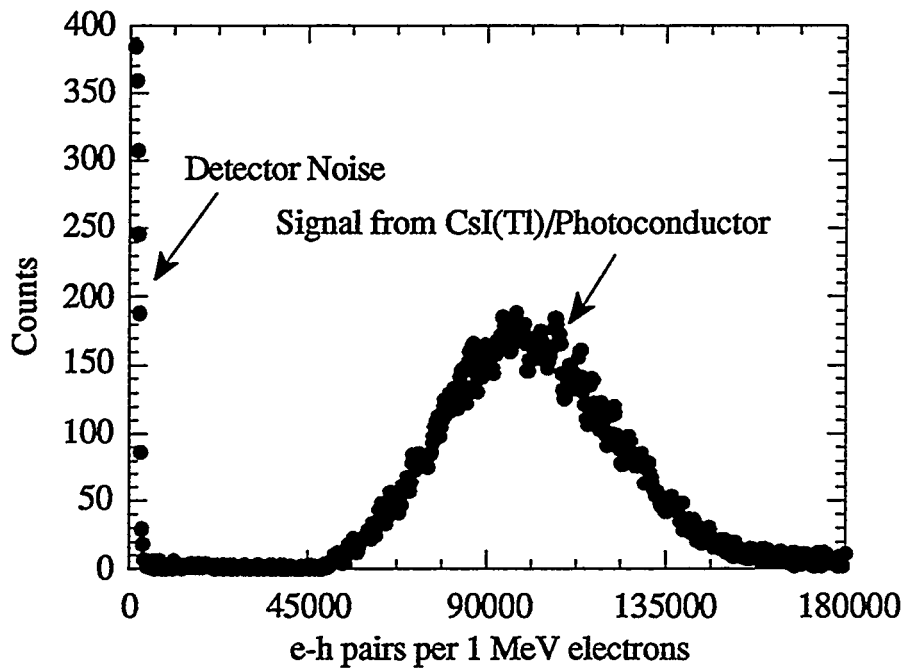Fig. 5.6 The expected Beta spectrum from a photoconductor coupled to
a 950 µm CsI(Tl) layer calculated for pixel size 100x100 µm.

large capacity, when the active area of the diode is ~8 mm^2. But if we use a detector pixel

size of 100x100 μm^2 in the detector array, the current will be substantial lower in each

pixel, therefore the noise level will be quite low ~ 2300 electrons for the same measuring

arrangement. The calculated pulse spectrum from Fig.5.5 is shown in Fig.5.6. The noise

will be well separated from the signal produced by the incident electrons.

5.2 X-ray Detection

At present the detectors used in medical imaging are (a) X-ray film coupled to

intensifying screens Lanex or Chronex, manufactured by Kodak and DuPont

respectively[8]. (b) Real time imaging is accomplished by electronic image intensifier tubes

with a X-ray sensitive layer of CsI(Na) deposited internally on the cathode. These both

have a spatial resolution-given as an MTF (Modulation Transfer Function) which has a

value of 5-6 line pairs per mm at the 10% level. A solid state replacement is a pixel array of

a-Si:H photodiodes with either a Lanex or CsI(Tl) scintillator. X-ray converter prototype arrays with a pitch of 125x125μm have been made by Xerox PARC[9]. The MTF of those devices is ~5 line pairs per mm at 10% level. We have measured the MTF of our CsI(Tl) columnar layers with X-rays of 41 and 90 KVp. The MTF of our CsI(Tl) layers as a function of thickness is shown in Fig.5.14. These layers have X-ray detection sensitivities ~3 times higher than those of Lanex screen when measured at the same resolution. We are presently testing pixel diode arrays with pixel size 50x50 μm coupled to CsI(Tl) layers 150μm thick to give an overall MTF of >10 lp/mm.

5.2.1 Absorption of X-ray in CsI layer

Gamma rays and X-rays interact with matter mainly by one of three types of process, namely the photoelectric effect, Compton scattering and pair production. In the medical imaging range of X-ray energies, the interaction coefficient in CsI is mostly due to the photoelectric effect. Thus the absorption coefficient can be substituted by the photoelectric coefficient for the X-ray energies below 200 KeV as shown in Fig.5.7.
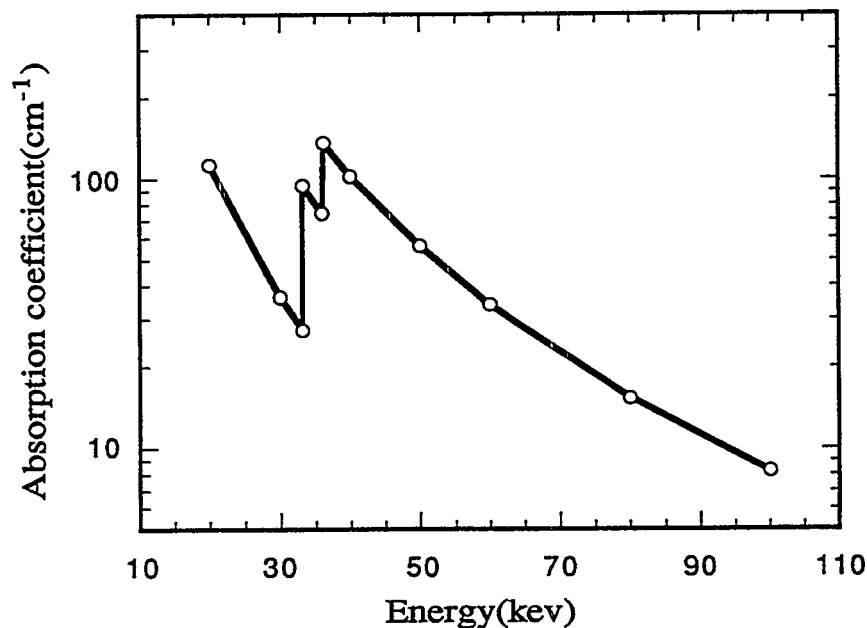

Fig.5.7 Absorption coefficient of CsI as a function of photon energy.
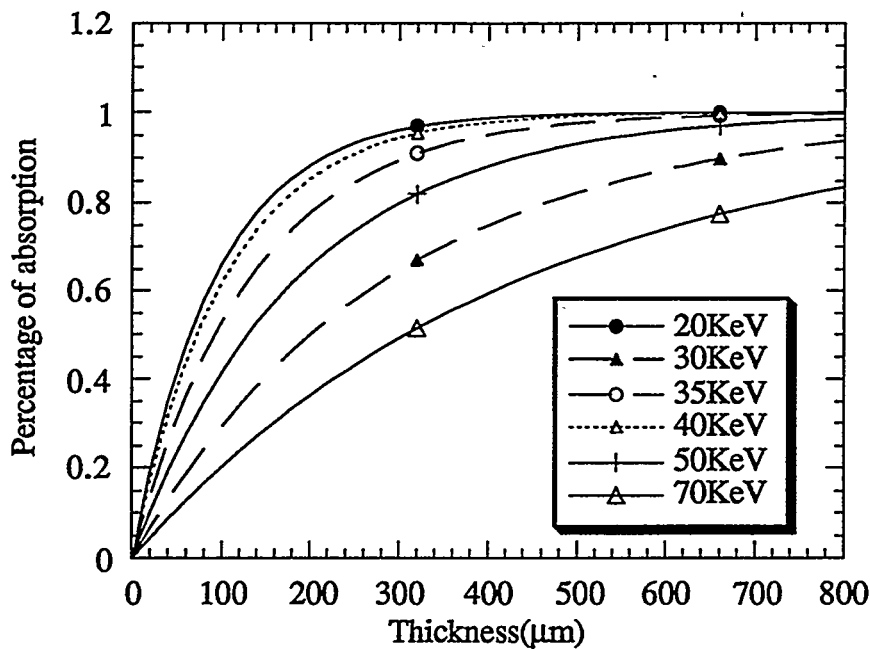
126

Fig.5.8 Calculated percentage of the absorption in different thickness CsI layers.

Scintillators for radiation detection are usually required to have high resolution and high output brightness characteristics. The brightness of the light output is, in part, a function of the thickness of the scintillator layer, which determines the amount of X-ray energy absorbed. Fig.5.8 shows the quantum efficiency of CsI(Tl) layers for different X-ray energies as a function thickness. One should note that just below and above the K-edge the absorption efficiencies are very different as shown in the figure.

5.2.2 Spatial resolution

The CsI screen spatial resolution was evaluated by measuring its line spread function (LSF). The scintillation light spread from evaporated CsI(Tl) layers (various thicknesses) was characterized by exposing a scintillator to a narrow beam of X-rays and detecting the light output with a linear position sensitive detector array. The shematic of the

measurement setup is shown in Fig.4.9. The low energy x-ray beam was generated by an x-ray tube operated at 49KVp and viewed through a 25 μm wide slit. The penetration depth is small enough so that the most of the irradiation energy could be deposited inside the CsI(Tl) film. A linear silicon photodiode array (EG&G Reticon RL0256SBU-001) with 20 dots/mm resolution was used as the light sensor. The output signals were digitized and stored in a computer for further analysis. The measured line spread function is the convolution of the three components: finite width of the X-ray beam, the spatial resolution of the sensor array and light spread of the scintillator, as shown in Fig.4.10. Thus the real line spread function of the CsI layers should be deconvoluted from the total line spread function response in the following steps:

(a) MTF of X-ray beam

First the X-ray beam through a narrow collimation slit with a finite size can be approximately expressed as a Gaussian distribution; thus X-ray beam intensity (LSF) can be written as:

$$X(u) = A \exp(-u^2/\sigma^2), \tag{5.4}$$

where u is the position, A is the amplitude at position u=0. σ is the standard deviation, and can be obtained by relation:

$$FWHM = 2.35\sigma, \tag{5.5}$$

FWHM is about 30μm (the width of the collimating slit) in our setup. Thus the normalized MTF of the X-ray beam is:

$$MTF_{x-ray} = \int_{-\infty}^{\infty} X(u)\exp(-2\pi iku)/A = \exp(-\sigma^2\pi^2k^2), \tag{5.6}$$

Here k is spatial frequency.

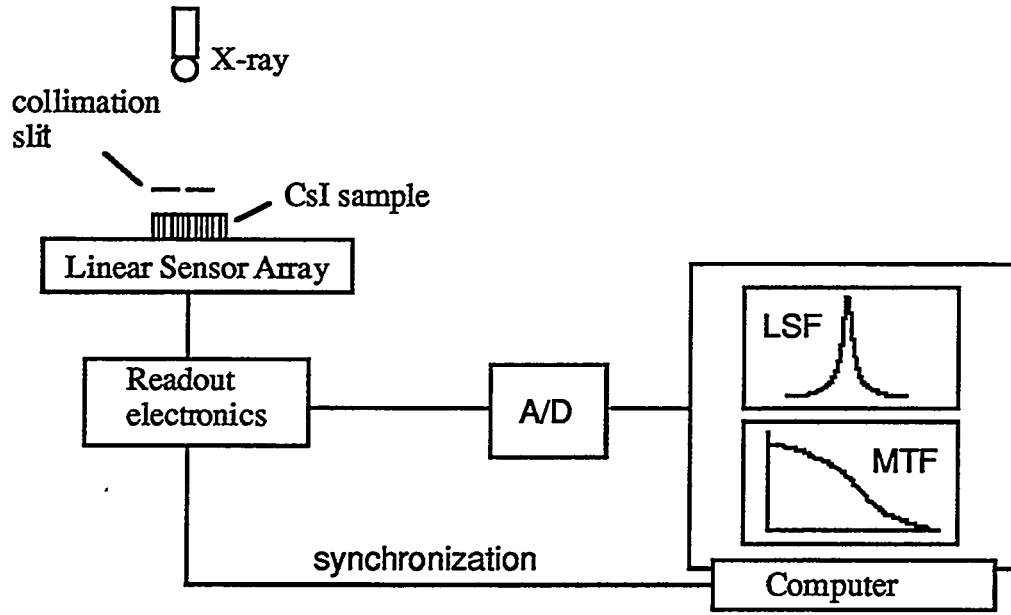Fig.5.9 Schematic of LSF and MTF measurement setup.

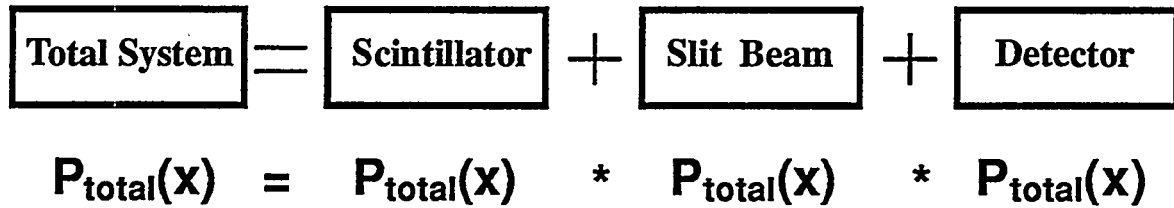$$P_{total}(x) = P_{total}(x) * P_{total}(x) * P_{total}(x)$$

Fig.5.10 The diagram of MTF components.

(b) MTF of the sensor array

The MTF is calculated for one-dimensional static case. The input illumination pattern for evaluation of the MTF is commonly given by[10]

$$X(\theta) = 0.5(1+\cos(\theta),$$ (5.7)

where is a general spatial parameter. Then the MTF is defined by the response of the sensor array to the input:

$$MTF = (Y_{max} - Y_{min})/(Y_{max} + Y_{min}),$$ (5.8)

129

Where Y_{max} and Y_{max} are the values of a neighboring maximum and minimum, respectively, of the output. Let T is the period of the input, L is the sensor pixel. For simplicity, let L is equal to the pixel pitch. We normalize the pixel spacing as

$$\theta_1 = \pi L/T, \qquad (5.9)$$

When the input maximum is aligned at the center of the sensor, Y_{max} and Y_{max} are easily obtained as:

$$Y_{max} = \int_{-\theta_1}^{\theta_1} 0.5(1+\cos\theta)d\theta = \theta_1 + \sin\theta_1, \qquad (5.10)$$

$$Y_{min} = \theta_1 - \sin\theta_1, \qquad (5.11)$$

Thus MTF of the sensor is

$$MTF = \sin\theta_1/\theta_1 = \sin(\pi L/T)/(\pi L/T), \qquad (5.12)$$

This is the MTF of the sensor for ideal condition, such as no across-talk coupling signal between the neighboring pixels. Fig.5.11 gives the MTFs of sensor elements for different spacings. For revealing the pixel effect, MTFs for different pixel sizes are also plotted in the same graph.
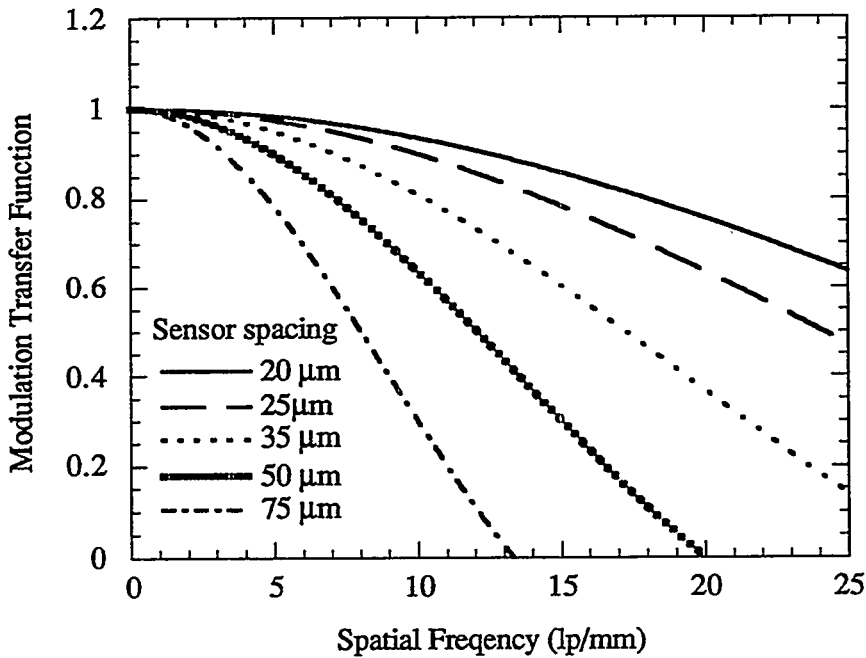

Fig.5.11 The calculated MTFs for different pixel spacing.

130

Now the line spread function of the scintillator is obtained as:

$$MTF_{CsI} = MTF_{CsI} / (MTF_{x-ray} MTF_{sensor}), \tag{5.13}$$

The line spread function for each scintillator was obtained by this method.

Table 5.1 Comparison of Characteristics of CsI(Tl) Layers with Lanex Screens

Scintillators	Relative Light Output	Spatial Resolution FWHM(μm)	MTF at 10 % Level (lp/mm)	Thickness (μm)
Lanex Fine Screen	100	96	9.1	75
Structured CsI(Tl) Layer	120	69	15.9	65
Structured CsI(Tl) Layer	170	81	12.0	75
Structured CsI(Tl) Layer	226	98	9.0	112
Lanex Medium Screen	210	179	4.6	140
Non-structured CsI	396	198	3.2	190
Structured CsI(Tl) Layer	340	110	8.0	144
Lanex Fast Screen	520	330	2.5	288
Non-structured CsI	410	259	2.9	220
Structured CsI(Tl) Layer	620	173	5.3	220

Fig.5.12 gives the LSF of Kodak Lanex Screens and CsI layers. Curve (a) shows the LSF of Lanex Fast Screen 288 μm thick, curve (b) that of non-structured CsI(Tl) crystal layer 220μm which exhibits a longer tail than curve (a) due to its good light transmission and curve (c) that of structured CsI(Tl) layer 220μm thick with the same light emission efficiency as the Lanex fast screen. The structured CsI(Tl) layer substantially suppressed its light spread by its auto-collimating structure. Thus it exhibits a narrower LSF that is superior to the Lanex fast screen and the non-structured CsI layer. Curves (d) and (e) are the same thickness 75 μm scintillators, Lanex fine screen and structured CsI(Tl) layer. Structured CsI layers deposited on flat substrate with inert gas enhancement give

131

almost same spatial resolution as layers deposited on patterned substrates. Again, the structured CsI(Tl) layer has a higher resolution than the Lanex screen. The comparison of characteristics of CsI(Tl) layers with Lanex screens are summarized in Table 5.1.
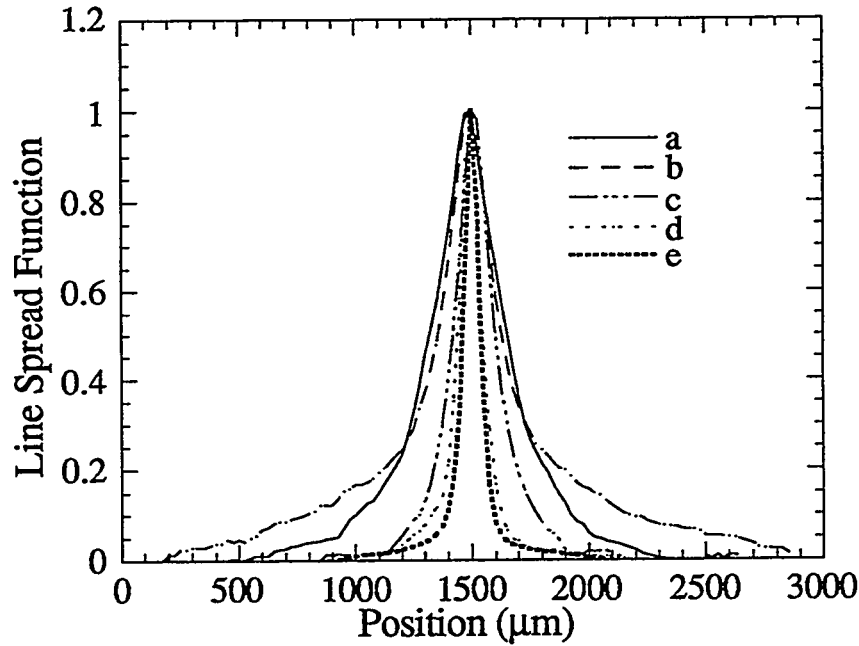

Fig.5.12 LSF of Lanex and CsI: (a) Lanex Fast Screen, (b) Non-structured CsI(Tl) crystal 220μm thick, (c) Structured CsI(Tl) layer 220μm thick, (d) Lanex fine Screen and (e) Structured CsI(Tl) layer 75μm thick.

The spatial resolution of an imaging system can be expressed as a frequency in the spatial domain, and is described in term of the modulation transfer function (MTF).

The MTF was determined by Fourier analysis of the line spread function. Mathematically, the MTF is expressed as

$$MTF = \left| \frac{\int_{-\infty}^{x} L(x) \exp[-2 \pi j f x] \, dx}{\int_{-\infty}^{x} L(x) \, dx} \right| \qquad (5.14)$$
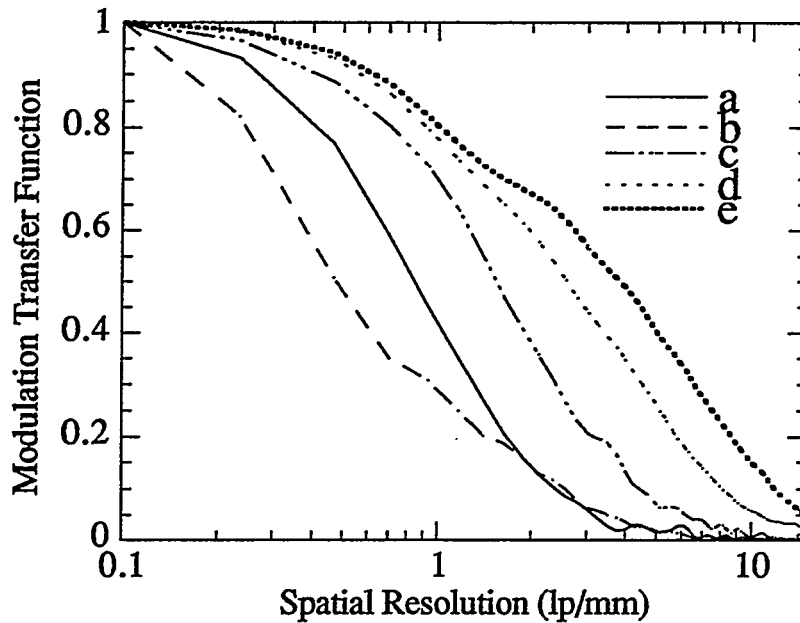
132

Fig.5.13 MTF calculated from LSF in Fig.5.12

The MTF of the CsI layers was obtained from MTF$_{tot}$ by correcting the MTF losses due to the limited width of the x-ray beam and the finite pixel size. The MTFs of the scintillation screens were normalized to unity at zero spatial frequency. The data of Fig.5.13 show the MTFs corresponding to the LSFs in Fig.5.12. Curves (a) and (b) exhibit the same MTF at the high frequency portion. The effect of reducing amplitude at the low frequency portion of MTF of non-structured CsI(Tl) is mainly due to its wider light spread tail. The structured CsI(Tl) curve (c) showed substantial improvement of MTF over curves (a) and (b) at all spatial frequencies. Curve (e) (structured CsI layer) has a spatial resolution at the 10% level of up to 12 lp/mm, while the Lanex fine screen has a spatial resolution 9.1 lp/mm at the same level. Further this CsI(Tl) layer has better light yield efficiency, see Table 5.1.

133
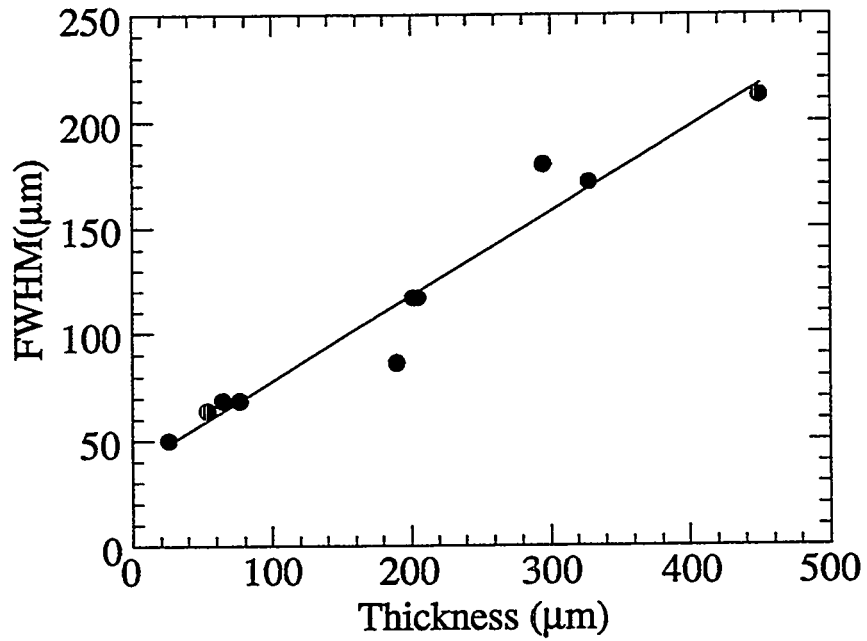
(a)
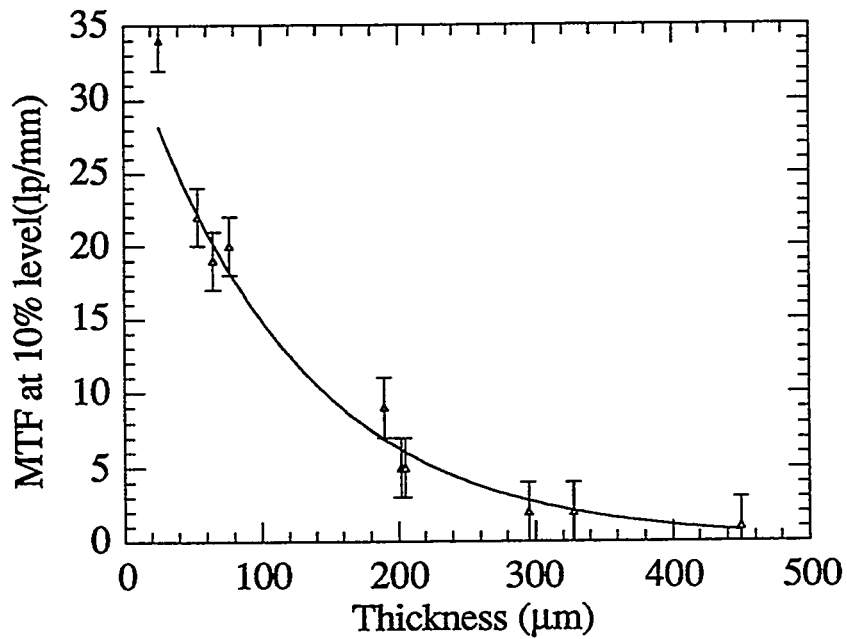
(b)

Fig.5.14 (a) the FWHM of various thickness CsI(Tl) layers; (b) the corresponding MTF.

With increasing thickness of the scintillator, the X-ray absorption increases, the light output also increases, but the resolution decreases. Fig.14(a) and (b) show the spatial resolution dependency of CsI(Tl) layers on their thicknesses.

5.2.3 Tooth X-ray imaging

As shown above, the columnar CsI(Tl) layer exhibits a high spatial resolution due to its collimating nature. When such a scintillator is coupled to a pixel detector array, a high quality radiation imaging can be obtained. As a demonstration, we placed a 120 μm thick columnar CsI on the top of a position-sensitive photosensor array and took an image of a real tooth as shown in Fig.5.15. The array area is 3x5 cm^2 with pixel spacing 50 μm (EG&E, Reticon). As a comparison, we took a picture with the same X-ray source using a conventional emulsion X-ray film as shown in Fig.5.16. As shown in these two pictures, the imaging quality using the solid state detector is almost the same as one by using the conventional method. In addition to the digilization of the imaging, another big advantage is that the electronic readout device can reduce, by as much as 90 percent, the amount of X-ray exposure compared to the conventional oral X-ray method using dental X-ray film without intensifying screens.

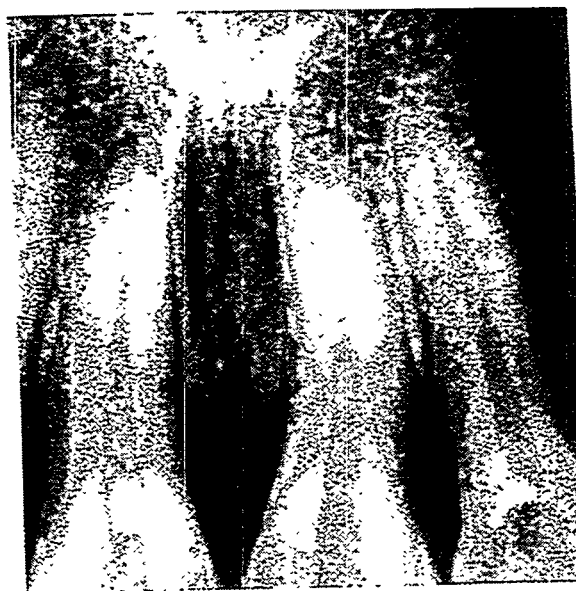Fig.5.15 The tooth radiograph obtained with the CsI(Tl)/photosensor array imager.

Fig.5.16 The The imaging of the same teeth as above obtained with
with conventional X-ray film.

136

References:

[1]   S. N. Kaplan, J. Morel, V. Perez-Mendez and R. A. Street, "Detection of Charged Particles in Amorphous Silicon Layers," IEEE Trans. Nuc. Sci., NS-33, p.351-354 (1987)

[2]   V. Perez-Mendez, S. N. Kaplan, G. Cho, I. Fujieda, S. Qureshi, W. Ward and R. A. Street, "Hydrogenated Amorphous Silicon Pixel Detectors for Minimum Ionizing Particles," Nuc. Inst. and Meth., A273, p.127-134 (1988)

[3]   W. S. Hong, J. S. Drewery, T. Jing, H. K. Lee, S. N. Kaplan, A. Mireshghi, and V. Perez-Mendez,"Thick (~50μm) Amorphous Silicon P-I-N Diodes for Direct Detection of Minimum Ionizing Particles," to be published in Nuc. Inst. and Meth., A, (1995).

[4]   T. Jing, C.A. Goodman, G. Cho, J.S. Drewery, W.S. Hong, H. Lee, S.N. Kaplan, A. Mireshghi, V. Perez-Mendez and D. Wildermuth, "Detection of charged particles and X-rays by scintillator layers coupled to amorphous silicon photodiode arrays," to be published.

[5]   H. A. Bethe, Handuch der Physik, Vol. 24, 273, Julius Springer (Berlin, 1933).

[6]   C. Moller, Ann. Physik, 14, 531 (1932).

[7]   G. F. Knoll, Radiation Detection and Measurement, John Wiley & Sons,Inc.,New York, p. 47 (1989).

[8]   V. Perez-Mendez, J. S. Drewery, W. S. Hong, T. Jing, H. K. Lee, S. N. Kaplan, and A. Mireshghi, "Amorphous Silicon Pixel Radiation Detectors and Associated Thin Film Transistor Electronics Readout," the Electrochemical Society Thin Film Technology Symposium, Miami, Oct. 10-14, 1994.

[9]   R. A. Street, J. Wu, R. Weisfield, S. E. Nelson, and P. Nylen, "Two Dimensional Amorphous Silicon Image Sensor Arrays," MRS, San Francisco, April. 17-21, 1995.

[10]   J. W. Coltman, "The Specification of Imaging Properties by Response to a Sine Wave Input," J. Opt. Soc. Am. 44, p.468 (1954).

137

Chapter 6. Conclusion

Hydrogenated amorphous silicon has been used in many kinds of detectors, ranging from light to charged particles and X-rays. Due to its random structure, a-Si:H is relative insensitive to radiation damage which makes it a good choice as a radiation detector. The thin film technology of a-Si:H with its inherent multilayer structure allows solutions not possible with crystalline silicon technology, especially a large-area capability.

For individual charged-particle position-sensitive detection, thin p-i-n layers are used as visible light detectors with a scintillator layer to provide the input signal by the energy deposition of the charged particle in it. The light collection loss for the scintillation light is mainly due to the p layer absorption. Thus a good light sensor diode was designed by optimizing the p-doped layer. The leakage current of the diode was analyzed. When designing a small pixel detector, the surface leakage should be eliminated. The charge from each pixel diode can be read out through TFT switches or can be connected to individual TFT preamplifiers for better signal to noise ratio.

A-Si:H n-i-n and p-i-n diodes can be operated as photoconductors with an increase of light sensitivity. For short times pulses with shaping time less than 5 μs, p-i-n and n-i-n structures give the same optical gain. However, for long term integration ~ milliseconds, the n-i-n device has a factor of 3 higher optical gain than the p-i-n structure, due to longer secondary current decay from n-i-n device. A-Si:H photoconductors are also good alternatives to light sensors as well as radiation detectors when coupled to suitable scintillators. A-Si:H diodes with photoconductive gain exhibit an alomst linear response to incident light photon flux up to 10^{15}photon/cm^{2}sec ($I_{ph} \propto \phi^{0.9}$) and should be suitable for medical imaging. The emergence of new applications provides the opportunity to improve the knowledge of photoconductivity in high resistivity semiconductors. Due to the simplicity of the configuration, a-Si:H photoconductors are particularly attractive from a

production yield standpoint, if we consider the large number of sensor elements associated with such 2-D imaging.

Techniques for forming columnar structure CsI were developed. The mechanism of the column formation on the patterned substrate was demonstrated. The various parameters affecting the growth of the material were discussed. When grown under inert gas pressure, the vapor kinetic energy is reduced by multiple collisions, thus reducing atom diffusion and resulting in enhanced column formation. The performances of the evaporated CsI layers was investigated, showing light yield comparable to crystal CsI. Maintaining the concentration of the activator Tl at a range of 0.02 -0.2 mole is required for an optimal light yield. Further annealing of the CsI was shown to increase its light output by 10 -40 percent. Measurement of radiation resistance of the CsI(Tl) layer has shown that CsI(Tl) layers have long term stability under X-ray radiation, which is essential for medical imaging.

The performance of a-Si:H p-i-n photodiodes coupled to CsI(Tl) scintillator for charged particle and X-ray detection was measured. The ability to detect minimum ionizing particles with S/N > 20 was demonstrated by using electrons with energies Ee>1.5 MeV from Sr[90] sources. Owing to the structure of the CsI(Tl) layers, it is possible to use a thicker scintillator layer for achieving higher x-ray absorption without the attendant degradation of resolution. A structured CsI(Tl) layer ~110μm thick produces twice as much light as a Kodak Lanex Fine intensifying screen with the equivalent resolution. Hence x-ray imaging can be carried out with smaller radiation doses. The performance of an x-ray imaging system is predominately determined by the input screen converters for the whole range of spatial frequencies which are of practical interest. The evaporated CsI(Tl) layer is more resistant to radiation damage than a CsI crystal. The predominant fluorescent decay time is less than 1 μs for the doped CsI layer. The measurements and analysis have shown that structured CsI(Tl) layers coupled to a-Si:H pixel arrays or other sensor arrays are good candidates for detectors in 2-dimensional imaging detection.

139